Università di Genova

PhD Program in Science and Technology for Electronic and Telecommunication Engineering

Simulations and experiments of electromagnetic problems involving materials in motion

Kirill Zeyde

Thesis submitted for the degree of *Doctor of Philosophy* (38° cycle)

February 2026

Prof. Mirco Raffetto — Tutor
Prof. Maurizio Valle — Head of the PhD program

Università di Genova
DITEN DIPARTIMENTO
DI INGEGNERIA NAVALE, ELETTRICA,
ELETTRONICA E DELLE TELECOMUNICAZIONI

Simulations and experiments of electromagnetic problems involving materials in motion

Kirill Zeyde

⋈

Reviewers

Giacomo Oliveri, Associate Professor, University of Trento, Italy
Daniele Trinchero, Assistant Professor, Polytechnic University of Turin, Italy

Tutor

Mirco Raffetto, Full Professor, University of Genoa, Italy

University of Genoa

Kirill Zeyde

Simulations and experiments of electromagnetic problems involving materials in motion

xvii+101 p.

For my inspiring daughters.

Abstract

The object of investigation in this work is electromagnetic waves in the presence of moving media. The study focuses on the effects induced directly by the motion of the media on incident radio-frequency time-harmonic electromagnetic fields. To restrict the consideration to frequency domain effects, a number of constraints were introduced in the formulation. We consider the motion of the media under the conditions that its boundaries remain stationary, the linear velocity vector field does not vary over time, and no transient processes occur in the system domain. The main attention is given to slow material motion, corresponding to the deeply non-relativistic state. The magnitude of these effects is extremely small, making them weak in comparison with the secondary scattering and refraction fields. For this reason, computing such effects with traditional techniques is challenging. To address this issue, a novel methodology is proposed. It relies on the Born approximation applied to electromagnetic problems involving moving media. The formulation employs equivalent field sources and is specifically designed to analyse the effects of motion on the electromagnetic field.

One of the key aspects discussed in this work is the implementation of the new methodology in the commercial CAD environment, namely COMSOL Multiphysics. This opens up broad opportunities for the practical application of the methodology, particularly for modeling and designing new devices and sensors for detecting moving effects, such as electromagnetic flowmeters. To add more specificity, the methodology was adapted for operation within the COMSOL Time Explicit EMW module.

The methodology was verified for a two-dimensional problem of electromagnetic wave scattering by an infinite circular cylinder moving along its axis of symmetry. The results obtained using the methodology were compared with the semi-analytical solution as well as with traditional numerical difference methods. The methodology was partially verified for a three-dimensional problem in which the scatterer was a finite-length cylinder, with all other conditions remaining the same. We evaluated the efficiency of the methodology in solving problems that extend beyond the sensitivity limits of double precision arithmetic. Traditional difference methods, even when combined with semi-analytical solutions, do not provide reliable results in this case, whereas only the new methodology can yield consistent outcomes. We also verified the algorithm for applying the methodology within COMSOL.

The work presents a description of a series of experiments on the interaction of electromagnetic waves with a moving medium. These experiments were carried out using a waveguide transmission line, inside the cavity of which a pipe with moving water was placed. To date, the results of these experiments have not been rigorously interpreted, and we present only a descriptive analysis. Nevertheless, the experiments conducted demonstrate the presence of a reproducible effect and provide substantial information regarding the requirements for designing an optimal study.

The verification of experimental data is one of the priority tasks for future developments. In addition, a number of tasks were identified for generalizing the methodology and expanding its range of applicability as well as for conducting new experiments. In

one group of experiments, the interaction of electromagnetic radiation with a moving gas is planned to be investigated. Another direction involves the design of fundamentally new laboratory setups, the schematics of which are presented in the work. The main tasks of future developments are divided into three areas, systematized, and prioritized according to their complexity and the consistency of the results.

Keywords: time-harmonic propagation, electromagnetic scattering, Born approximations, moving media, bianisotropic media, numerical simulations, waveguide measurements, experiment design, COMSOL

Contents

Appendix

List of Figures

List of Tables

Notations

$\mathbf{A}$	variable matrix (used for notational simplification)
$\mathbf{B}$	magnetic flux density
$\mathbf{D}$	electric displacement
$\mathbf{D}_a$	difference for the electric or magnetic field (target quantity of the classical BA in Section 4.2.2.2)
$\mathbf{D}_e$	difference for the electric field
$\mathbf{D}_m$	difference for the magnetic field
D_s	difference function for S-parameters
$\mathbf{E}$	electric field intensity
$\mathbf{H}$	magnetic field intensity
$\mathbf{I}$	identity matrix
$\mathbf{J}_e$	electric current density
$\mathbf{J}_m$	magnetic current density
L	laboratory reference frame
L'	moving reference frame
R	radius of the numerical computational domain
S_{11}	one of the reflection coefficients of the scattering matrix
S_{21}	one of the transmission coefficients of the scattering matrix
T	oscillation period of the source
T_{obs}	observation time
T_t	propagation time from source to observer
Y	admittance
Z_0	wave impedance of free space
a	radius of the cylinder or pipe
b	β magnitude of order absolute value
c_0	speed of light in free space
d_f	number of frequency steps in TD-FFT solver
d_t	number of time steps in TD solver
f	frequency of a source
f_m	reference frequency for mesh generation in COMSOL
f_s	sampling frequency
$\mathbf{f}_R$	boundary conditions inhomogeneous term
l	length of the scatterer
m	δ magnitude of order absolute value
$\mathbf{n}$	normal vector
n	order of the Born approximation (Chapters 1, 2). Number of medium state measurements in the experiments (Chapter 5).
n_f	total number of frequencies in FFT spectrum
n_{rep}	number of samples per oscillation period

n_s	total number of time samples in TD solver
p	number of circles in the region for native meshing
q	number of layers in the region for native meshing
s	distance between source and observer
$\mathbf{v}$	vector field of linear velocity
v_p	phase velocity
x	one of the Cartesian coordinates
y	one of the Cartesian coordinates
z	one of the Cartesian coordinates and one of the coordinates of the cylindrical system
Ω	computational domain
Ω_s	subregion in Ω occupied by the scatterer
β	relative linear velocity
δ	residual for the iterative solver
ϵ	absolute permittivity
ϵ_r	relative permittivity
ϵ_0	electric constant
ζ	magnetoelectric coupling coefficient
κ	hydraulic coefficient
λ_0	wavelength in free space for f
μ	absolute permeability
μ_r	relative permeability
μ_0	magnetic constant
ξ	electromagnetic coupling coefficient
ρ	radial coordinate of the cylindrical system
σ	electrical conductivity
φ	angular coordinate of the cylindrical system
ω	angular frequency of a source
$\partial\Omega$	computational domain boundary

Acronyms

BA	Born approximation
BCs	boundary conditions
BLDC	brushless direct current
BW	bandwidth
CAD	computer-aided design
EM	electromagnetic
ES	experimental studies
FD	frequency domain
FDTD	finite-difference time-domain method
FE	finite element
FEM	finite element method
FFT	fast Fourier transform
HDPE	high-density polyethylene
IF	intermediate frequency
MG	methodology generalization
RPM	revolutions per minute
STL	standard tessellation language
TD	time domain
TE	transverse electric
TL	transmission line
TM	transverse magnetic
VE	validity enhancement
VNA	vector network analyzer

CHAPTER 1

Introduction

Understanding the interaction between electromagnetic radiation and moving materials, media, and objects is a problem of considerable scientific relevance, with far-reaching implications for modern physics and engineering. Since its inception, this research field has evolved along multiple interconnected directions, driven both by fundamental scientific interest and by the increasing demand for practical applications. These directions encompass theoretical developments, analytical modeling, numerical simulations, and experimental validation, all of which complement and reinforce each other. In this context, it is sufficient to note that this topic combines and integrates such complementary fields as relativistic electrodynamics, diffraction theory, and materials science. Over the years, a vast and meaningful body of knowledge has been established in this scope. Nevertheless, a number of fundamental questions remain unresolved, underscoring the relevance of continued investigation. The present work is devoted to addressing some of these open issues.

Our primary focus is on the effects of material motion on scattered electromagnetic fields. The main research interest is in systems with slowly moving objects, *i.e.*, cases where the characteristic velocity is much smaller than the speed of light. This focus is motivated by an important trend: the threshold for detecting relativistic effects in electrodynamics is rapidly decreasing. This is driven by advances in experimental equipment as well as the emergence of powerful computational approaches. Consequently, the effects of a slowly moving medium on scattered electromagnetic fields can now be observed under laboratory conditions, implying potential practical applications. Reliable analysis methods are essential for validating existing experimental data on these effects.

Furthermore, it is essential to emphasize the second significant aspect of this study. We consider the propagation, scattering, and diffraction of electromagnetic fields in the microwave range. In Fizeau's classical work [1], an experiment is described that can be considered the first (or one of the first) in this direction. In this experiment, the effect of a moving medium on optical-range radiation was investigated. All else being equal,

the effect on microwave radiation turns out to be much smaller in magnitude. For this reason, the original problem in such a formulation remained outside the scope of practical interest for a long time. Research in this area was primarily theoretical. Among the potential applications, particular attention can be given to the development of new types of contactless, non-invasive electromagnetic flowmeters for liquids, gases, and bulk solids as well as velocity profilers for continuous media.

In [2], Van Bladel provides a detailed discussion of various practical applications of relativistic effects. The indication of potential applicability in this context is closely related to the issue of feasibility. Existing numerical methods for analyzing motion effects are stable at velocities close to the speed of light, but their practical use is highly limited, essentially confined to astrophysical studies. In contrast, traditional approaches are ineffective for analyzing the effects of slowly moving materials, despite the fact that the practical applications of such effects can be highly diverse. This work attempts to bridge this gap by providing a consistent and reliable framework for analysis across the full range of velocities.

In the field of electromagnetic flow measurement methods, optical approaches are a subclass [3, 4], with the classical Fizeau-Fresnel type being one of the prominent techniques. This method based on the electromagnetic drag effect [5, 6], which is detected using standard interferometry [4], [5]. Despite its potential, this type of liquid flowmeter has not been widely adopted, primarily due to competition from other optical techniques. However, several advanced flowmetry problems [3] can be addressed by adapting the Fizeau-Fresnel principles from optics to microwaves [7]. The key advantage of this microwave flow measurement method lies in its ability to reconstruct flow and velocity profiles without exerting mechanical influence on the flow. It is important to emphasize that reconstructing the flow velocity profile through direct measurement, without any mechanical impact, currently has no reliable method available [3]. This issue is discussed in Section 1.6.

The Fizeau experiment, which was initially misinterpreted, was later explained with the advent of Einstein's special theory of relativity [8]. For a rigorous electrodynamic description, the classical Maxwell's equations were extended by Minkowski [9]. One of the outcomes of the emerging theory was the refinement of the constitutive relations for moving media. This new class of media and materials was later termed as bianisotropic [10]. New terms representing electro-magnetic and magneto-electric coupling appeared in the constitutive equations of such media. However, the consideration of such material parameters was first proposed by Tellegen in the context of developing new functional

materials and circuit elements [11]. We can conventionally divide the bianisotropy of a medium into artificial, associated with its structural properties, and natural, determined by the state of the medium. Subsequently, the study and application of bianisotropic materials extended beyond the scope of relativistic electrodynamics.

In this work, we only highlight the potential applicability of the developed algorithm for analyzing the effects of bianisotropy in composite or metamaterials. We also point out the fundamental similarities between natural and artificial bianisotropy of media. However, a detailed analysis in the field of materials science is not provided in this study. The focus remains on the methodology for analyzing motion effects. The generality of the formulations within the approach is a key priority. In this context, the Born approximation (BA) methodology proposed in this work represents a novel and highly effective tool, enabling the solution of an entirely new class of electrodynamic problems. Various approaches with certain modifications employ BAs for solving electrodynamic problems can be found across a wide range of applications [12, 13, 14]. In the corresponding section, it will be shown that approaches based on the BA continue to appear, along with specific modifications and improvements that increase the efficiency of solving existing problems and enable the solution of new classes of electrodynamic problems.

The structure of this work follows the classical framework of a scientific study. First, the research problem is clearly defined, highlighting the objectives, scientific novelty, and the specific tasks required to achieve them. Based on this formulation, a methodology is developed that meets all stated requirements. The methodology is then subjected to a comprehensive analysis to determine its key properties, accuracy, and limits of applicability, with particular emphasis on its implementation within a commercial computer-aided design (CAD) system. The subsequent stage involves verification, including comparisons with reliable sources to enhance the external validity of the approach. In parallel, a series of experiments is conducted to observe the effects of motion on scattered electromagnetic fields, with the present work reporting the results and their initial analysis. Finally, the study concludes with a detailed plan for the future development of the research project.

1.1 Problematization

The three key aspects outlined below define the general problem framework of the entire work. First, the object of this study is moving materials with time-invariant boundaries. This means that the set of points forming the boundary between the background medium

and the moving object remains stationary. Along with the requirement that the velocity field inside the object should also be time-independent, and assuming that the incident electromagnetic waves are time-harmonic, we can exclude any temporal effects from consideration and solve the problem in the frequency domain (FD). This does not represent a significant limitation of the approach, since temporal effects are well studied. By excluding them, we can focus on analyzing the target effects associated with the bianisotropy of the moving material.

Secondly, we investigate the influence of a slowly moving material on the electromagnetic field scattered by it. Since the velocity of the object is much smaller than the speed of light in vacuum, this corresponds to a deeply non-relativistic analysis. Relativistic analysis can be carried out using a number of existing techniques; however, their application in the deeply non-relativistic case proves to be almost impossible. The analysis of slowly moving materials is of considerable practical interest. This problematic area underpins the study's novelty and scientific importance.

The third aspect of the problematization is the analysis of the potential for practical application of weak bianisotropy effects in moving materials. Since the analysis is carried out in a deeply non-relativistic regime, the magnitude of the target effects is very small, making them difficult to detect experimentally and to capture through numerical analysis. We aim to develop a stable and flexible analysis algorithm that can be effectively applied to problems involving the direct utilization of these effects. We do not impose restrictions on the possible frequency range for the analysis; however, the primary practical interest lies in microwave scattering from moving bodies.

In summary, we formulate the main scientific question addressed in this work. Is it possible to develop a reliable and efficient method for the analysis of electrodynamic scattering effects due to slowly moving materials, at deeply non-relativistic velocities relevant for practical applications, aimed at conducting multiphysics studies, solving inverse problems, designing new types of flowmeters, and validating obtained experimental data? We are interested in FD effects, in the absence of any time dependence of the scattered field, for an arbitrary velocity vector field and a scatterer of any shape.

1.2 State of the Art

In this section, we will present the current state of the problem in three main aspects closely related to the present work: moving media and moving reference frames, computational

techniques for analyzing bianisotropy effects (including artificial materials and plasma as the main object of studying natural bianisotropy), and developments in the use of Born approximations for solving electrodynamic problems. For this purpose, we carried out a brief review of the most important sources, not older than five years from the time of problematization.

In [15], the rotation of an elastic body under the action of an external electromagnetic field is considered. The authors provide an analysis of the arising ponderomotive forces in a non-inertial reference frame. In the context of the present study, this work serves as an important indication of the complex and intricate nature of such a system, whose full analysis is possible only within the scope of multiphysics modeling. In [16], a fundamental and thorough investigation is presented on the very interesting problem of the interaction between electromagnetic radiation and a moving medium. Among other things, the authors examine the interluminal phenomenon, which corresponds to the Cherenkov regime. This study investigates mainly relativistic effects, since the authors consider linear velocities only a few orders of magnitude below the speed of light. However, the work expands the theoretical foundation of the subject and also points out that the analysis of moving bodies must be multiscale. As an additional example, [17] considers a relativistic problem of the interaction between electromagnetic waves and matter in a high-speed moving reference frame.

In [18], the interaction of electromagnetic radiation with a slowly moving medium is investigated. The problem addressed in this study is closely related to ours. Nevertheless, the work does not carry out a full-wave analysis but instead provides a solution within the well-known ray model to account for the Fresnel drag effect. The authors apply a traditional difference scheme but do not indicate how the issue of loss of accuracy, described in the Section 1.5, is resolved in this case. Furthermore, the authors do not present simulation results obtained using the proposed methodology, which significantly reduces the reproducibility of the method and its practical applicability. Even so, this work is important as it demonstrates the researchers' interest in the topic. In [19], a slowly moving medium containing a source of electromagnetic waves is also considered. This formulation differs fundamentally from ours (see Section 1.3). The study includes analytical derivations, whose main value lies in the examination of electromagnetic wave propagation in a moving medium with nonzero conductivity. The article is of a primarily expository nature and does not propose any specific techniques for the calculation and analysis of motion effects.

In [20], the use of the hybrid boundary element method is proposed for the study of Tellegen-type media. A modified method is described, allowing the solution of a wide range of quasi-static problems in bi-isotropic artificial materials. The study [21] introduces a numerical approach for determining the spectral dyadic Green's function used in the examination of multilayered configurations consisting of periodic bianisotropic layers. The derivation of the Green's function relies on a fully vectorial and rigorous matrix-based framework, constructed upon a generalized transmission-line formulation of Maxwell's equations. A classical approach for solving problems related to calculating the effects of translational motion of a body is the finite-difference time-domain method (FDTD), which received further development in [22]. This method is applied both to relativistic and to slow velocities and has been well established. Nevertheless, within this approach, the only focus is on time-dependent effects associated with changes in the position of the body's boundaries. Such effects generally have a much larger magnitude than the weak bianisotropy effects of a moving medium, and therefore their analysis does not require extreme accuracy. It may be emphasized once again that these effects are well studied, and advances in computational techniques in this area are mainly achieved through optimization and performance improvements, while the accuracy limit is not a significant issue. The FDTD method is also applied in [17] for relativistic velocities. If the method takes into account the Lorentz transformation, which is essential for the problem mentioned, it is usually referred to as the Lorentz-FDTD method. In [17], a moving body of a specific shape in a plasma environment is considered. This can serve as a model of a moving comet with a plasma tail. In [23], the temporal spectra of a signal reflected from moving turbulent plasma are examined. The work addresses numerous time-dependent effects and presents numerical results. Although the technique used is not new, the formulation of the problem is the most general in this scope, making the results of considerable interest.

A fundamental analytical study on nonlocal media, including bianisotropic media, is presented in [24]. The work serves as a major source of knowledge and also provides an extensive review of the topic. Of greatest interest is the investigation of emergent effects arising in complex media. To describe such materials, the authors employ the hydrodynamic Drude model. The central focus of the study is the examination of the uniqueness theorem for the interaction of electromagnetic waves with these media. This work provides a comprehensive overview of approaches to both artificial materials and natural bianisotropy (the latter being of particular interest to us), and it significantly fosters interest in theoretical investigations in this field. The dynamic Drude model for describing

transient effects associated with the propagation of electromagnetic waves in plasma was applied in [25]. The work presents a numerical approach for analyzing the spectra of high-power microwave pulses, based on the Galerkin method for space discretization.

A method for accelerating the convergence of Born series in solving scattering problems involving multiple small bodies was presented in [26]. The acceleration technique proposed by the authors is based on a specific change of variables, which improves the efficiency of scattering analysis without increasing the algorithmic complexity of the method. It should be noted that this work addresses a completely different class of problems, based on the Neumann series and Taylor expansion. The inverse Born method, combined with artificial neural networks, was proposed for solving inverse scattering problems in [27]. The inverse Born method is used to reconstruct the parameters of the scatterer, while employing the same field approximation approach as the direct method and thus sharing its limitations. A key feature of the method is the requirement to search for an optimal solution at each iteration of the procedure. The use of classification neural networks in this part of the algorithm significantly enhances its overall efficiency and accuracy. Work [28] continues the development of integrating machine learning into the Born approximation. In this study, the authors propose a solution to a principal limitation of the effective application of the Born approximation, namely, the requirement of small scattered field magnitude, by demonstrating a possible approach to the problem of non-weak scattering. This work represents a substantial and comprehensive attempt to overcome the main accuracy barrier of this methodology. Nevertheless, it is not highly relevant to our study, since we are concerned with weak effects whose small magnitude is the objective rather than a limitation.

1.3 Generalities

The most general formulation of the problem is consistent with classical relativistic electrodynamics. The reference frames and the orientation of objects within them are shown in Figure 1.1. The laboratory reference frame L is stationary; it contains both the electromagnetic wave source (black square) and the observer (black circle). Within this reference frame, there is a moving object V and an associated reference frame L', relative to which the object is at rest (the boundaries of the object V are also stationary in the frame L). The reference frame L' may be either inertial or non-inertial, with a velocity vector field $\mathbf{v}$. The observation of the effect in frame L is related to the analysis of electromagnetic waves

scattered by the object. It should be noted that if L' is a non-inertial reference frame, Lorentz transformations are possible only if a local inertial reference frame is defined. We will not present here the well-known Lorentz transformations (these can be found for all relevant electrodynamic quantities in [2]).

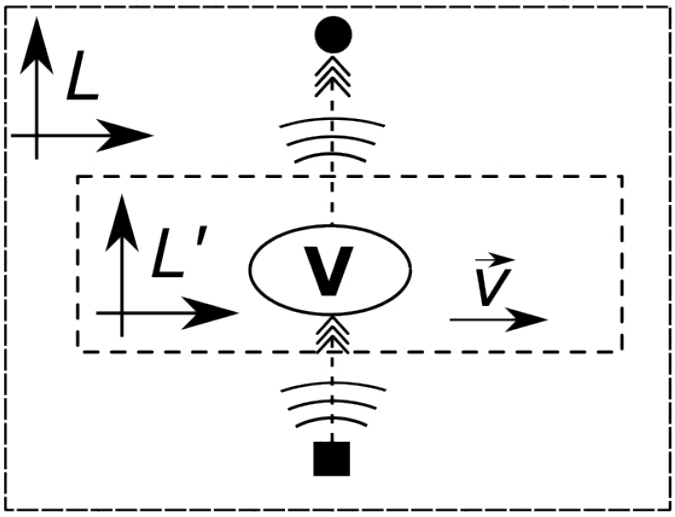

Figure 1.1: Mutual orientation and reference frames in the problem.

The constitutive parameters of a moving material, which in its rest state is non-conducting and isotropic, are [29]

$$\begin{aligned} \mathbf{D} &= \epsilon_0\epsilon_r\mathbf{E} + \epsilon_0\epsilon_r\alpha\, v^2\,[(\hat{v}\times\mathbf{E})\times\hat{v}] + \alpha v\,(\hat{v}\times\mathbf{H}), \\ \mathbf{B} &= \mu_0\mu_r\mathbf{H} + \mu_0\mu_r\alpha\, v^2\,[(\hat{v}\times\mathbf{H})\times\hat{v}] - \alpha v\,(\hat{v}\times\mathbf{E}), \end{aligned} \tag{1.1}$$

where velocity vector $\mathbf{v} = v\hat{v}$ and $\alpha = \frac{\epsilon_r\mu_r - 1}{c_0^2 - \epsilon_r\mu_r v^2}$. Here and throughout the work, traditional notations are used for electrodynamic quantities $\mathbf{E}$, $\mathbf{H}$, $\mathbf{D}$, $\mathbf{B}$, ϵ_r, μ_r and constants ϵ_0, μ_0 and c_0 (follow standard Maxwell's equations). The classical constitutive equations for a bianisotropic medium are given below

$$\begin{aligned} \mathbf{D} &= \epsilon\mathbf{E} + \xi\mathbf{H}, \\ \mathbf{B} &= \zeta\mathbf{E} + \mu\mathbf{H}. \end{aligned} \tag{1.2}$$

By comparing (1.1) and (1.2), one can easily identify a direct analogy between the quantities. In order to determine the bianisotropic parameters of the moving medium, let us denote its material parameters in L' as ϵ^v and μ^v, while coupling coefficients ξ and ζ are equal to zero when the medium is at rest, and therefore it is unnecessary to

introduce additional notation for them. Thus, we emphasize that the weak bianisotropy effects analyzed in the present work are associated with the material parameters $(\epsilon^v - \epsilon)$, $(\mu^v - \mu)$, ξ and ζ.

Expand double vector product as ($\otimes$ is for vector outer product)

$$\begin{aligned}(\hat{v} \times \mathbf{A}) \times \hat{v} = \mathbf{A} - \hat{v}\,(\hat{v} \cdot \mathbf{A}) = \\ \mathbf{I}\mathbf{A} - (\hat{v} \otimes \hat{v})\,\mathbf{A} = [\mathbf{I} - (\hat{v} \otimes \hat{v})]\,\mathbf{A}.\end{aligned} \tag{1.3}$$

Now, for (1.1) we have

$$\begin{aligned}\mathbf{D} &= \epsilon_0\epsilon_r\mathbf{E} + \epsilon_0\epsilon_r\alpha\, v^2\,[\mathbf{I} - (\hat{v} \otimes \hat{v})]\,\mathbf{E} + \alpha v\,(\hat{v} \times \mathbf{H})\,, \\ \mathbf{B} &= \mu_0\mu_r\mathbf{H} + \mu_0\mu_r\alpha\, v^2\,[\mathbf{I} - (\hat{v} \otimes \hat{v})]\,\mathbf{H} - \alpha v\,(\hat{v} \times \mathbf{E})\,.\end{aligned} \tag{1.4}$$

By comparing with (1.2), we immediately express the permeabilities as

$$\begin{aligned}\epsilon^v &= \epsilon_0\epsilon_r\left[1 + \alpha v^2\,[\mathbf{I} - (\hat{v} \otimes \hat{v})]\right], \\ \mu^v &= \mu_0\mu_r\left[1 + \alpha v^2\,[\mathbf{I} - (\hat{v} \otimes \hat{v})]\right].\end{aligned} \tag{1.5}$$

Now let us write the result of the vector product in terms of its components

$$(\hat{v} \times \mathbf{A})_i = \sum_{j,k} \epsilon_{i,j,k} \left(\frac{\mathbf{v}}{v}\right)^j A^k, \tag{1.6}$$

where $\epsilon_{i,j,k}$ is the Levi-Civita symbol. From (1.1) and (1.2) we have

$$\begin{aligned}\xi_{i,k} &= \alpha v \sum_j \epsilon_{i,j,k} \left(\frac{\mathbf{v}}{v}\right)^j, \\ \zeta_{i,k} &= -\alpha v \sum_j \epsilon_{i,j,k} \left(\frac{\mathbf{v}}{v}\right)^j.\end{aligned} \tag{1.7}$$

If the velocity vector is given by its components as $\mathbf{v} = \left(v_x, v_y, v_z\right)$, then

$$\xi = -\zeta = \alpha v \begin{pmatrix} 0 & \frac{-v_z}{v} & \frac{v_y}{v} \\ \frac{v_z}{v} & 0 & \frac{-v_x}{v} \\ \frac{-v_y}{v} & \frac{v_x}{v} & 0 \end{pmatrix} = \alpha \begin{pmatrix} 0 & -v_z & v_y \\ v_z & 0 & -v_x \\ -v_y & v_x & 0 \end{pmatrix}. \tag{1.8}$$

Apart from expressing the complete material equations through the coefficients ϵ, μ, ξ, ζ, an alternative formulation exists [10]. It is given below

$$\begin{cases} \mathbf{D} = \dfrac{P}{c_0}\mathbf{E} + L\mathbf{B}, \\ \mathbf{B} = M\mathbf{E} + c_0 Q\mathbf{B}. \end{cases} \tag{1.9}$$

If the classical electrophysical parameters of the medium ϵ, μ, ξ, ζ are not directly related to the value of $\mathbf{v}$, then P, Q, L, M coefficients were specifically derived to simplify the formulation of material equations for a moving medium. It is straightforward to derive the transformation formulas for these quantities

$$\begin{aligned} \epsilon &= \frac{1}{c_0}\left(P - LQ^{-1}M\right), \\ \xi &= \frac{1}{c_0}LQ^{-1}, \\ \zeta &= -\frac{1}{c_0}Q^{-1}M, \\ \mu &= \frac{1}{c_0}Q^{-1}. \end{aligned} \tag{1.10}$$

A detailed derivation of the P, Q, L, M matrices is provided in [30]. We also present below the inverse transformation formulas

$$\begin{aligned} P &= c_0\left(\epsilon - \frac{\xi\zeta}{\mu}\right), \\ L &= \frac{\xi}{\mu}, \\ M &= -\frac{\zeta}{\mu}, \\ Q &= \frac{1}{c_0\mu}. \end{aligned} \tag{1.11}$$

In summary, the direct relationship between (1.1) and (1.2) substantiates the idea that was already briefly touched upon at the beginning of the chapter. A noticeable difference between the two possible types of bianisotropy (artificial and natural) becomes evident. Artificial bianisotropy is a deliberate effect engineered in functional materials, such as metamaterials. Natural bianisotropy, on the other hand, is an unavoidable effect that arises even in simple media under specific conditions, such as motion. This analogy is crucial

for us because advancements in the analysis of natural bianisotropy can be directly applied to studying materials that exhibit artificial bianisotropy.

1.4 Classical Born Approximation

The Born series, originating from the work of Max Born in the 1920s, represents one of the classical approaches to scattering theory. It was initially formulated as a means of solving the Lippmann–Schwinger equation within the quantum mechanical framework of scattering [31]. Truncating the full series of successive corrections at a certain point is referred to as the Born approximation. A detailed description of the classical Born approximation for solving electrodynamic scattering problems is provided in [32, chap. 1, sec. 3.2]. Here, we present only the expressions relevant to the present work, which have been modified for the synthesis of the new methodology in Chapter 2. To this end, we first formulate the scattering problem.

Let us consider a body of arbitrary shape, size, and dielectric permittivity, subjected to an incident electromagnetic wave. The problem consists in determining the fields scattered by the body. The exact values of the equivalent currents in the case of substituting the scatterer with a source are as follows:

$$\begin{aligned} \mathbf{J}_{e,eq} &= j\omega \left(\epsilon - \epsilon^0\right) \mathbf{E}^{tot}, \\ \mathbf{J}_{m,eq} &= j\omega \left(\mu - \mu^0\right) \mathbf{H}^{tot}. \end{aligned} \tag{1.12}$$

Expression (1.12) can be interpreted as an equivalence principle. In this case, the presence of the scatterer represents a perturbation of the system. Thus, ϵ^0 and μ^0 are the parameters of the background medium in which the scatterer is placed, while ϵ and μ are the parameters of scatterer material. The total field quantities are the vector sum of the incident and scattered fields $\mathbf{E}^{tot} = \mathbf{E}^{inc} + \mathbf{E}^{sc}$, similarly, for $\mathbf{H}^{tot}$. The concept of the first approximation lies in the following:

$$\begin{aligned} \mathbf{J}_{e,eq,ba,1} &\approx j\omega \left(\epsilon - \epsilon^0\right) \mathbf{E}^{inc}, \\ \mathbf{J}_{m,eq,ba,1} &\approx j\omega \left(\mu - \mu^0\right) \mathbf{H}^{inc}. \end{aligned} \tag{1.13}$$

A necessary and sufficient condition for such an approximation is $\mathbf{E}^{sc} \to 0$ and $\mathbf{H}^{sc} \to 0$ (in direct problems, these quantities are unknown). From which, it follows that $\mathbf{E}^{tot} \approx \mathbf{E}^{inc}$ and $\mathbf{H}^{tot} \approx \mathbf{H}^{inc}$, hence expressions (1.12) and (1.13) acquire a complete mutual interpretation.

Physically, this means that in the field of incident waves, the object exerts a small magnitude effect of electromagnetic waves diffraction. It should be noted that the Born approximation does not require the body to be small in size. A scatterer is considered tenuous if its permittivity is close to that of the surrounding medium. The more strongly this condition is satisfied, the better the (1.13) approximation. Nevertheless, according to recent studies, this condition can be significantly weakened while maintaining an acceptable level of approximation in a wide range of electrodynamics problems (see Section 1.2).

The fields generated by sources (1.13) act as the first-order approximation of the required fields $\mathbf{E}_{ba,1} \approx \mathbf{E}^{sc}$ and $\mathbf{H}_{ba,1} \approx \mathbf{H}^{sc}$. Thus, the second-order approximation enhances accuracy and is expressed as

$$\begin{aligned} \mathbf{J}_{e,eq,ba,2} &\approx j\omega \left(\epsilon - \epsilon^0\right) \left(\mathbf{E}^{inc} + \mathbf{E}_{ba,1}\right), \\ \mathbf{J}_{m,eq,ba,2} &\approx j\omega \left(\mu - \mu^0\right) \left(\mathbf{H}^{inc} + \mathbf{H}_{ba,1}\right). \end{aligned} \tag{1.14}$$

Thus, we obtain a potentially infinite series of successive approximations (Born series). With n being the order of BA, we can state that $\mathbf{E}_{ba,n\to\infty} = \mathbf{E}^{sc}$ and $\mathbf{H}_{ba,n\to\infty} = \mathbf{H}^{sc}$, which implies that $\left(\mathbf{E}^{inc} + \mathbf{E}_{ba,n\to\infty}\right) = \mathbf{E}^{tot}$ (similarly, for the magnetic field). And we reach the equivalence principle (1.12).

1.5 Traditional Difference Methods

A classical approach for analyzing the effects of media motion on electromagnetic fields is to consider the difference between the two states of the system. One state 0 corresponds to the medium at rest, and the other state 1 corresponds to the medium in motion. The scattering of electromagnetic waves by the object in both states can be computed using various techniques. The author is not aware of any problem that has a solution for state 1 but not for state 0, while the reverse situation occurs fairly often. This is related to the principle, according to which, at $\mathbf{v} = 0$, the solution for state 1 is equivalent to the solution for state 0 [33]. Thus, the availability of a solution for the madia in motion state determines the applicability of the difference method.

Traditional difference methods become highly unreliable when the effect is very small compared to the magnitudes of the subtracted quantities. In such cases, numerical round-off errors, bounded by the machine epsilon of the computational system, may become comparable to or even larger than the true effect. As a result, the relative error of the

estimate can grow dramatically, making it difficult to detect weak effects. As will be demonstrated in Chapter 4, even if both system states are computed using semi-analytical methods, which are generally assumed to provide minimal possible error, the subtraction of two quantities of nearly equal magnitude often introduces an irreducible error.

One possible approach to mitigating this error is the use of arbitrary-precision arithmetic and big-float numbers. Naturally, both the algorithmic and memory complexity of the solution increase significantly; however, for semi-analytical approaches this may still represent a reasonable choice. However, if the analysis of the two system states is carried out using numerical methods such as finite element method (FEM) or FDTD, the use of arbitrary-precision arithmetic may become impractical from the standpoint of performance. Moreover, to the best of the authors' knowledge, no commercial or publicly available electromagnetic solvers currently support arithmetic operations with such precision. It should also be noted that in many electromagnetic simulations the dominant sources of error are not arithmetic limitations, but rather discretization effects, boundary conditions (BCs) modeling, material property approximations, and mesh non-uniformities [34]. As a result, increasing arithmetic precision beyond standard double precision often provides little improvement in the overall accuracy of the simulation.

Notably, difference method was applied by De Zutter for the analytical solution of the scattering problem on a rotating sphere [35]. The analytical solution for a rotating cylinder was also obtained by De Zutter [36]. Bladel considered a rotating disk and spheroid in [37]. Analytical solutions for a cylinder moving along its axis were obtained earlier [38, 39]. In addition to the aforementioned problems, analytical solutions also exist for a moving infinite half-space [40] and for a moving infinite boundary [41]. In the context of present work, using the traditional difference, an analytical approach was developed to analyze the influence of motion on the electromagnetic field scattered by a moving dielectric slab [42]. A semi-analytical approach for a multilayered cylinder moving along its axis is presented in [43].

There are several numerical approaches that allow solving problems involving a moving medium. The most advanced of these have already been reviewed in Section 1.2. Their number is complemented by earlier developments. As an example, we present only a small subset of them, those relevant to the present work. Various techniques for solving problems in the time domain (TD) are presented in [44, 45, 46]. FEM was applied to solve the scattering problem for an axially moving cylinder in [47]. Fast and simple method for analyzing first order motion effects, which can be used to obtain initial results, is presented in [48]. The traditional difference method is directly employed in [49, 50, 51].

1.6 Practical Relevance of the Research

At the beginning of this chapter, we have already described in detail the possible applications of the conducted study. To be more specific and to illustrate the overall picture of motion effects encountered in technical applications, we present a summary information in Table 1.1. The table lists possible situations and applications involving a moving medium. In some cases, the motion is rotational, while in others, it is translational. We present characteristic velocities – that is, typical values of the magnitude relevant to each specific application. The characteristic angular velocity of rotation is denoted by Ω_{char}, and the characteristic linear velocity by v_{char}.

Let us now introduce a quantity that is of fundamental importance for the present study, namely the relative linear velocity of the media, denoted as β. By definition, the quantity $\beta = \frac{|\mathbf{v}|}{c_0}$. This scalar field determines the magnitude of the motion effects. Characteristic value β_{char} is a representative quantity used to describe the generic kinematic properties of a system and to estimate typical scale of motion inherent to the considered application. It is not necessarily the average or maximum β but rather indicates the order of magnitude. Let us note, that first-order effects are controlled by β, while second-order effects are controlled by β^2. To estimate the value of β_{char} for rotational motion, in all cases presented in Table 1.1, the radius of the rotating body is assumed to be 20 cm.

Thus, within the scope of potential applications, the value of β_{char} varies in the range from approximately $(0 \div 10^{-3}]$. Let us introduce a heuristic classification for the entire range of variation of the parameter $\beta \in (0 \div 1)$. Slow motion $\beta_{slow} \in \left(0 \div 10^{-6}\right]$ refers to velocities that are easily achievable under laboratory and industrial conditions and are commonly encountered in technological processes. The upper bound may correspond to linear velocities on the surfaces of rotating rotors in compact turbojet engines or gas turbine blades. Relativistic speed subrange $\beta_{rel} \in [0.01 \div 1)$. Obviously, studying this subrange is mainly of theoretical and fundamental interest, since the effects of general and special relativity become significant. The remaining subrange covers intermediate velocity values, hence $\beta_{int} \in \left(10^{-6} \div 0.01\right)$. The main applications within this range are primarily related to space research and the study of electromagnetic wave propagation in cosmic environments [52]. It should also be noted that for motion (and especially for rotation) of matter, the entire range of the β is bounded from above by limit determined by the material parameters of the media (see [30, 50, 53]). Within the scope of the present study, this limit is not significant and is therefore omitted from consideration.

Table 1.1: Characteristic values of linear and relative velocities for various applications.

Object	Ω_{char}, RPM	v_{char}, m/s	β_{char}
Arterial blood in humans	none	0.4	1.3×10^{-9}
Water in a tap hydraulic system	none	1.5	5.0×10^{-9}
Household fan	1200	25.1	8.4×10^{-8}
Generator turbine	3000	62.8	2.1×10^{-7}
Gas in pneumatic systems	none	75.0	2.5×10^{-7}
Dust tail of a comet	none	100.0	3.3×10^{-7}
Car engine shaft	6000	125.7	4.2×10^{-7}
BLDC motor	50000	1047.2	3.5×10^{-6}
High-speed BLDC motor	100000	2094.4	7.0×10^{-6}
Exhaust velocity of a liquid-fueled engine	none	2500.0	8.3×10^{-6}
Plasma tail of a comet	none	5×10^5	0.0017

Let us describe a specific application of the new BA methodology to a practically significant problem. In the measurement of liquid or gas flows in pipes, one of the key challenges is the reconstruction of the flow velocity profile [3]. This issue is particularly critical in industrial settings, as accurate estimation of the flow rate of a given substance improves process efficiency and contributes to sustainable development. A traditional approach to measuring the flow profile of a liquid involves installing a sensor array directly inside the pipe [54]. Such an invasive method has notable drawbacks, the primary one being that the sensor array distorts the flow profile, due to blockage and turbulence caused by the sensor structure. Moreover, this approach is limited when applied to multiphase flows or to the measurement of gas velocity profiles. An alternative approach is electromagnetic probing of moving media in weakly conducting pipes. This technique is remote, non-destructive, and non-invasive. By obtaining information about the field scattered by the moving medium at the receiver, and employing effective computational tools to analyze the effects of motion, it becomes possible to reconstruct the flow parameters of interest. It is

also important to note that, in most cases, time-dependent effects caused by transverse pipe displacement do not carry useful information about the axial flow velocity. Finally, the experimental setup described in Chapter 5 and used to validate the proposed methodology represents a laboratory prototype of a waveguide-based system for remote electromagnetic measurement of liquid flow velocity.

In summary, the low-velocity range β_{slow} is of the greatest interest for practical applications. Existing numerical approaches for modeling the interaction of electromagnetic waves with moving media are largely inadequate for $\beta \in \beta_{slow}$ (see explanations provided in Section 1.5). This limitation makes it clear that, without a robust method for solving the direct scattering problem, it is impossible to reliably address the corresponding inverse problem, detect weak effects of motion, restore velocity fields, design new experiments, or develop devices based on the obtained results. Consequently, the development of efficient and accurate methods for studying electrodynamic scattering in moving media remains a critical challenge. To address this challenge, we employ the novel BA approach.

CHAPTER 2

Born Approximations for Modeling EM Effects of Moving Materials

2.1 Formulation of the Main Problems

Figure 2.1 illustrates the geometry of the system as well as the main entities involved in the problem formulation. The system comprises a closed domain Ω with a continuous boundary $\partial\Omega$ that outlines the region for numerical analysis. Inside this domain, there is a confined subregion Ω_s with electrophysical properties distinct from the background medium. Within this subregion, a vector field of linear velocities $\mathbf{v}$ governs the motion of the medium, while its boundaries remain unchanged.

The following system of equations holds for the given problem in general form

$$\begin{cases} \operatorname{curl}\mathbf{H} - j\omega\mathbf{D} = \mathbf{J}_e & \text{in } \Omega, \\ \operatorname{curl}\mathbf{E} + j\omega\mathbf{B} = -\mathbf{J}_m & \text{in } \Omega, \\ \mathbf{D} = \epsilon\mathbf{E} + \xi\mathbf{H} & \text{in } \Omega, \\ \mathbf{B} = \zeta\mathbf{E} + \mu\mathbf{H} & \text{in } \Omega, \\ \mathbf{H}\times\mathbf{n} - Y\,(\mathbf{n}\times\mathbf{E}\times\mathbf{n}) = \mathbf{f}_R & \text{on } \partial\Omega. \end{cases} \tag{2.1}$$

$\mathbf{J}_e$ and $\mathbf{J}_m$ are the densities of electric and magnetic currents, respectively. ϵ, μ, ξ, ζ are the material parameters of the bianisotropic media (see Sections 1.3 and 1.4). The problem is defined by BCs, where $\mathbf{n}$ is the outward normal vector to $\partial\Omega$, Y is the scalar complex admittance and $\mathbf{f}_R$ is the BCs inhomogeneous term. BCs in equation (2.1) are formulated using the conventional notation for three-dimensional problems and, owing to its generality, applies to both open (radiation or scattering) and closed (cavity) problems. The latter statement is particularly important for us in the context of verifying the conducted experiments (see Chapter 5).

The material of this chapter is based on the publication [55]. The content of Section 2.3 was presented at the XXV Riunione Nazionale di Elettromagnetismo (RINEM) conference add held in Viareggio, Italy, on October 2024.

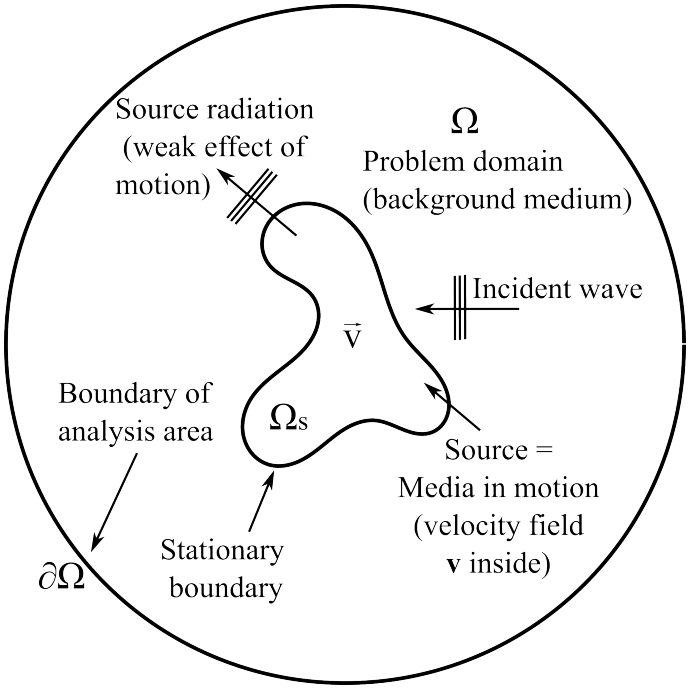

Figure 2.1: The incident field, produced by a primary source, defines the electromagnetic scattering problem. To analyze the effects of motion, the scatterer is substituted with an equivalent source, and the incident field is excluded from the analysis. The figure illustrates an example with a single scatterer; however, this does not impose any limitation, as multiple scatterers may be present within Ω.

If $\mathbf{v} = 0$ the problem is formulated as follows:

$$\begin{cases} \operatorname{curl} \mathbf{H}_0 - j\omega \mathbf{D}_0 = \mathbf{J}_e & \text{in } \Omega, \\ \operatorname{curl} \mathbf{E}_0 + j\omega \mathbf{B}_0 = -\mathbf{J}_m & \text{in } \Omega, \\ \mathbf{D}_0 = \epsilon^0 \mathbf{E}_0 & \text{in } \Omega, \\ \mathbf{B}_0 = \mu^0 \mathbf{H}_0 & \text{in } \Omega, \\ \mathbf{H}_0 \times \mathbf{n} - Y\,(\mathbf{n} \times \mathbf{E}_0 \times \mathbf{n}) = \mathbf{f}_R & \text{on } \partial\Omega, \end{cases} \tag{2.2}$$

Here and throughout, $\mathbf{E}_0$, $\mathbf{H}_0$, $\mathbf{D}_0$, $\mathbf{B}_0$, ϵ^0, μ^0 are the corresponding quantities defined when all media are at rest. Thus, the media at rest in the subregion Ω_s are isotropic and non conducting. Analyzing expressions (2.1) and (2.2), the primary and sole difference is the emergence of the bianisotropy of the moving media. To maintain a complete analogy, it can be stated that $\xi^0 = 0$ and $\zeta^0 = 0$.

The difference fields, denoted as $\mathbf{D}_e = \mathbf{E} - \mathbf{E}_0$ and $\mathbf{D}_m = \mathbf{H} - \mathbf{H}_0$ represent the effects of motion. These are the fields we aim to compute. By performing the subtraction of

problems (2.1) and (2.2) and carrying out the standard mathematics for such a case [56, p. 328], the formulation reduces to the following:

$$\begin{cases} \text{curl}\, \mathbf{D}_m - j\omega\epsilon^0 \mathbf{D}_e = \mathbf{J}_{e,eq} & \text{in } \Omega, \\ \text{curl}\, \mathbf{D}_e + j\omega\mu^0 \mathbf{D}_m = -\mathbf{J}_{m,eq} & \text{in } \Omega, \\ \mathbf{D}_m \times \mathbf{n} - Y\,(\mathbf{n} \times \mathbf{D}_e \times \mathbf{n}) = 0 & \text{on } \partial\Omega, \end{cases} \tag{2.3}$$

It is important to note that problem (2.3) does not involve bianisotropic media and can be solved by traditional electromagnetic simulators.

The current densities in (2.3) are unknown by definition. They are given by the following expressions:

$$\begin{aligned} \mathbf{J}_{e,eq} &= j\omega \left(\epsilon - \epsilon^0\right) \mathbf{E} + j\omega\xi\mathbf{H}, \\ \mathbf{J}_{m,eq} &= j\omega \left(\mu - \mu^0\right) \mathbf{H} + j\omega\zeta\mathbf{E}. \end{aligned} \tag{2.4}$$

In the first-order BA, we approximate them, respectively, by the fields $\mathbf{J}_{e,eq,ba1}$ and $\mathbf{J}_{m,eq,ba1}$, where:

$$\begin{aligned} \mathbf{J}_{e,eq,ba1} &= j\omega \left(\epsilon - \epsilon^0\right) \mathbf{E}_0 + j\omega\xi\mathbf{H}_0, \\ \mathbf{J}_{m,eq,ba1} &= j\omega \left(\mu - \mu^0\right) \mathbf{H}_0 + j\omega\zeta\mathbf{E}_0. \end{aligned} \tag{2.5}$$

These equivalent sources are known and for most problems of engineering interest they provide very good approximations of $\mathbf{J}_{e,eq}$ and $\mathbf{J}_{m,eq}$. By considering problem (2.3) with the source terms $\mathbf{J}_{e,eq}$ and $\mathbf{J}_{m,eq}$ replaced by $\mathbf{J}_{e,eq,ba1}$ and $\mathbf{J}_{m,eq,ba1}$, one can obtain reliable approximations of $\mathbf{D}_e$ and $\mathbf{D}_m$, and consequently estimate the effects of motion in relevant applications. Denote these approximate solutions by $\mathbf{D}_{e,ba1}$ and $\mathbf{D}_{m,ba1}$. By recursion, the expressions for the equivalent sources in the second-order approximation are obtained as follows:

$$\begin{aligned} \mathbf{J}_{e,eq,ba2} &= j\omega \left(\epsilon - \epsilon^0\right) \left(\mathbf{E}_0 + \mathbf{D}_{e,ba1}\right) + j\omega\xi \left(\mathbf{H}_0 + \mathbf{D}_{m,ba1}\right), \\ \mathbf{J}_{m,eq,ba2} &= j\omega \left(\mu - \mu^0\right) \left(\mathbf{H}_0 + \mathbf{D}_{m,ba1}\right) + j\omega\zeta \left(\mathbf{E}_0 + \mathbf{D}_{e,ba1}\right). \end{aligned} \tag{2.6}$$

We now draw important analogies between the new method and the classical Born approximation (see Section 1.4) and highlight the key differences. In both cases, the effect of a perturbation in the system is taken into account in the equivalent source formulations

through the medium parameters. In the classical approximation, the perturbation is the presence of the scatterer itself, thus, $\left(\epsilon - \epsilon^0\right) \neq 0$ and $\left(\mu - \mu^0\right) \neq 0$ serve as a direct indication of this. Within the new methodology, the perturbation is the motion of the scatterer, and this is indicated by $\mathbf{v} \neq 0$. And due to the fact that the motion velocity modifies the material parameters of the medium (see Section 1.3), we can express this perturbation in a similar form, but with the addition of two new terms ξ and ζ. Even at relativistic velocities, the perturbation of the media (particularly in radio-transparent cases) may remain small, and the new Born approximation can yield acceptable results. However, in the deeply non-relativistic regime, the smallness of the perturbation is guaranteed, making the new approach highly effective. A more detailed assessment of the method's applicability is provided in Section 2.4.2.

2.2 Weak Formulation of the Problem

We are looking for a solution to the problem formulated as shown in [57, eq. (3.7)]. The problem is defined as follows:

$$\text{find } \mathbf{D}_e \in U : a(\mathbf{D}_e, \mathbf{u}) = l(\mathbf{u}), \forall \mathbf{u} \in U, \tag{2.7}$$

where

$$\begin{aligned} U &= \left\{\mathbf{u} \in H(\text{curl}, \Omega) \mid \mathbf{u} \times \mathbf{n} \in L_t^2(\partial\Omega)\right\}, \\ H(\text{curl}, \Omega) &= \left\{\mathbf{u} \in [L^2(\Omega)]^3 \mid \text{curl}\mathbf{u} \in [L^2(\Omega)]^3\right\}. \end{aligned} \tag{2.8}$$

A similar problem is formulated for the quantity $\mathbf{D}_m$. Here and in the following, if in an expression the quantity $\mathbf{D}_e$ can be replaced by $\mathbf{D}_m$ without affecting its validity, we use a subscript 'a' for the sake of brevity. Considering that the scalar products are defined as $(\mathbf{D}_a, \mathbf{u})_{0,\Omega} = \int_\Omega \mathbf{u}^* \mathbf{D}_a \, dV$ and $(\mathbf{D}_a, \mathbf{u})_{0,\partial\Omega} = \int_{\partial\Omega} \mathbf{u}^* \mathbf{D}_a \, dS$.

To demonstrate the conciseness of the proposed method, we first write down the most general weak form of the given problem [57]. It is presented below

$$
\begin{aligned}
a(\mathbf{D}_a, \mathbf{u}) = c_0 &\int_\Omega (\mathrm{curl}\mathbf{u})^* Q(\mathrm{curl}\mathbf{D}_a)\, dV \\
&- \frac{\omega^2}{c_0} \int_\Omega \mathbf{u}^* P \mathbf{D}_a\, dV \\
&- j\omega \int_\Omega \mathbf{u}^* M(\mathrm{curl}\mathbf{D}_a)\, dV \\
&- j\omega \int_\Omega (\mathrm{curl}\mathbf{u})^* L \mathbf{D}_a\, dV \\
&+ j\omega \int_{\partial\Omega} (\mathbf{n}\times\mathbf{u}\times\mathbf{n})^* Y(\mathbf{n}\times\mathbf{D}_a\times\mathbf{n})\, dS,
\end{aligned}
\tag{2.9}
$$

$$
\begin{aligned}
l(\mathbf{u}) = &- j\omega \int_\Omega \mathbf{J}^*_{e,eq,ba}\mathbf{u}\, dV \\
&- c_0 \int_\Omega (\mathrm{curl}\mathbf{u})^* Q \mathbf{J}_{m,eq,ba}\, dV \\
&+ j\omega \int_\Omega \mathbf{J}^*_{m,eq,ba} L\mathbf{u}\, dV \\
&- j\omega \int_{\partial\Omega} \mathbf{f}^*_R(\mathbf{n}\times\mathbf{u}\times\mathbf{n})\, dS,
\end{aligned}
\tag{2.10}
$$

where $(\cdot)^*$ denotes the conjugate transpose of the corresponding vector.

If in (2.9) the quantity $\mathbf{D}_a$ is replaced by $\mathbf{E}$, we obtain the standard scattering problem for a bianisotropic material at rest, which has been considered in numerous related studies (*e.g* in [30, 49, 57]). However, as previously noted, the system (2.3) does not require the material to be characterized as bianisotropic, while it retains the properties it had in the rest state. If the medium at rest of the subregion is isotropic, it follows from equations (1.11) that $\xi = \zeta = L = M = 0$. Additionally, the expression (2.10) is simplified by the fact that the inhomogeneous term $\mathbf{f}_R$ in the boundary conditions, according to (2.3), is also equal to zero. Hence,

$$
\begin{aligned}
a(\mathbf{D}_a, \mathbf{u}) = &\int_\Omega (\mathrm{curl}\mathbf{u})^* \frac{1}{\mu^0} (\mathrm{curl}\mathbf{D}_a)\, dV \\
&- \omega^2 \int_\Omega \mathbf{u}^* \epsilon^0 \mathbf{D}_a\, dV \\
&+ j\omega \int_{\partial\Omega} (\mathbf{n}\times\mathbf{u}\times\mathbf{n})^* Y(\mathbf{n}\times\mathbf{D}_a\times\mathbf{n})\, dS,
\end{aligned}
\tag{2.11}
$$

$$
\begin{aligned}
l(\mathbf{u}) = &- j\omega \int_{\Omega} \mathbf{u}^{*} \mathbf{J}_{e,eq,ba}\, dV \\
&- \int_{\Omega} (\mathrm{curl}\mathbf{u})^{*} \frac{1}{\mu^{0}} \mathbf{J}_{m,eq,ba}\, dV.
\end{aligned}
\tag{2.12}
$$

It is clearly seen that expressions (2.11) and (2.12) are much simpler than expressions (2.9) and (2.10). This is an important aspect that allows us to assess the complexity of the new approach, which will be carried out in Section 2.4.1. Moreover, in this case, the problem does not require a specific treatment (as is the case when bianisotropy parameters of the medium are involved), which significantly improves the accuracy of the obtained solution [58].

2.3 Implementation of the Methodology in Native FE Solver

To carry out a comprehensive analysis, assessment, and verification of the new methodology, we applied it within a native FEM solver. In this context, "native" refers to our own solver, whose code is fully under our control. This solver has been employed in numerous works of our research group [55, 57, 58] and, while offering a number of undeniable advantages, its use also comes with significant limitations. One of the main limitations is the absence of a powerful mesh generator, which restricts the computational meshes to trivial geometries. This limitation was overcome by developing a system for importing mesh geometries into the native solver, with the meshes being generated in commercial CAD software. This process is described in the Appendix A.

Figure 2.2 shows a diagram of the proposed procedure. At the beginning, geometry, mesh, boundary conditions and solver parameters are specified. Then the solution is calculated in the case of zero velocity of the object (see (2.2)). The resulting field solution is stored in memory. Further, it is used in the procedure for finding field values at the centres of gravity of elements that belong to the subdomains occupied by media in motion (Ω_s). Next, the calculation of equivalent currents is carried out. The first iteration determines the first order of approximation ($n = 1$), the second iteration determines the second order ($n = 2$), *et cetera*. The magnitude of the effect of motion determined by the relative linear velocity β (see Section 1.6) is used only in this procedure and acts in it as an input, *a priori* parameter. By definition, β is a scalar field that equals zero everywhere outside the domain Ω_s and is nonzero almost everywhere within Ω_s. When this quantity is defined through a specific value, it implies that the velocity field is uniform. It should

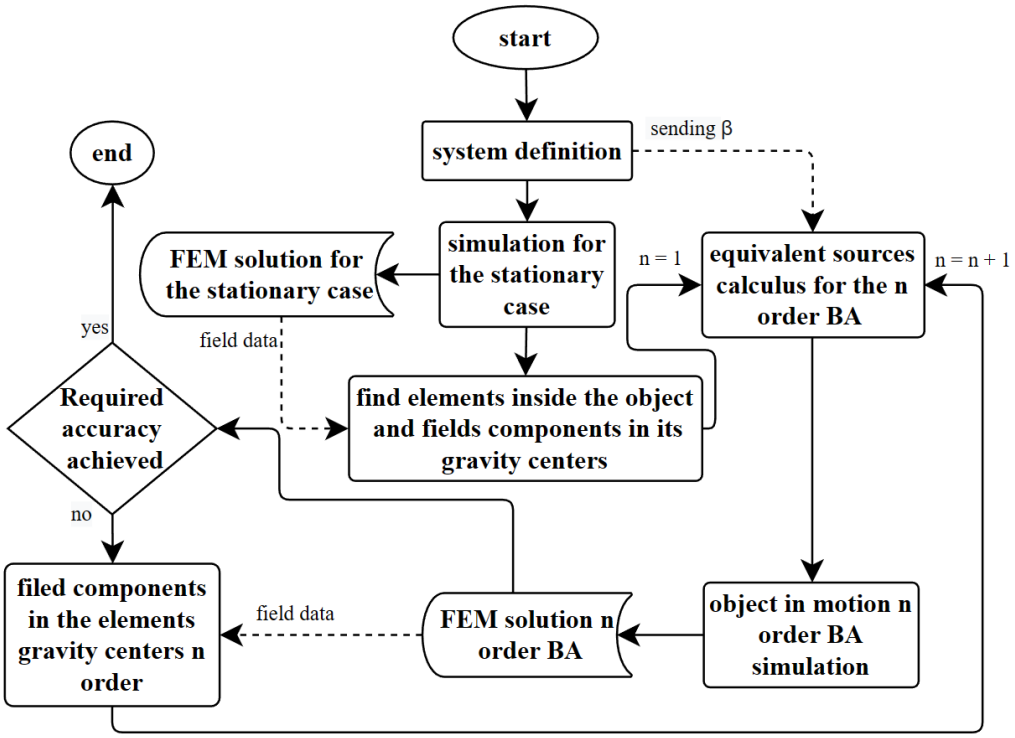

Figure 2.2: General diagram of the implementation of the new BA methodology in the FE solver.

be noted that the uniformity of the β is not a requirement for the methodology. Then the second run of the finite element solver occurs, in which the original scatterer is replaced, according to the Born approximation, by equivalent sources (see (2.3)). If the solution for the current value of n satisfies the required accuracy, then the procedure ends. Otherwise, based on the results of the last calculation, the equivalent currents are calculated again. The procedure is repeated, *mutatis mutandis*.

A number of important clarifications need to be provided for the presented procedure. First, this workflow can be applied to scattering problems of any dimensionality. Within the scope of this work, we obtained reliable results for both 2D and 3D cases, which are presented in Chapter 4. It should be noted that, within the framework of this procedure, the FEM mesh is of particular importance not only in the classical sense [34, 59], but also because it plays a crucial role in defining the equivalent sources. According to (2.5), in order to obtain the equivalent sources, it is necessary to use the values of the $\mathbf{E}_0$ and $\mathbf{H}_0$ at specific coordinates within Ω_s (since only there the sources are nonzero, see Figure 2.1). An important question arises: how should the coordinates at which the fields

values are to be determined be selected? From the perspective of the FE approximation, the most reliable approach is to compute the fields at the element centroids, which is the method we employ. However, in this case, the accuracy of the results is highly sensitive to the quality of the computational mesh. This issue becomes particularly critical when integrating the methodology into commercial CAD software, as discussed in Chapter 3. In this case, the number of elements in the mesh for Ω_s should be chosen not only based on standard considerations related to the wavelength within the scatterer, but also to ensure the subsequent accuracy in representing the distribution of equivalent current densities within the subregion.

The settings of the matrix solver also play a significant role. FE solutions are typically obtained using iterative solvers. Since our focus is on computing small quantities, the choice of stopping criterion and related parameters becomes particularly critical. In the present study, the iterative process is terminated once the prescribed residual threshold $\delta = 10^{-m}$ is reached. The range of variation of the quantity is as follows: $m \in [8 \div 12]$. These values slightly extend the range commonly used in double-precision computations to provide clearer insights into the influence of this parameter. If we define the relative velocity as $\beta = 10^{-b}$, then, for a reliable determination of the motion effects at this velocity, the following condition must be satisfied: $m \geq b$.

2.4 Key Properties of the New BA Methodology

In this section, we outline the general properties of the proposed methodology that are essential for the subsequent analysis.

2.4.1 Complexity of the BA Methodology

To obtain the motion effects using the traditional difference method, it is necessary to solve two problems (2.2) and (2.1), with respect to, for example, $\mathbf{E}$ and $\mathbf{E}_0$. Thus, the algorithmic complexity of traditional methods is the sum of the algorithmic complexities of solving these problems. Since neither of these problems provides a direct solution for the target quantity, $\mathbf{D}_a$ is computed *a posteriori* as the trivial difference between the solutions of the first and second problems. Thus, within the procedure of the traditional difference method, the necessary and sufficient number of problem solutions is two. Nevertheless, as clearly demonstrated in Section 2.2, the complexity of these problems is not the same. Solving one of them is significantly more resource-demanding than the other. This, however,

holds true only if the problems within the traditional difference procedure are solved in the manner presented here. As noted in Section 1.5, this is by no means mandatory. Nevertheless, we assume this approach within the traditional difference procedure, since it allows a qualitative assessment of the algorithmic complexity of the new methodology in comparison with it.

While the solution of problem (2.2) can be regarded as straightforward, the variational formulation of problem (2.1) is considerably more complex (see (2.9) and (2.10)). According to the derivation presented in Section 2.1, to obtain an exact solution for the motion effects, it is sufficient to solve only a single problem (2.3). Nevertheless, obtaining an exact solution in a single-step procedure is not possible. According to the diagram shown in Figure 2.2, the first step is solving problem (2.2). In other words, this is the same problem that is solved within the traditional difference method. Thus, the algorithmic complexity of the first step in both approaches is equivalent. The second step, which implements the first-order BA, involves solving problem (2.3) with the sources obtained from equation (2.5). We have already noted that solving this problem is algorithmically less demanding than solving the second problem in the traditional difference method. However, the procedure does not necessarily terminate at this stage and may proceed into a loop implementing the second-order BA. In this case, problem (2.3) is solved in the same manner, but using the refined sources from (2.5). Without specifying a breaking criterion for this loop, the procedure may initiate the implementation of higher-order BAs. Before addressing this issue, we present some interim conclusions. The algorithmic complexity of the new methodology for the first-order approximation is lower than that of the traditional difference method. For the second-order approximation, it is slightly higher. It is evident that at each new iteration of the Born approximation, the algorithmic complexity increases. If the absolute computation time for a single iteration of the approximation loop is denoted by t_i , then the time for the n-th order approximation is simply $n \times t_i$. It should also be noted that this requires solving $(n + 1)$ problems.

In diagram 2.2, there is a decision block labeled “Required accuracy achieved.” How can one answer the question “Has the desired accuracy been achieved?” without any *a priori* knowledge of the system? As shown by empirical studies of the method, described in detail in Chapter 4, there is no practical need to consider orders higher than the second. All information regarding motion effects can be obtained at $n = 2$. Thus, without any additional knowledge about the system, the approximation process should terminate at $n = 2$, whereas the decision block present in the diagram 2.2 acts as a Boolean element asking, “Is the first-order BA sufficient in current case?”

2.4.2 Limits of Applicability of the BA Methodology

The new BAs methodology largely inherits the limitations and conditions of the classical approach described in Section 1.4. There is a direct analogy between (1.12) and (2.4). Let us decompose the differential electric field into its components (a similar representation applies to the magnetic field)

$$\mathbf{D}_e = \mathbf{E} - \mathbf{E}_0 = \mathbf{E}^{inc} + \mathbf{E}^{sc} - \mathbf{E}^{inc} - \mathbf{E}^{sc,0} = \mathbf{E}^{sc,0} + \mathbf{E}^{mov} - \mathbf{E}^{sc,0} = \mathbf{E}^{mov}. \tag{2.13}$$

In the sequence of trivial expressions (2.13), it is taken into account that the field scattered by a moving media can be represented as a superposition of the field scattered by the media at rest and the additional scattering component associated with the motion effect $\mathbf{E}^{mov}$. The total fields can be represented as: $\mathbf{E} = \mathbf{E}^{inc} + \mathbf{E}^{sc,0} + \mathbf{E}^{mov}$. Thus, the only condition that allows us to transition from the exact formulation (2.4) to the approximate one (2.5) is: $\mathbf{E}^{mov} \to 0$. This leads us to two important conclusions that define the limits of applicability of the proposed methodology:

> Provided that the moving media induces only small-magnitude motion effects, its constitutive parameters at rest can be any. In other words, the scatterer at rest does not necessarily have to be weak for the proposed methodology to be effectively applied to the analysis of its motion effects. In the deeply non-relativistic regime, motion effects are inherently weak.
>
> Referring back to expression (2.13), it is evident that the equivalent condition for the approximation is: $\mathbf{D}_a \to 0$. It follows that the lower the velocity of the media, the more accurate the approximation, and consequently, the more precisely problem (2.3) is solved. This unique feature of the methodology is likely its most significant advantage over traditional difference methods, where the opposite behavior is observed as β decreases. At relativistic velocities, for which the traditional difference methods provide reliable results, the error of the BAs may be higher. However, it should be noted that if the motion effect is small in magnitude, even at relativistic velocities (for example, in almost radio-transparent media), the methodology can still be applied effectively.

It should also be noted that the proposed methodology avoids direct subtraction by extracting the effect directly from the state of the moving media. In this way, the procedure circumvents the amplification of numerical errors inherent in subtractive methods. This

direct estimation significantly improves robustness against floating-point limitations and reduces sensitivity to noise (see Section 1.5).

From a formal perspective, the solutions of equations (2.3) represent certain part of fields scattered by a stationary bianisotropic object. In fact, this defines the equivalent transition from a moving isotropic dielectric to a stationary bianisotropic one. If the subregion Ω_s is associated with a non-inertial reference frame, such a transition occurs non-instantaneously [60]. In this case, if the reference frame L' (see Section 1.3) is non-inertial, the Born approximation can only be applied within the rest frame theory [61, sec. II]. This is particularly important when considering rotating axisymmetric bodies.

Several significant similarities can be identified between the proposed method and that described in [62]. In that work, the authors present a method for analyzing the bianisotropic effects of a material at rest. Similarly, in the current-based approach, the sources are expressed in terms of the material parameters, and their radiation is computed using integral equations. The present work proposes an alternative approach for computing the electric and magnetic currents considered in [62, eqs. (12), (13)], thereby extending the applicability of the BAs methodology to the analysis of weak bianisotropic effects in artificial materials at rest.

2.4.3 Fake Born Approximation

A distinctive feature of the procedure shown in Figure 2.2 is its flexibility and adaptability. One possible implication of this is the replacement of the numerical solution step for the state 0 with an analytical one, if such a solution exists. Similar to traditional difference methods, where the solutions for both states can be obtained in various ways (see Section 1.5), the BAs methodology also allows for combining different approaches. Thus, if the solution for the stationary medium is obtained analytically, we refer to this approach as the *Fake Born Approximation*. The problems for which such an approach is possible have already been described in Section 1.5. Below, we highlight two important features of the fake BA.

> If we assume that the analytical solution for the media at rest is the most accurate available and use it instead of a numerical approach, we reduce the computational error. This approach is useful for assessing solution accuracy and for extrapolating it to more complex cases that do not have an analytical solution. We use the fake BA to verify certain results presented in Chapter 4.

A remarkable property of the fake BA is that it is the most accurate and simple among the considered approaches for calculating the effects of slow media motion. As noted above, it is more accurate than the general BAs methodology as well as more precise than traditional difference methods for the reasons described in Subsection 2.4.2.

It should be noted that if an analytical solution exists also for state 1, it can be used to determine the total fields in the system and be directly substituted into (2.4), avoiding the BAs. In this way, the motion effect can be obtained without use of the traditional difference method as well.

The greatest benefit of the flexibility of the proposed algorithm can be achieved by integrating it into a commercial CAD software. One possible implementation of such an integration is described in the following chapter.

CHAPTER 3

Application of the BA in COMSOL Multiphysics

Working with our native codes provides certain benefits, such as the ability to easily introduce modifications of interest for specific applications. However, these codes lack many of the advanced functionalities available in commercial simulators. Commercial software, in contrast, offers a broad spectrum of capabilities, including professional meshing and post-processing, multiphysics and multiscale modeling, parametric optimization, and even neural network–assisted design tools. For this reason, integrating an effective methodology into a commercial solver yields a synergistic outcome: it combines the flexibility of our approach with the robustness of established platforms, thereby simplifying its use, ensuring broad accessibility, and eliminating the need for specialized external libraries.

The main requirement for successfully implementing the procedure shown in Figure 2.2 is the ability to work with imported sources within commercial CAD software. External sources described by an electric current density distribution can be imported and assigned to the corresponding model region in all commercial CAD software known to the author, as this capability is standard in electromagnetic modeling. In contrast, sources described by magnetic current density distributions are not universally supported. To preserve the usability of the procedure and ensure practical simplicity, it is preferable that such tools be available directly within the graphical user interfaces of commercial CAD software, without relying on unofficial plugins, auxiliary tools, or complex application programming interface manipulations.

One possible solution that supports the handling of magnetic current sources is the COMSOL Time Explicit EMW module [64]. This interface provides the solution of electromagnetic problems in the TD. Since our problem is formulated to be solved in the FD, several steps of the TD solution are redundant. We optimize this process, and to convert

The material of this chapter is based on the publication [63] and it was presented and discussed at a conference URSI International Symposium on Electromagnetic Theory, which was held in Bologna, Italy (2025).

the solution from the TD to the FD, we use the classical Fast Fourier Transform (FFT). However, we must comply with the requirements of the TD simulation and formulate an equivalent problem that accounts for the specifics of the selected COMSOL module. All the required formulations are provided in Section 3.2. A key aspect of successfully integrating the BAs methodology into commercial CAD software is the interpolation of sources within the model. Several important details of this process, illustrated using COMSOL, are provided in Section 3.3. It should be noted that this material is general to the methodology, is not tied to any specific module in which it is implemented, and can be applied within other possible approaches. Finally, Section 3.4 provides some confirmations of the effective use of the methodology within commercial CAD software, describes potential scenarios for its application, and highlights the prospects for following research.

3.1 BA in COMSOL Time Explicit EMW Module

Figure 3.1 shows a diagram of the main processes for applying the methodology in COMSOL Time Explicit EMW interface. This block diagram complements the overall algorithm shown in the Figure 2.2. We retain the existing method for calculating equivalent currents but provide additional processing to ensure data format compliance. The "System Geometry" block indicates that the geometry of the problem is identical both for determining the equivalent sources (performed in the native solver) and for their interpolation in COMSOL.

In the TD, the harmonic current sources oscillations are written as follows:

$$\begin{aligned}\mathbf{J}(x,y,z) = &\left|J_x(x,y,z)\right| \times \cos\left(\omega t + \arg\left[J_x(x,y,z)\right]\right)\hat{x} + \\ &\left|J_y(x,y,z)\right| \times \cos\left(\omega t + \arg\left[J_y(x,y,z)\right]\right)\hat{y} + \\ &\left|J_z(x,y,z)\right| \times \cos\left(\omega t + \arg\left[J_z(x,y,z)\right]\right)\hat{z}.\end{aligned} \tag{3.1}$$

In this form, the electric and magnetic sources (2.5) of the BA methodology should be presented. A table-defined function is created to describe expression (3.1), which establishes the standard intrinsic COMSOL interpolation procedure. The first columns contain the coordinates of the points (x, y, and/or z), while the subsequent column contains the phase or magnitude values of the corresponding current density component. According to (3.1), a total of 12 files are loaded into COMSOL in the general case (6 for electric currents and 6 for magnetic currents). Once the data is loaded into COMSOL, the internal

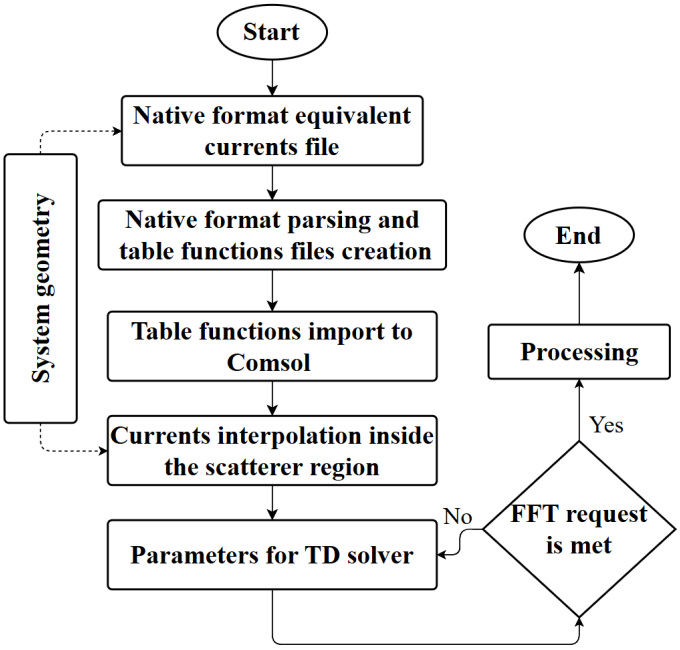

Figure 3.1: Workflow diagram for applying the methodology with COMSOL Multiphysics.

interpolation algorithm can be any method (nearest neighbor or linear). The quality of interpolation, where the current within a single element is constant (nearest neighbor), depends solely on the loaded files. Extrapolation should adhere to a predetermined rule: it must take a value strictly equal to zero outside the defined domain of the currents.

3.2 Time Domain Transition

The problem is initially formulated in TD, after which the classical FFT is applied to obtain the desired result in the frequency domain. We begin by introducing three key time values and the fundamental relationship between them as follows:

$$\begin{aligned} T &= \frac{1}{f}, \\ T_t &= \frac{s}{v_p}, \\ T &< T_t < T_{obs}, \end{aligned} \tag{3.2}$$

where T is the period of the oscillations of interest, T_t is the travel time for the wave to propagate from the source to the boundary of the numerical domain (at which the observation point is located), and T_{obs} is the observation time. Thus, s is the maximum

distance between the region where the equivalent sources are defined and the observer, v_p is the phase velocity of the wave. Inequality in (3.2) means that during the observation of the periodic process, the wave from the source must reach the observer while completing several full oscillation periods. Otherwise, there will not be enough information to restore the characteristics of the process of interest.

In addition to the time condition, it is necessary to satisfy the sampling frequency condition according to the Nyquist–Shannon theorem, namely: $f_s > 2f$. If the analysis time interval of the system in the TD solver is chosen as $[0 \div T_{obs}]$, with the time step $d_t = \frac{T_{obs}}{n_s}$, then $f_s = \frac{1}{d_t}$. Here, n_s is the total number of time samples of the system state during the observation period [64]. By analogy, we introduce frequency discretization as $d_f = \frac{f}{n_f}$, where n_f is the total number of frequency points in the resulting spectrum. The observation time can also be expressed through this quantity as $T_{obs} = \frac{1}{d_f}$.

For simplicity, we will choose the quantitative parameters n_f and n_s as the input variables of the solver. From (3.2) and the sampling frequency condition, it follows that these parameters are related by a simple inequality:

$$1 < n_f < \frac{n_s}{2}. \tag{3.3}$$

The physical meaning of the introduced quantities is standard when observing a periodic process for a limited period of time. An important measure of the accuracy of the TD solution is the number of samples of the oscillatory process state taken during one period. This quantity can be easily obtained as $n_{rep} = \frac{n_s}{n_f}$, which makes it possible to control its value at the solver input. We apply continuous Fourier transformation scaling over the time interval, with f being the maximum frequency for the analysis. Since we control the value of n_f, we can always set it as an integer. This ensures that the frequency of interest is always included in the resulting spectrum.

3.3 Currents Interpolation in COMSOL

Source data are imported into COMSOL in the form of tabular coordinate functions. For the first-order BA, we obtain complex values for the sources from expression (2.5), then compute the magnitude and phase of the complex numbers and load them as external files into COMSOL. These functions are then interpolated over the region where the currents are defined by (3.1) (see Figure 2.1).

We tested multiple approaches to interpolate these functions in COMSOL. The highest simulation accuracy was achieved when interpolation was performed after the FE mesh was deduced for the geometry of interest, with the current distribution defined as a piecewise-constant function within each element. All information regarding the interpolation of tabulated functions in COMSOL can be found in [65, p. 363]. The FEM mesh-based interpolation, which was found to be the most effective in this study, is detailed in [66]. General information on interpolation in computational electrodynamics applications, along with error estimation, is provided in [67]. Here we describe the most general and reliable approach we used for interpolating three-dimensional tabular functions. This method allows controlling the accuracy associated with the interpolation procedure and the representation of equivalent sources.

There are two discretization parameters to consider: discretization of the current distribution and discretization of the parametric geometry region of sources. Recall that the first process is related to determining the equivalent sources inside the scatterer, according to diagram 2.2. We provided a brief description of this process in Section 2.3. The second process is the discretization of the model geometry into a computational mesh, which is necessary for its numerical analysis in COMSOL (in the native solver, there is no parametric geometry specification, and the model is defined directly using polygons). Many possible relationships exist between these discretizations, but the most common are shown in Fig. 3.2. For simplicity and clarity, we present the relationships between triangular elements, although everything stated also applies to tetrahedra in the mesh.

The first case involves complete mesh matching. A computational mesh is initially created over the geometry, and the current distribution at the centers of gravity of the elements is determined and imported into external software. Calculations are then performed on the same mesh with the sources included, allowing full control over discretization accuracy and preventing element overlaps. The second case arises when the discretization of the current distribution is significantly coarser than that of the geometry. While this approach reduces the size of current tables and accelerates the interpolation process, it increases the likelihood of element intersections, complicating the estimation of accuracy.

In the third case, the discretization of the current distribution is finer than that of the geometry. This scenario offers two sub-options. Either the current value near the center of gravity of the solver's element is extrapolated across the entire element (as shown in Fig. 3.2), or multiple current values exist within one element, meaning the function is no longer piecewise constant within its boundary.

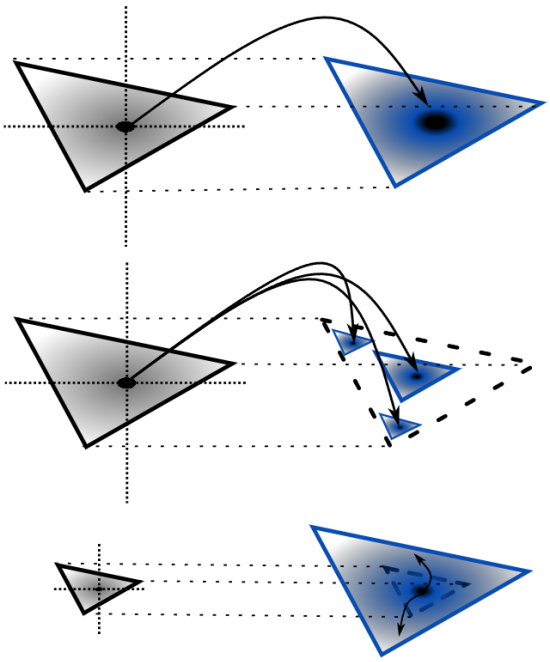

Figure 3.2: Some of the possible relationships between the elements used to calculate the equivalent current densities and the mesh elements used by the solver to compute the Born approximations. The figure shows for simplicity the correspondence between triangular elements. However, the relationships shown are representative of what also happens for discretizations of three-dimensional domains.

Thus, the most reliable approach is to use identical discretization at both of the specified stages. Initially, we generate the computational mesh in COMSOL according to standard rules of electrodynamic modeling. We then export this mesh to the native solver, where the coordinates of the centroids of the elements belonging to the Ω_s are determined, and the values of the equivalent sources within them are calculated. Next, we create files of tabulated functions, load them into COMSOL, and interpolate the functions within the scatterer. The model calculation in COMSOL is performed on the originally generated mesh. Consequently, changing the mesh quality and the number of elements has a controlled and predictable effect both on the accuracy of the electrodynamic calculation and on the quality of the description of the current density distribution within the subregion of interest. An important step in organizing this process is the creation of a mesh converter, which allows transferring the mesh geometry created in COMSOL to the native solver (this process is described in the Appendix A).

As an illustrative example, Figure 3.3 shows the interpolated equivalent sources in COMSOL. The figure shows some Cartesian components of the electric current of the

equivalent sources for the problem of electromagnetic wave scattering from a circular infinite cylinder moving along its axis of symmetry. The problem is solved in 2.5D (see [38, 39, 55]), so in this case a two-dimensional tabulated function is interpolated. The sources shown were used to verify the algorithm for implementing the BA methodology in COMSOL. Accordingly, all model parameters and the results of its calculation are provided in corresponding part of Chapter 4.

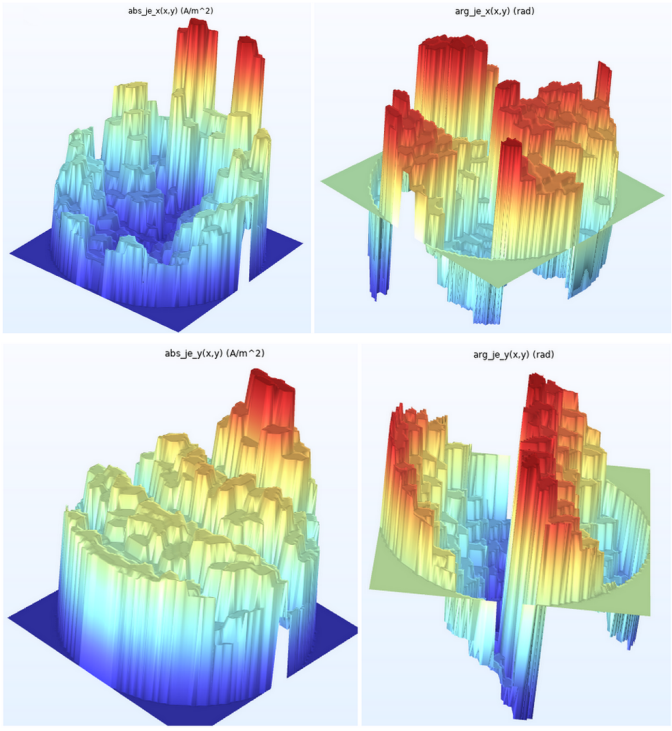

Figure 3.3: Example of interpolation of some components of the electrical equivalent current densities in COMSOL. Top left for $|J_x(x, y)|$, top right for arg $[J_x(x, y)]$, bottom left for $\left|J_y(x, y)\right|$ and bottom right for arg $[J_x(x, y)]$.

The radiation of electric and magnetic sources, as one of the possible results of the corresponding model calculation in COMSOL, is shown in Figures 3.4 and 3.5. These results were obtained for the interpolation shown in Figure 3.3 (not all interpolated functions are presented). The two-dimensional geometry of the system fully corresponds to that shown in Figure 2.1. In this case, the subregion Ω_s is a disk. This is only an illustrative example; the specific calculation parameters are provided in Chapter 4.

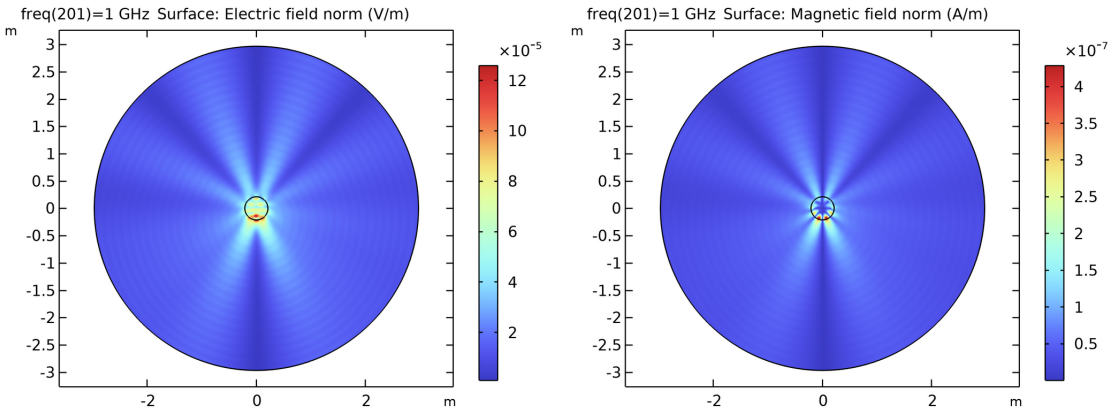

Figure 3.4: Visualization of the radiation of equivalent electric and magnetic currents obtained in COMSOL Time Explicit EMW Module.

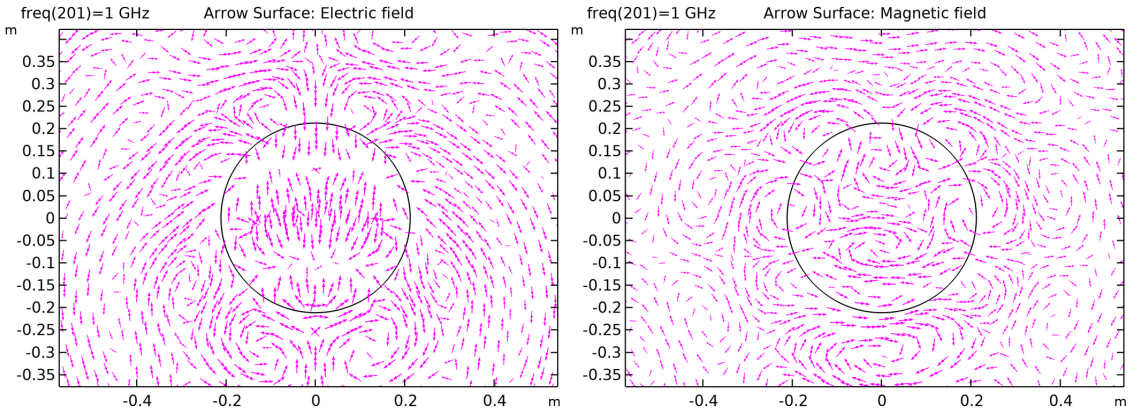

Figure 3.5: Visualization of the tangential components of the vector fields of radiation from electric and magnetic equivalent sources obtained in COMSOL Time Explicit EMW Module. Identical behavior for any values of β.

3.4 Prospects and Potential

As noted above, the application of the new methodology within a commercial CAD system opens up new possibilities for solving electrodynamic problems, the efficient solution of which was previously unavailable. Below is a list of potential scenarios for applying the BA methodology in COMSOL, which have significant practical and scientific relevance.

1. Parametric optimization of the model geometry for designing sensors of media motion effects.

   A parametric optimizer that enables searching using modern methods is a powerful tool in contemporary CAD systems [68]. With the help of this tool, the optimal

state of the system can be found, for example, a configuration that ensures the most reliable detection of a low-magnitude effect. Optimization can also be used to study the model's stability and sensitivity to small variations of the parameters. Parametric optimization can play a crucial role in designing sensors for weak bianisotropy, for example, in the development of new types of electromagnetic flowmeters. This topic is discussed in Chapter 5.

2. Use of real sources in the model.

All analytical solutions of the problems considered in Section 1.5 use a source of incident waves located infinitely far from the scatterer, producing plane electromagnetic waves. A commercial CAD system allows modeling in the presence of a real source, such as a specific type of antenna. This greatly enhances the practical significance of the developed methodology.

3. Solving inverse problems and tasks related to reconstructing velocity profiles.

The necessity of this process was already emphasized in the introduction to the work as well as in Section 1.6.

4. Conducting the complete procedure for designing an optimal experiment and obtaining reliable expectations for its results.

The importance of this process was highlighted in [69]. A well-designed laboratory experiment is a key step in verification, and at present, this stage poses the greatest challenges. Chapter 5 provides a description of the experiments conducted to detect media motion effects. However, the results of these experiments do not have a clear interpretation, as they were carried out without modeling-supported expectations for the target outcomes.

5. Conducting multiphysics and multiscale numerical studies.

In Section 1.2, we also noted that a comprehensive study of motion effects should be multiphysical [15] and multiscale [16]. COMSOL Multiphysics software is ideally suited for such studies [65]. In addition to the cases mentioned, there are other potential scenarios. For example, accounting for thermodynamic effects occurring in a liquid or gas flow in pipes proves to be a very important element in the development of Fizeau-Fresnel flowmeters at microwaves [3]. In non-inertial reference frames, it is important to account for effects at different scales, including meso-scale effects

(effects related to a group of elementary particles, such as electrons or atoms) [70, 71].

Work [72] describes the motion of electrons in a rarefied gas under the action of centrifugal forces in a rotating reference frame. The resulting microcurrents are modeled with COMSOL simulator. The work explains that as long as these currents exist, the scatterer cannot be considered a static bianisotropic object, since it is in a transitional state. The analysis of electromagnetic scattering on such a body must also account for effects at different scales and in TD.

6. Conducting high-performance computations of complex models.

A number of the applications mentioned above can be implemented within the native solver. However, as noted in Chapter 1, unoptimized code and the lack of computational acceleration capabilities make the analysis of resource-intensive problems unacceptably time-consuming. Commercial CAD systems, in their standard packages, offer cloud, distributed, and parallel computing capabilities with an optimized solver code. It should be noted that the applications mentioned above represent complex computational problems, and in this context, high-performance computing is not merely an option but a necessity.

At the end of the chapter, it should be noted that an algorithm for implementing the methodology in COMSOL is currently being developed in another CAD module, without the need to formulate the problem for the TD solver, which is unnecessary for the class of problems under consideration. Nevertheless, the approach described in this chapter can prove highly effective for problems where it is necessary to analyze weak bianisotropy effects of moving media, in the presence of time-dependent motion effects, such as modulation of the scattered signal. A striking example of such problems is the rotation of a non-axisymmetric body or non-stationary rotation (rotation with angular acceleration, rotation with precession, *etc.*). This future research direction is discussed in Chapter 6.

CHAPTER 4

Verification and Simulation Results

4.1 Verification Approach and Problem under Consideration

To verify the BA methodology and its implementation in COMSOL, a problem with an exact analytical solution [38, 39] is used. TM-polarized electromagnetic plane wave with frequency f traveling along y axis is scattered by a circular homogeneous cylinder, with the axis of symmetry along the z axis and radius a. The vector of its linear velocity $\mathbf{v}$ is directed along the same axis. With the considered motion the scatterer boundary is stationary. The material of the cylinder at rest has the following parameters: $\mu = \mu_0$, $\sigma = 0$ with a variable value of ϵ_r. The geometry of the problem is shown in Figure 4.1.

The analytical solution of the problem is obtained for an infinitely long cylinder. In this case, the problem is reduced to a two-dimensional one. We refer to this solution as 2.5D because the obtained result is equivalent to a three-dimensional one under the condition of an infinitely long scatterer. By assuming the cylinder to be sufficiently long compared to the wavelength of the source, or by applying absorbing boundary conditions to the ends of the cylinder, we can consider scattering only from a finite section of the infinite cylinder, thereby solving a fully three-dimensional problem. Additionally, periodic boundary conditions may be used [47, 74], in this case. However, to verify the algorithm, we kept the BCs without changes.

Let us present some general properties that are important for performing verification. The relative velocity β and its powers determine the magnitude of the effect of motion.

The material in this chapter is based on results presented in various publications on the subject. Section 4.2 compiles a mix of results published in [55] and [73]. The results were presented at the IEEE International Symposium on Antennas and Propagation and INC/USNC-URSI Radio Science Meeting, held in Firenze, Italy (2024). The content of Section 4.2.3 was presented at the XXV Riunione Nazionale di Elettromagnetismo held in Viareggio, Italy (2024). The results presented in Section 4.3 were published in [63] and reported at the URSI International Symposium on Electromagnetic Theory, which was held in Bologna, Italy (2025).

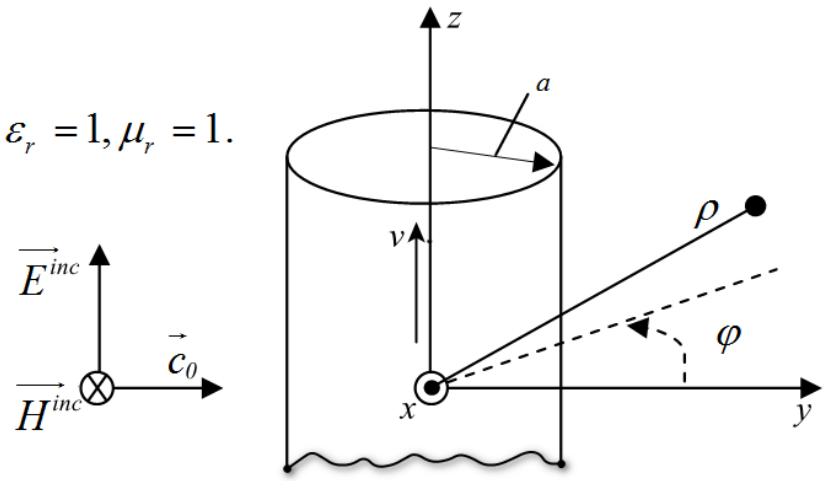

Figure 4.1: Geometry of the problem for a cylinder moving along its axis of symmetry.

This effect occur at two different orders of magnitude. The components of the electric field that are perpendicular to the velocity vector **v** are first-order effects, controlled by β^1. The component of the electric field aligned with **v** is a second-order effect, controlled by β^2. In the problem under analysis, the field components affected by different orders of the effect are easily separable and can be analyzed independently (this is due to the symmetry and simplicity of the geometry).

For cylinders at rest composed of isotropic materials, a transverse electric (or magnetic) current density produces a solution with a trivial TM (or TE) component and a non-trivial TE (or TM) component [51, 55]. This consideration implies that, under TM illumination, the solution of problem (2.3) for $\mathbf{E}_0$ and $\mathbf{H}_0$ contains only the TM component, that is

$$E_{0,x} = E_{0,y} = H_{0,z} = 0. \tag{4.1}$$

The remaining field components, in general, are nonzero. It should also be noted that when considering a moving cylinder, the condition (4.1) no longer holds [51].

For clarity, the parameters used in the verification process are summarized in Table 4.1. Parameters not listed in the table are variables that change during the verification process, and their values are provided in the descriptions for each corresponding result.

In Section 4.2, we present the verification of the methodology described in Chapter 2 using the native solver for both two-dimensional and three-dimensional cases. The accuracy problems of traditional difference methods, even when using analytical solutions (described in Section 1.5), are clearly demonstrated in Section 4.2.3. In Section 4.3,

Table 4.1: System parameters for the verification.

Parameter	Value	Problem
f	1 GHz	All
ϵ_r for Ω	1	All
μ_r for Ω	1	All
μ_r for Ω_s	1	All
σ for Ω	0	All
σ for Ω_s	0	All
R	2.967793920005365 m	2.5D
a	0.2119852800003832 m	2.5D
R	0.6 m	3D
a	0.2 m	3D

we present the results of verifying the adaptation of the methodology in COMSOL, the algorithm of which is described in Chapter 3.

4.2 General Verification of the BA Methodology

To obtain the BA results presented in this section, the native solver and the procedure shown in Figure 2.2 are used. All FE solutions were computed using a first-order Lagrangian approximation for the axial component of the unknown field and a first-order edge element approximation for its transverse part [58, 75]. Almost uniform meshes with p concentric circles were employed. An example obtained for $p = 20$ is shown in Figure 4.2 (left-hand side). The number p was always chosen so that the meshes contained approximately 14 elements per wavelength. This value was slightly higher than the usual one, which is 10 for first-order finite element approximations. This choice was made to limit errors due to finite element discretization and to facilitate the analysis of first- and second-order BAs.

For three-dimensional problems, a mesh of tetrahedra is used. A number of layers q is chosen on the cylinder, between which prisms are formed, with triangular bases corresponding to the two-dimensional elements shown in Figure 4.2 on the left. These prisms are then divided into three tetrahedra of equal volume, following standard procedures. An example obtained for $p = 6$ and $q = 6$ is shown in Figure 4.2 (right-hand side). The use of a 3D native solver for analyzing problems similar to ours is described in [76].

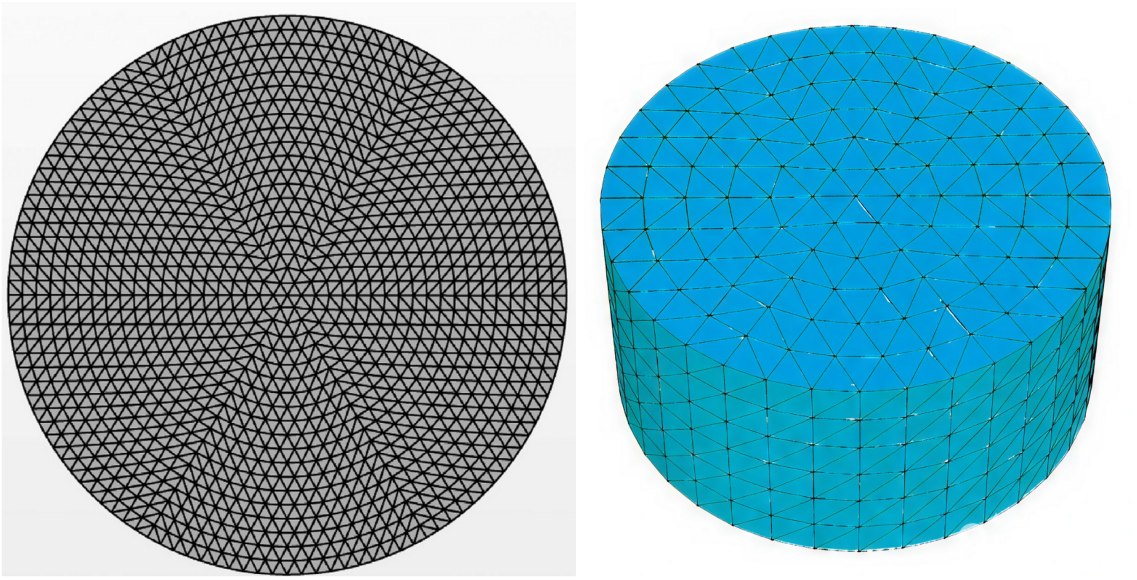

Figure 4.2: An example of the quasi-uniform meshes used in native solver. On the left – the triangular mesh on the two-dimensional geometry for $p = 20$. On the right – the tetrahedral mesh on the three-dimensional geometry for $p = 6$ and $q = 6$.

4.2.1 Two-dimensional Problem

For all results presented in this subsection, the following input parameter values apply: $a = \frac{\lambda_0}{\sqrt{2}}$, where λ_0 is the wavelength in free space (the scatterer is surrounded by free space). The numerical analysis domain Ω (see Figure 2.1) is a disk with a radius of $R = 14a$.

Figure 4.3 shows a comparison of results of first- and second-order BAs for the magnitude of z field component $\mathbf{D}_e$, along with two results obtained using traditional difference methods. The first traditional method is the difference between the states obtained from the semi-analytical solution [39], while the second is the difference between the states obtained using the native FE solver [77]. The result obtained from the difference of the semi-analytical solutions is well approximated by the second-order BA and FE traditional difference, although the latter exhibits spurious oscillations in regions where the motion effects are weaker. In contrast, first-order BA shows errors of the same order of magnitude as the quantity it is intended to approximate.

In most applications, users of finite element simulators generally do not need to adjust the parameters of the algebraic solvers. However, the inability to control parameters such as δ can have serious consequences for the reliability of the calculations considered in this work. To illustrate this, we repeated our analysis with $\delta = 10^{-8}$. This modification does not affect the semi-analytical solutions, but it has a significant impact on all finite element

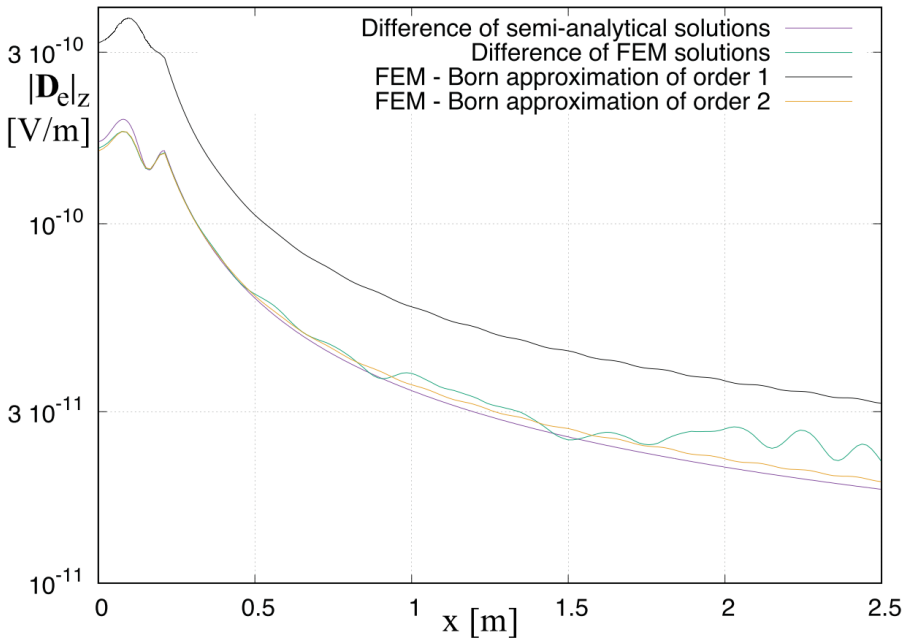

Figure 4.3: Approximations for $|\mathbf{D}_e|_z$ along the x axis for $\beta = 10^{-5}$, $\delta = 10^{-12}$, $p = 196$ and $\epsilon_r = 2$.

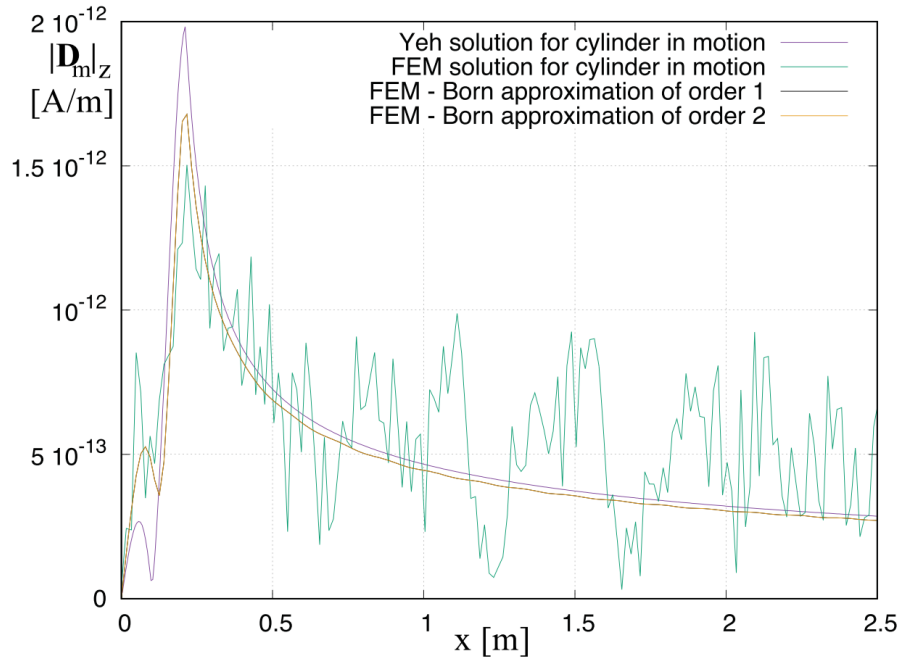

Figure 4.4: Approximations for $|\mathbf{D}_m|_z$ along the x axis for $\beta = 10^{-9}$, $\delta = 10^{-8}$, $p = 196$ and $\epsilon_r = 2$.

results. One possible solution is to use direct methods for solving matrix equations instead of iterative ones. However, even with commercial CAD systems, this resource-intensive approach becomes impractical for solving problems of any significant complexity.

Figure 4.4 illustrates, for example, the motion effects on the axial component of the magnetic field along the x-axis when $\beta = 10^{-9}$. The figure shows that the first- and second-order BAs produce very good results, with negligible differences between them, whereas the FE difference is incorrect. Interestingly, for cylinders moving along their axis and illuminated by a TM-polarized wave, such errors are less severe than those found in the electric field when the reliability conditions are not met. This is because, for the magnetic field, no difference computation is required, since $H_{0,z} = 0$ (see (4.1)). Thus, the analytical difference provides the most accurate result.

Figure 4.5 shows the motion effects on the axial component of the electric field along the y-axis for $\beta = 10^{-4}$. It is important that the errors affecting FE solutions in Figure 4.5 are significantly greater than those in Figure 4.3 for the same component, even though the velocity is ten times higher, which should yield better results. This discrepancy arises solely from the different δ values used in the two simulations. As noted earlier, for an effect controlled by the β^2 , the first-order BA introduces an error of the same magnitude as the effect itself, whereas the second-order BA provides a good approximation to the semi-analytical solution.

Figure 4.6 illustrates the behavior of $|\mathbf{D}_m|_z = |H_z|$ along the x-axis for $\beta = 10^{-7}$ and $\delta = 10^{-8}$. In this case, we consider a sufficiently radio-transparent scatterer with $\epsilon_r = 1.01$. According to the explanation provided in Section 1.3 the dielectric parameters of the media in motion have important consequences on the motion effects. Such a value could be of interest when the medium in motion is, for example, a gas [38]. The low density of the scatterer poses a major challenge for the FE traditional difference approach, despite the relatively high velocity considered (about 30 m/s) and the significant first-order motion effect on this component. This unreliability is similar to that observed in Figure 4.4 for the same component and arises because the quantity of interest is of the same order of magnitude. The influence of the higher velocity is counterbalanced by the much smaller value of ϵ_r. In contrast, first and second orders of BAs closely approximate the semi-analytical solution.

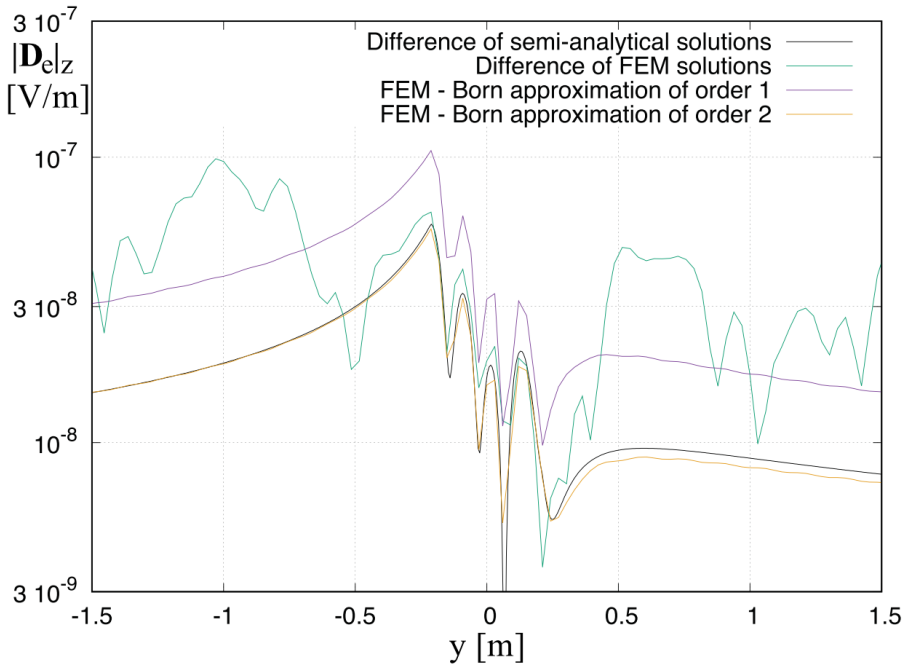

Figure 4.5: Approximations for $|\mathbf{D}_e|_z$ along the y axis for $\beta = 10^{-4}$, $\delta = 10^{-8}$, $p = 196$ and $\epsilon_r = 2$.

4.2.2 Three-dimensional Problem

In this section, we present the results of the verification for the three-dimensional electromagnetic scattering problem. The formulation corresponds to that described in Section 4.1, however, in this case, we consider a cylinder of finite length l. The center of the cylinder along the axis of symmetry is located at the origin. Thus, the coordinate z changes within $[-\frac{l}{2}, \frac{l}{2}]$. The main challenge of this formulation has already been mentioned in Section 4.1.

Since the upper and lower boundaries of the scatterer (the bases of the finite-length cylinder) are now located within the numerical analysis domain Ω, the last of equations (2.3) no longer holds, which compromises the strictness of the methodology. To minimize this effect, the boundaries of the scatterer must be placed sufficiently far from the boundary $\partial\Omega$, which in this case is a spherical surface of radius R. A significant error is expected when computing the difference fields along the z-axis, especially in the regions near the cylinder boundaries.

To assess and minimize this error, we carried out verification in three stages. Firstly, we validate our solver with analytical solution for the stationary infinite circular cylinder. Secondly, we implement the 3D classical Born approximation for the electromagnetic

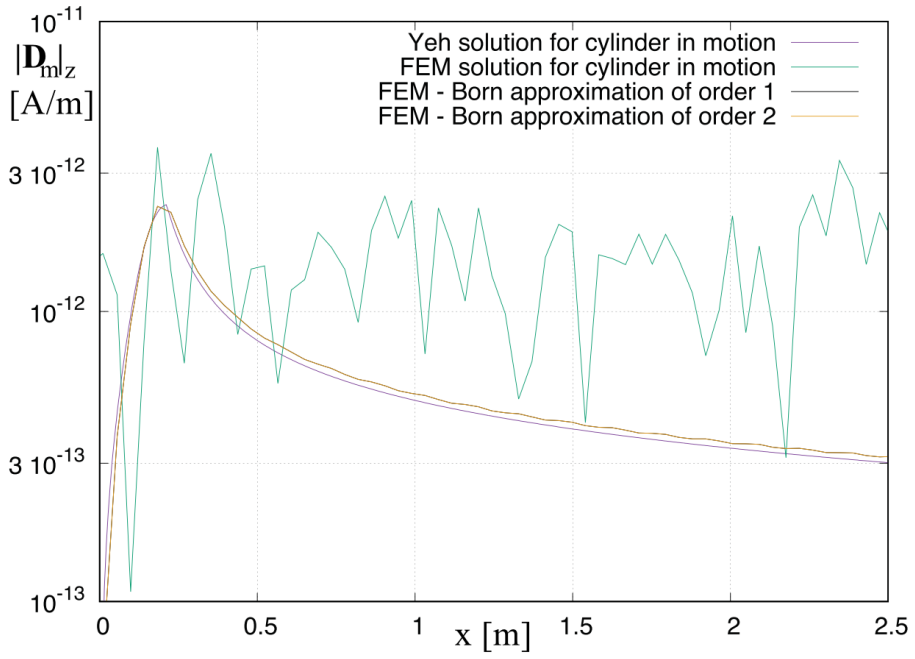

Figure 4.6: Approximations for $|\mathbf{D}_m|_z$ along the x axis for $\beta = 10^{-7}$, $\delta = 10^{-8}$, $p = 140$ and $\epsilon_r = 1.01$.

scattering problem (see Section 1.4). Finally, we implement the novel approach of 3D BAs to obtain the scattering field from the moving cylinder.

4.2.2.1 Solution for the Stationary Cylinder of Finite Length

BCs for the numerical domain are exact analytically obtained by solving the scattering problem on an infinite circular cylinder [39]. The boundary value problem is formulated in the same way as in [76], thus the BCs are equivalent to those of an infinite cylinder. According to [76, eq. (1)] we are using the following boundary conditions for the external faces of the domain:

$$\mathbf{H}^{tot} \times \mathbf{n} - Y \left(\mathbf{n} \times \mathbf{E}^{tot} \times \mathbf{n} \right) = \mathbf{f}_R. \tag{4.2}$$

Model geometry parameters are defined by values as $R = 0.6$ m and $a = 0.2$ m as it is shown in Table 4.1.

Figure 4.7 shows a comparison of FE solution and classical analytical solution. We make a comparison for two cylinder heights $l = 0.3$ and $l = 0.6$ m. In the first case, discretization is performed for the values $p = 60$, $q = 30$. In the second case, to preserve the mesh quality, we use $p = 60$, $q = 60$. The residual of the iterative solver δ is equal

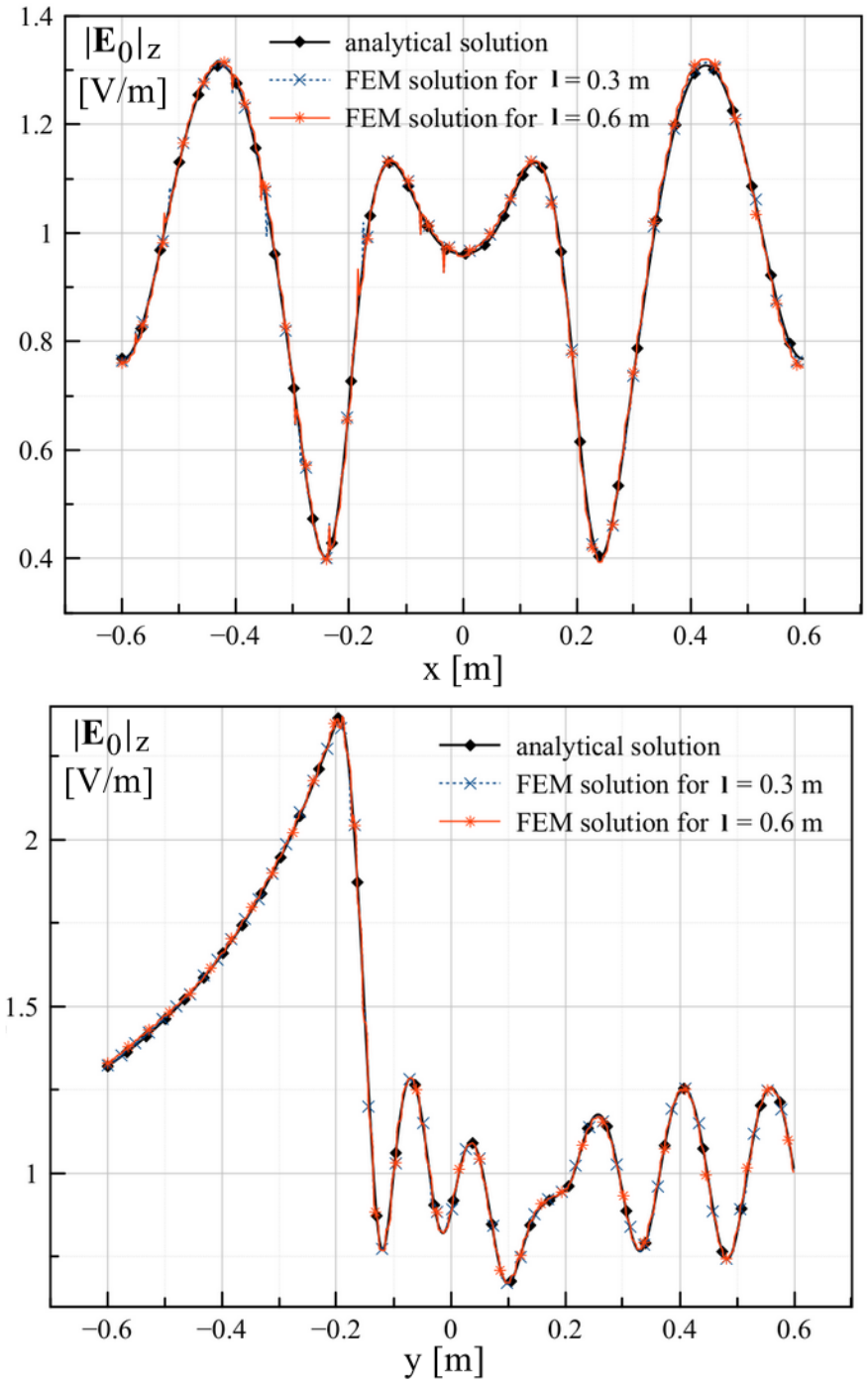

Figure 4.7: Comparison of the results of numerical and analytical calculations for the stationary cylinder. $|\mathbf{E}_0|_z$ field distribution along the x (at the top) and y (at the bottom) axis with $\delta = 10^{-12}$.

to 10^{-12}. We may note a good agreement between the results as well as the absence of a significant dependence on the height of the cylinder, which confirms the validity of the approach in setting the boundary conditions.

4.2.2.2 Classical BA for the Stationary Cylinder of Finite Length

Let us solve the classical problem of approximating a weak scatterer by equivalent sources [78]. Thus, we verify the applicability of the BAs in the three-dimensional case. There is no magnetic currents in such a problem and incident electric field has only z component. In our particular case, (1.13) takes the form

$$J_{e,eq,ba,1,z} = j\omega\epsilon_0 \left(\epsilon_r - 1\right) E_z^{inc}. \tag{4.3}$$

To obtain inhomogeneous BCs in this case, we must rewrite expression (4.2) as follows:

$$\mathbf{H}^{sc} \times \mathbf{n} - Y \left(\mathbf{n} \times \mathbf{E}^{sc} \times \mathbf{n}\right) = \mathbf{f}_R. \tag{4.4}$$

In this particular case, we have an analytical solution for the scattered fields [39] and we can immediately apply it to the corresponding calculations (4.4).

Figure 4.8 shows the results of calculating a certain system configuration. The quantity $\mathbf{D}_a$ in this case represents the difference between the system states in the presence and in the absence of the scatterer. The distribution of the quantity along the x and y axes matches the analytical solution with good accuracy. As expected, the distribution along the z-axis shows significant errors near the upper and lower boundaries of the cylinder. Therefore, these results can be considered reliable only in the immediate vicinity of the cylinder's center.

4.2.2.3 Novel BA methodology for the Cylinder of Finite Length in Axial Motion

Figure 4.9 shows some of the obtained results for the first-order BA. The results are in good agreement with those obtained by a semi-analytical technique. It should be noted, however, that these results do not provide a comprehensive verification. Firstly, they present field components that are affected only by the first-order of β, and secondly, they are obtained in the plane containing the origin, which is perpendicular to the z-axis. In contrast, Figure 4.10 presents the distribution of $\mathbf{D}_e$ along a straight line parallel to the z axis passing outside the cylinder, together with the component that is controlled by β^2. We can note that the error associated with assigning boundary conditions to the faces of

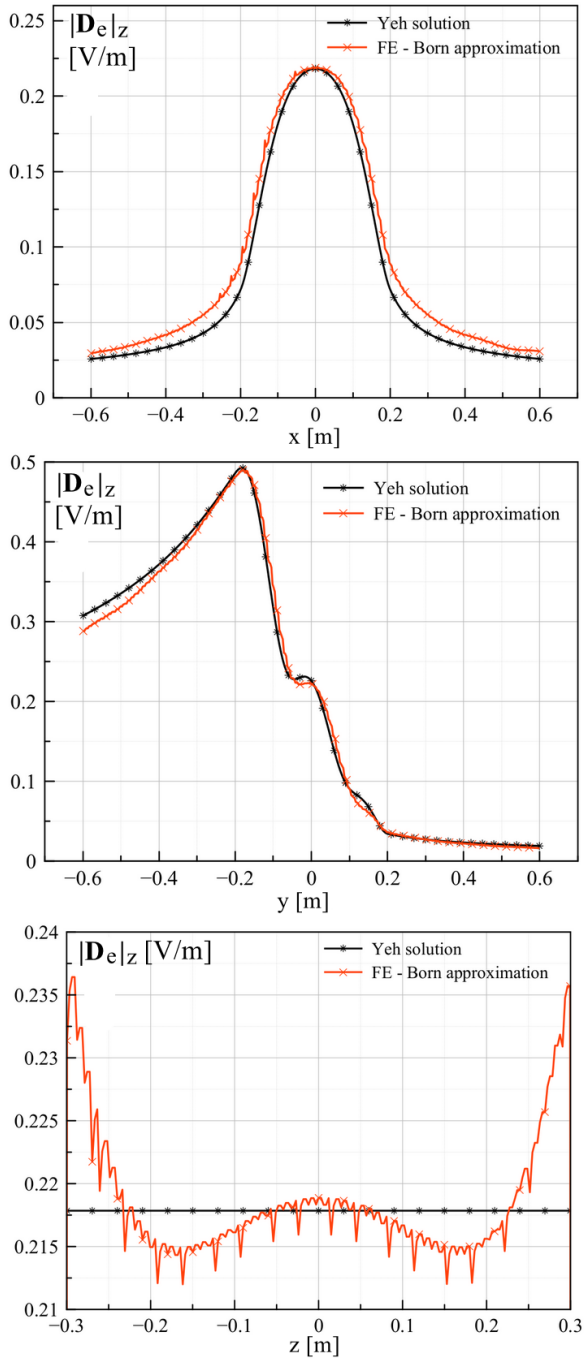

Figure 4.8: Comparison of the results of numerical and analytical calculations for the stationary cylinder classical BA. $|\mathbf{D}_e|_z$ distribution along the x (at the top), y (at the middle) and z (at the bottom) axis. System parameters are $l = 0.6$ m, $p = 60$, $q = 60$, $\epsilon_r = 1.1$ and $\delta = 10 \times 10^{-12}$.

the cylinder, even for the second order effect (Figure 4.10 at the bottom), is not critical. Similar results obtained along a line passing inside the cylinder exhibit significantly larger errors (see the lower plot in Figure 4.8).

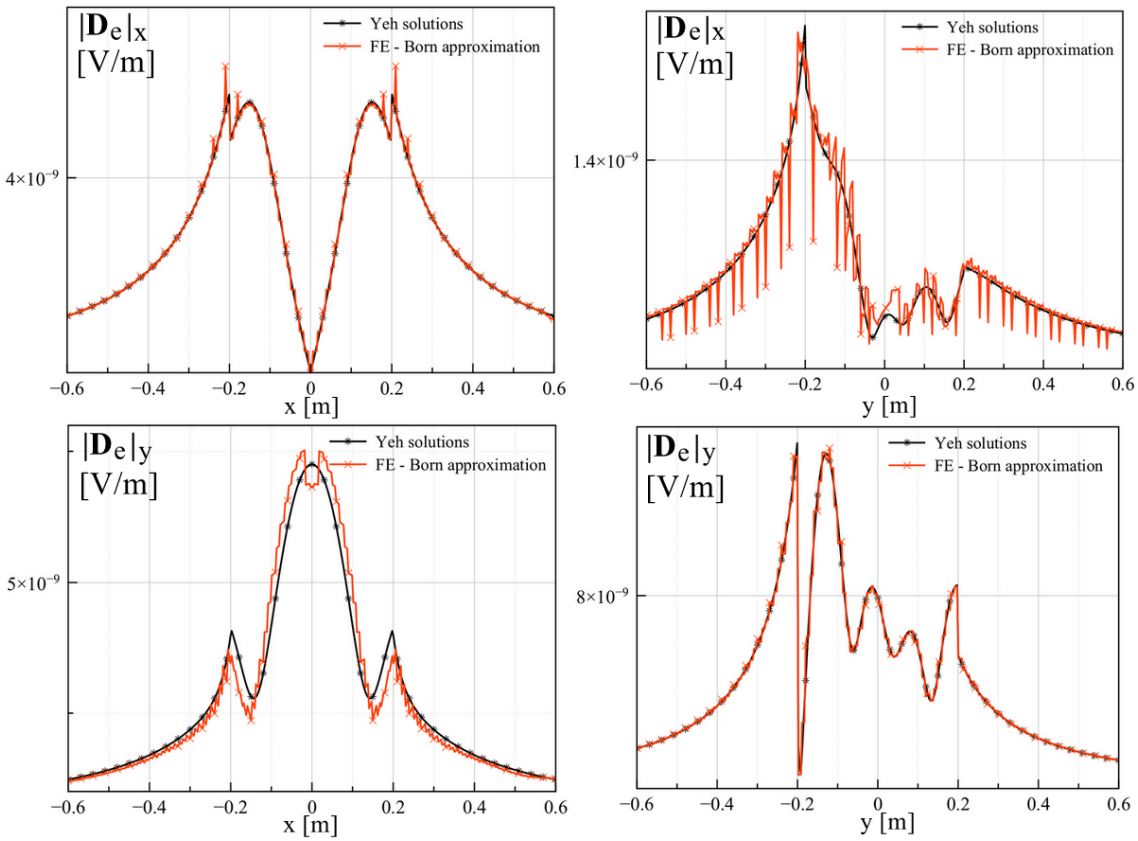

Figure 4.9: Comparisons of the transversal parts of the $|\mathbf{D}_e|$ field. Results obtained for: $\beta = 10^{-8}$, $\delta = 10^{-12}$, $l = 1.2$ m, $p = 60$, $q = 120$ and $\epsilon_r = 2$.

In [73], results identical to those shown in Figure 4.9 are presented, but accompanied by calculations performed using the classical FE difference approach. The comparison showed that the traditional FE difference does not provide reliable results for this class of problems. The results shown in Figure 4.10 are obtained under the fake BAs condition (see Section 2.4.3), so they demonstrate the error of the FE solver and not the methodology uncertainties.

The accuracy of the proposed BAs strongly depends on the value of the parameter q. This dependence arises because the equivalent currents, which do not depend on the z-coordinate, are computed in exactly the same manner as in the two-dimensional case. As a result, the current density is uniformly distributed along the cylinder, and its value is identical along any straight line parallel to the z-axis. To satisfy this condition in the three-

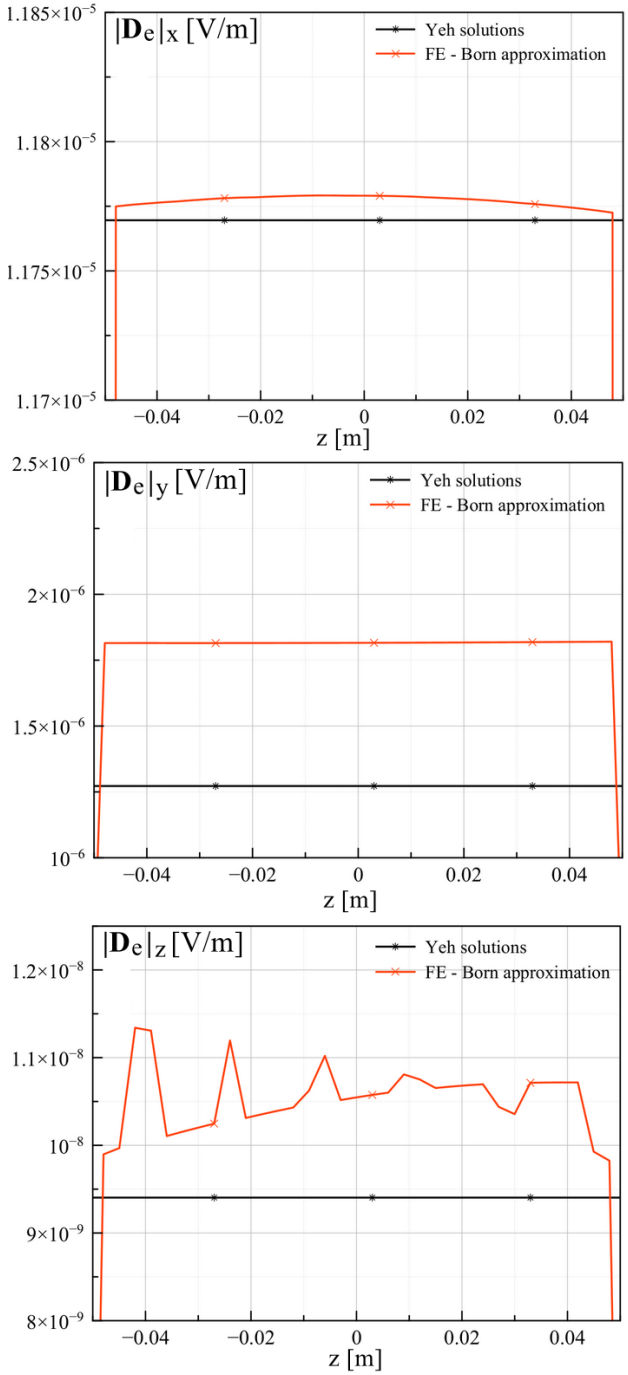

Figure 4.10: Comparisons of the results for all Cartesian components of $|\mathbf{D}_e|$. The field was calculated along a straight line parallel to the z axis with x and y coordinates equal to (0.5 ; 0.5) m. Results obtained for: $\beta = 10^{-4}$, $\delta = 10^{-12}$, $l = 0.1$ m, $r = 0.2$ m, $p = 60$, $q = 120$, $\epsilon_r = 2$.

dimensional case, a sufficiently fine mesh along the axial direction inside the scatterer is required.

4.2.3 Beyond Double Precision

A number of the results presented above clearly demonstrate the impossibility of analyzing weak media motion effects using the traditional difference method, in which the solutions for the two system states are obtained from the native finite element solver (see Section 1.5). This is evident from the comparisons shown in Figures 4.4,4.5 and 4.6. This was also noted in [73, p. 2] during the verification of the methodology for the 3D problem.

Since FEM solutions strongly depend on parameters such as p, q and δ, whereas semi-analytical solutions do not, the latter can clearly demonstrate the inherent issues of difference approach when using double-precision arithmetic. One such example, obtained during the verification of the methodology for the 2.5D problem, is shown in Figure 4.11. In this case, FE difference is completely unreliable. The difference between the semi-analytical solutions is also inaccurate. It is evidently affected by numerical noise and, moreover, it is not 10^6 times smaller than the corresponding plot in Figure 4.3, as it should be. In contrast, $|\mathbf{D}_{e,ba1}|_z$ and $|\mathbf{D}_{e,ba2}|_z$ closely match the corresponding plots from Figure 4.3, with the correct scaling. We can assume that these results are novel from a scientific point of view and cannot be strictly verified by existing methods. We can reasonably assert the possibility of scaling the results for small values of β, since the parameters ϵ^v and μ^v do not depend on the first order of β (see (1.5)), while ξ and ζ, at low velocities, depend on β almost linearly (1.8).

A similar result, obtained for a higher value of β but for a rarefied medium, is shown in Figure 4.12. This result was obtained for parameters similar to those shown in Figure 4.6, but for the electric difference field. The FE difference method yields a random cloud of points, whereas the result obtained using the semi-analytical traditional difference, although closer to the true level (unlike in Figure 4.11), is still strongly affected by numerical noise and lies at the limit of double-precision arithmetic sensitivity.

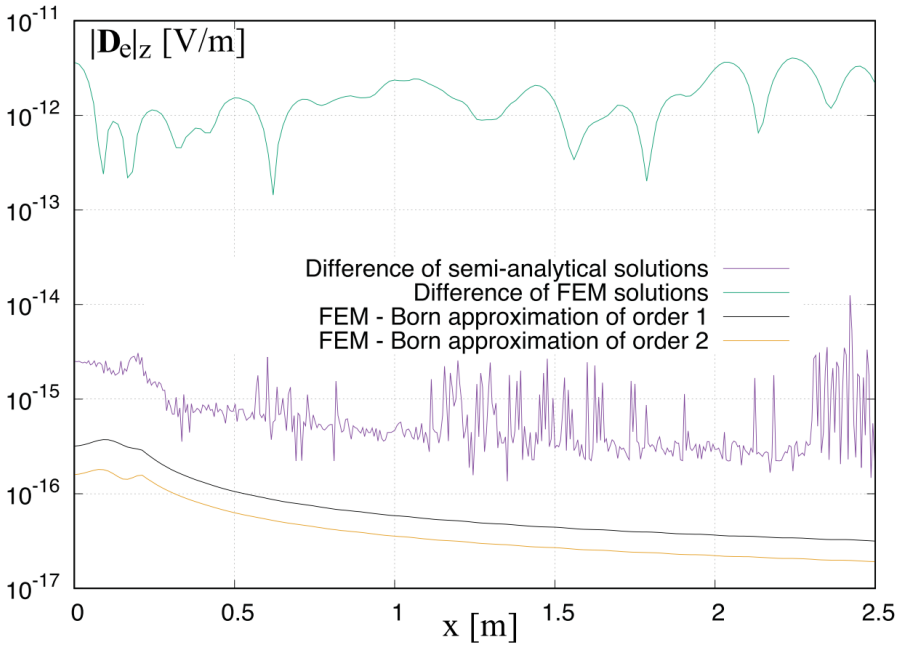

Figure 4.11: Approximations of $|\mathbf{D}_e|_z$ along the x-axis for $\beta = 10^{-8}$, $\delta = 10^{-12}$, $p = 196$ and $\epsilon_r = 2$.

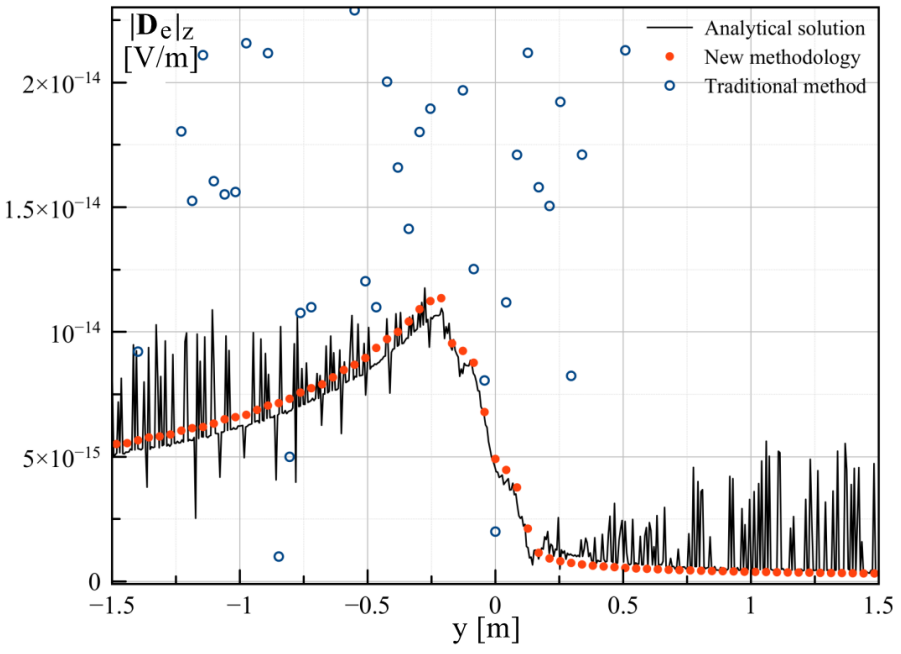

Figure 4.12: Approximations of $|\mathbf{D}_e|_z$ along the y-axis for $\beta = 5 \times 10^{-7}$, $\delta = 10^{-12}$, $p = 140$ and $\epsilon_r = 1.01$.

4.3 Verification of the Methodology Implementation in COMSOL

In this section, we present the verification of the algorithm implementing the BA methodology in COMSOL, which is described in detail in Chapter 3. First and foremost, we assume that the BA methodology implemented within the native FE solver has been fully verified and provides reliable results, at least for 2.5D problems. Thus, we do not present any comparison with traditional difference methods here, considering such results unnecessary. We present the results of the analysis of a 2.5D scattering problem, whose parameters fully correspond to those used in the verification of the general methodology (see Section 4.1 and Table 4.1).

Figure 4.13 shows the geometry of the two-dimensional problem in COMSOL interface. The outer boundary of the numerical domain $\partial\Omega$ (see Figure 2.1) has the scattering boundary conditions with impedance equal to Z_0 constant. According to the geometry shown, the path $s = R - a$ (this quantity is required to determine the value of T_t in (3.2)). An example of the assigned equivalent current distributions over the current definition domain after interpolation was already shown earlier in Figure 3.3. Some illustrative results, not related to the verification process, were also previously shown in Figures 3.4 and 3.5.

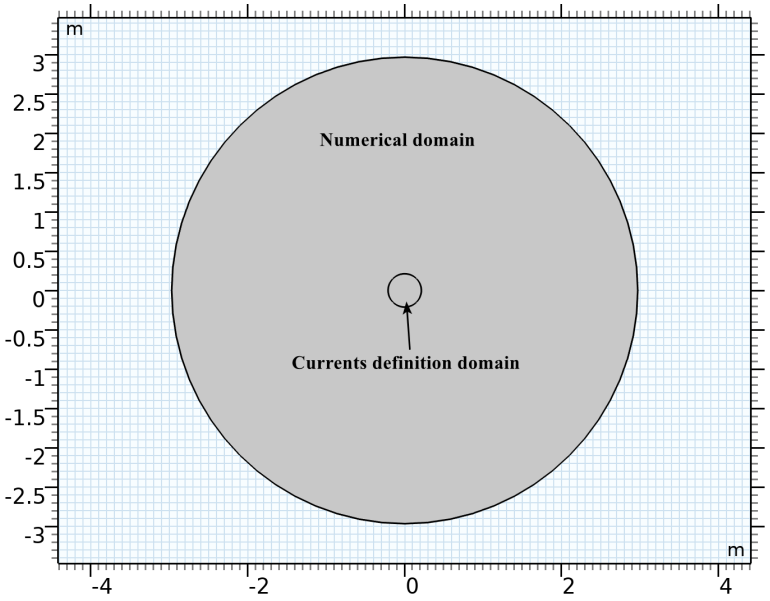

Figure 4.13: 2.5D problem geometry in COMSOL interface.

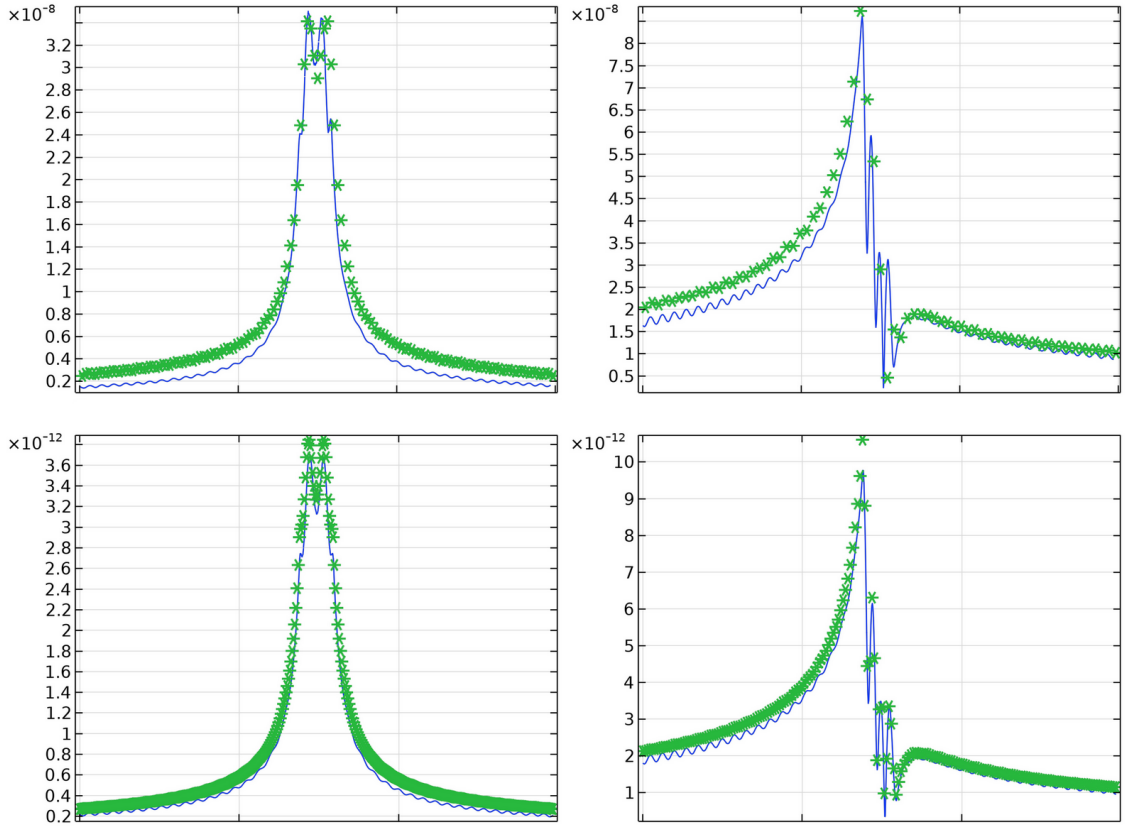

Figure 4.14: Comparison of the $|\mathbf{D}_e|_z$ field distribution calculated in native solver (green asterisk marker) and in COMSOL (blue line) for the $\beta = 10^{-4}$ (at the top) and $\beta = 10^{-6}$ (at the bottom). Left-hand side for line along x axis, right-hand side for line along y axis.

Figure 4.14 presents a comparison of the results obtained in COMSOL and in the native solver. As described in Section 3.3, to obtain these results, the computational mesh was first generated in COMSOL, then imported into the native solver, where the solution was computed. Thus, identical meshes were used in both the native solver and COMSOL. In this case, we cannot describe the computational mesh using the parameter p typically employed in the native meshing procedure. It should be noted that the mesh was generated according to the standard COMSOL meshing rules for the frequency $f_m = 1.5 \times f$. To satisfy the requirement given by (3.3), we used the following discretization parameter values: $n_s = 512$ and $n_f = 200$.

The distributions of the quantity $|\mathbf{D}_e|_z$ shown in Figure 4.14 agree well with the results obtained from the native solver. The minor oscillations observed in the values are associated with the specifics of the TD solution and the formulation of the equivalent

sources given in (3.1). The magnitude of these oscillations noticeably decreases when the discretization parameters n_s and n_f are refined.

The verification of the BA implementation in COMSOL can be considered partially complete. Completing the verification of the methodology and its implementation is a priority for future research. The following chapter describes experiments that can be validated using the BA methodology implemented in COMSOL, which is of crucial importance for the overall project.

CHAPTER 5

Experiments on the Interaction of EM Waves with Moving Media

Experimental investigation is an essential part of the methodology verification process. We conducted a series of experiments on the interaction of electromagnetic waves with moving media. However, at the present stage, the obtained experimental results cannot be interpreted unambiguously. This is due to the fact that in all our experiments, the moving media possesses a nonzero electrical conductivity σ. The requirement of $\sigma = 0$ for the media at rest represents the main limitation for the analysis to date [75, sec. 1]. By adhering to a strictly formal approach, we did not investigate possible acceptable approximations of $\sigma \approx 0$ for various β and material parameters that would not introduce significant computational errors and could be considered negligibly small. Such an investigation is part of the methodology generalization described in Section 6.1.

The charge density present in the media at rest in L' undergo Lorentz transformations when observed from L [2] (see Figure 1.1). In moving media, a current arises similar to the one described in [72]. The surface current modifies the boundary conditions on the scatterer. For a material with nonzero conductivity at rest, its parameter values ϵ^v, μ^v, ξ, ζ must also be recalculated, and the formulations presented in Section 1.3 need to be modified accordingly. Accounting for these effects significantly complicates the analysis process and requires further investigation.

It is important to note that considering a lossless moving media does not constitute a methodological limitation of the BA approach. For this reason, it was not addressed in Section 2.4.2. The main applicability conditions of the BA methodology have already been described in Sections 1.4 and 2.1 and do not require further clarifications. Moreover, they can be significantly weakened [28], and the inverse BA procedure has been applied to highly conducting bodies [13]. Thus, this is a general limitation for computing the

The main content of this section was published in [79] and [80]. The results were also presented at IEEE International Conference on Microwaves, Communications, Antennas, Biomedical Engineering and Electronic Systems (COMCAS), held in Tel-Aviv, Israel (2024) and at 6^{th} International Conference in Electronic Engineering & Information Technology (EEITE), held in Chania, Greece (2025).

system's state 1 (media in motion), and it also applies to traditional difference methods [30, 49, 51, 75] (see Section 1.5).

At the same time, using a material with $\sigma = 0$ at rest in experiments appears to be impossible. It is likely that the effect of nonzero conductivity can be minimized (or even neglected) when studying the motion of gases. In the simplest case, this gas can be air, whose conductivity under normal conditions varies within the range of $\sigma \in [10^{-14} \div 10^{-12}]$ S/m [81, figs. 7, 15 and sec. 7]. However, designing an experimental setup to study gas motion proves to be more challenging from an engineering perspective than, for example, studying liquid motion. It is quite possible that higher-order values of conductivity will also have little effect on the results. As noted above, this question remains open.

Therefore, we have experimental data, but we lack a reliable method for its interpretation. In Section 3.4, we noted that one of the important applications of the BA adaptation in COMSOL could be the validation of experimental data through numerical simulation. If the simulation results of the weak motion effects match the experimental data, the methodology can be considered fully verified. Simultaneously, this would also confirm the practical significance and the potential applicability of these effects, as discussed in Section 1.6.

5.1 General Characteristics of the Experimental Study

All the experiments we conducted were carried out using a waveguide transmission line (TL). One of the waveguide ports is excited by the fundamental mode, while a pipe containing the medium under study is placed inside the TL cavity. The specific parameters and configurations of the experimental setups are presented in the corresponding section. Here, we will limit ourselves to a discussion of the general features.

The waveguide measurement method offers several notable advantages. In a waveguide with a standard cross-section, plane-wave propagation is well described by analytical models [82]. Importantly, the waveguide cavity is shielded by its metallic walls, forming a closed system inherently protected from external interference and noise. Moreover, a section of the waveguide can effectively operate as a cavity resonator [83]. The perturbation method, widely employed in resonator studies, allows for highly precise measurements and provides significant flexibility for system adjustments [84, 85, 86]. Additionally, waveguide transmission lines can incorporate a variety of passive elements to further enhance measurement accuracy [87]. By optimizing the cross-sectional geometry of the

waveguide, electromagnetic power can be concentrated, thereby improving sensitivity. It should be noted that a theoretical study of the propagation of guided waves in a moving medium has been conducted [88], which supports the analysis presented here.

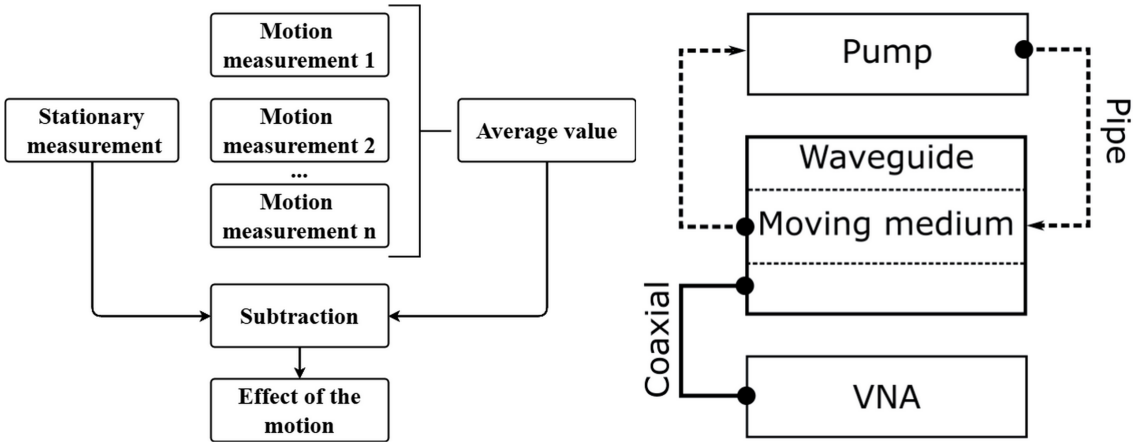

Figure 5.1: Experimental data processing flowchart (on the left). Generic experimental installation scheme (on the right).

Figure 5.1 (on the left) presents the measurement scheme used for processing the experimental results. This setup corresponds to a standard configuration for testing flowmeter devices and their embedded algorithms, which are primarily benchmarked against acoustic measurement methods [7]. Stationary measurements are employed as a reference for calibrating the experimental setup. When the number of measurement iterations, denoted by n, during medium motion is sufficiently large, the magnitude of systematic parasitic effects is significantly reduced during the subtraction stage. Various regression-based techniques can then be applied for data post-processing, as discussed in [89]. Furthermore, [90, 91] explored the feasibility of developing an intelligent system based on self-aware cognitive radio for the retrieval of material parameters, including weak bianisotropy [92].

It is not difficult to observe that the processing of measurement data for extracting motion effects is analogous to the difference used in traditional methods. Therefore, for the experiments conducted, it is critical that the only significant distinction between the system's state 0 (media at rest) and state 1 (media in motion) be associated with the effect of induced bianisotropy. Possible accompanying effects are discussed in detail in Section 5.3. Minimizing their magnitude and influence is a key objective in the optimization and design of the experiment [87, 89].

In our experiments, we measure the S-parameters of the TL. For a single-port measurement in a cavity resonator, we measure S_{11}, and for a two-port configuration, we

additionally measure S_{21}. Thus, the procedure for processing the measurement results is carried out as follows:

$$D_s = \left| S_{11,0} - \frac{\sum_{i=1}^{n} S_{11,1,i}}{n} \right|, \tag{5.1}$$

where D_s represents a difference analogous to $\mathbf{D}_a$, but in scalar form. As usual, the subscripts 0 and 1 correspond to the system at rest and in motion states, respectively. An analogous procedure is applied to S_{21} as well. In the present work, we present results only for the magnitudes of the S-parameters.

Figure 5.1 (right-hand side) shows the general scheme of the measurement setup. A vector network analyzer (VNA) is connected to the waveguide TL via coaxial cables (this applies to both single-port and two-port configurations). The motion of the liquid inside the pipe piercing the waveguide cavity is generated by a pump. The simplicity of the setup is its main advantage. The experiment can be significantly optimized, as the scheme is flexible and offers great potential for enhancing sensitivity.

Below, we summarize the key aspects of the experiment optimization (see [80]). All relevant data regarding the construction and operation of the laboratory setup can be found in [87]. It is worth noting that the moving medium in the waveguide can be equivalently replaced with a stationary bianisotropic material in order to apply the measurement scheme described in [90].

We have already noted that the waveguide walls shield the cavity from external EM noise and interference. During the experiment, we can be confident that external sources will not significantly distort the measurement results. Thus, the primary source of this type of noise is the signal generator. Deterministic and stationary noise from the generator is minimized by subtracting the results of different measurements, as shown on the left in Figure 5.1. VNA noise is filtered by setting a narrower intermediate frequency (IF) bandwidth (BW) [93]. Calibration, temperature stability, and adherence to general VNA operating recommendations also reduce the impact of noise.

Temperature fluctuations in the experiment constitute a major source of inaccuracies and errors. Maintaining a stable temperature is therefore one of the most critical tasks. Even a slight deviation of 0.1 degrees Celsius during measurements, however, can introduce significant errors. Nonlinear ferrite elements within the waveguide TL are used to decouple the directions of the incident and reflected waves [94, p. 475]. This setup imposes certain constraints on the guided wave power necessary for reliable effect detection.

In this regard, further optimization of the waveguide cross-section to better redistribute power along the TL could produce results of substantial interest. Extensive preliminary experiments have shown that the cavity resonator approach provides significantly higher accuracy compared to two-port measurements. In all experiments, the same pump is used, operating at full power and generating a liquid flow with an average velocity v_{av} of approximately 3.3 m/s. Thus, for all our experiments, $\beta_{av} \approx 1.1 \times 10^{-8} \in \beta_{slow}$ (see Section 1.6). Double distilled water of identical standard is employed in all experiments. The conductivity of medium is $\sigma \approx 5.5 \times 10^{-6}$ S/m. The properties of water, in terms of dielectric spectroscopy and conduction mechanisms, are discussed in [95, sec. 3.1, p. 189].

In all the experiments presented in Section 5.2, we used a coaxial waveguide adapter Agilent X281A for WR90 TL. This line is standardized for the X-band and consists of a rectangular waveguides. Agilent adapter is well-known and has an semi-analytical representation [96]. As the measuring device we used Rohde & Schwarz ZVA-50 with R&S ZV-Z91 phase-independent coaxial cables. The IF BW value for all experiments is 1 kHz. A peristaltic industrial pump GZL-50 was used. The input power level was –10 dBm. The pipe is made of high-density polyethylene (HDPE). The pump and the waveguide TL are placed on damping supports that absorb vibrations. In all experiment, a water tanker is used, which creates an overpressure at its lowest point of 4.5 kPa.

5.2 Description of the Conducted Experiments

In this section, we present two complete and valid experimental datasets. The most significant experimental results were described in [89]. A photograph of the experimental setup used for the first group of experiments is shown in Figure 5.2. The components used are also detailed there.

In this case, the measurements were carried out using the cavity resonator method. To maximize the volume of electromagnetic power interacting with the moving medium, the pipe was aligned along the wide wall of the waveguide; however, this solution proved to be ineffective. Temperature and vibration isolation of the hydraulic system and electrodynamic components were accomplished using damping and thermal insulation materials (without spatial separation of them). At the adapter flange plane, a full one-port calibration was carried out using the standard open–short–match algorithm [93, p. 106]. It is important to emphasize that during the experiments, the calibration was performed with

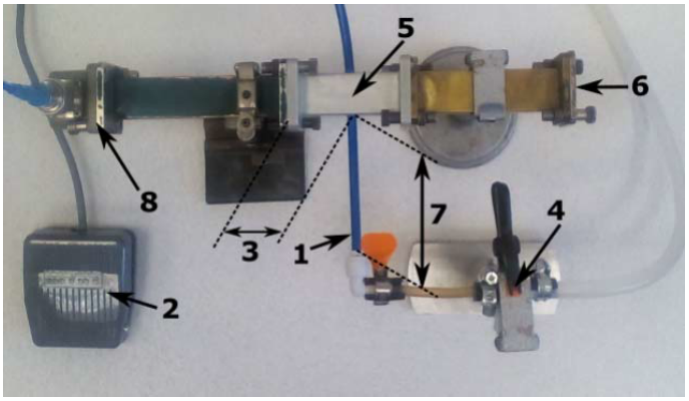

Figure 5.2: Laboratory installation for the first group of experiments: 1 – pipe with water (at rest or in motion), 2 – pump control, 3 – waveguide with length equal to λ at f = 10 GHz, 4 – check valve, 5 – observation area, 6 – short measure, 7 – flow developing path, 8 – coaxial waveguide adapter.

the waveguide containing the pipe with water at rest. Consequently, measurements taken with the water at rest serve as a 0 state for all observed effects. Additionally, this approach is consistent with the cavity perturbation method [83, 85, 86].

Let us provide additional clarifications regarding the setup shown in Figure 5.2 The scatterer is positioned several wavelengths away from the port for any frequency within the X-band (item 3) in order to minimize the influence of higher-order modes of the scattered waves. The check valve (item 4) prevents water from flowing in the opposite direction when the pump is turned off. To ensure that the flow in the observation area is fully developed, a straight section of the pipe with a length exceeding ten times its inner diameter, which is equal to 5.2 mm, is placed before it (item 7). Raw data from one of the measurements, captured directly on the measurement device, are shown in Figure 5.3.

A photograph of the experimental setup used for the second group of experiments is shown in Figure 5.4. The second set of experiments was performed in two-port mode. As noted earlier, this configuration slightly decreases measurement precision but provides additional data for processing and analysis, particularly the S_{21}. A key difference in this setup is that the water pipe is aligned along the waveguide's narrow wall. This adjustment significantly enhanced both the stability and accuracy of the measurements. There are two main reasons for this. First, a semi-analytical solution exists for this geometry, as described in [97]. This allows us to assess the measurement accuracy for water at rest. Second, with the flow oriented along the gravity vector (from top to bottom in Figure 5.4), it becomes more uniform. VNA and the pump are spatially separated now (placed on different surfaces).

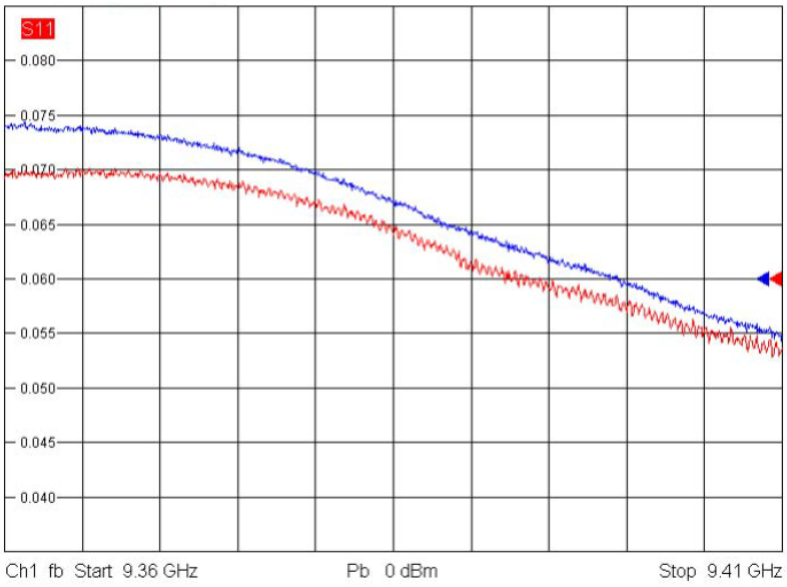

Figure 5.3: Raw results obtained from the first experimental setup. The image displays the VNA interface for the $|S_{11}|$ [dB] parameters measurements during water at rest (blue line) and water in motion (red line). Displayed frequency range: 9.36 GHz – 9.41 GHz.

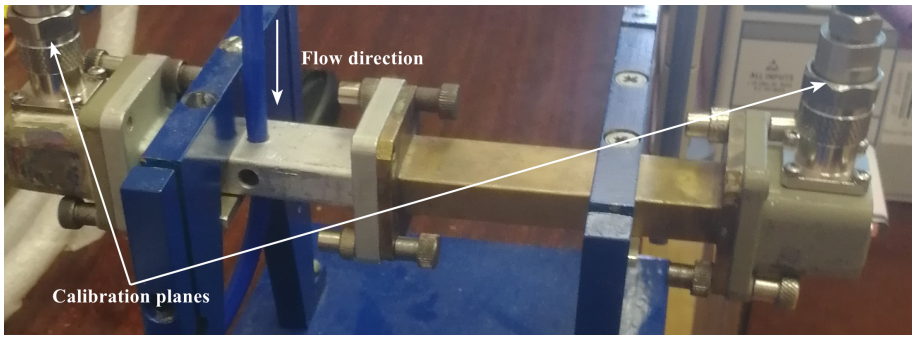

Figure 5.4: Laboratory installation for the second group of experiments.

A significant modification in the revised experimental protocol concerns the calibration of the TL. Calibration performed via waveguide measurements (at the adapter flange plane) is relatively imprecise, even when all standard recommendations are followed [93, sec. 3.3]. Using high-precision coaxial measures considerably enhances the calibration quality. The procedure itself remains unchanged, but for the two-port configuration. We only shifted the reference plane (the coaxial cable end, as illustrated in Figure 5.4) and changed the instruments used. Figure 5.5 shows some of the results obtained from these experiments.

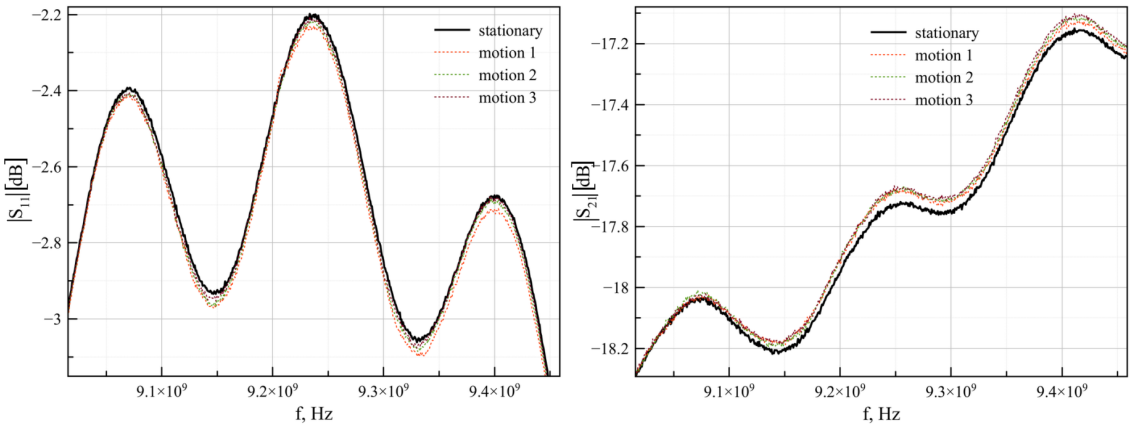

Figure 5.5: Raw results obtained from the second experimental setup. Frequency dependence of the $|S_{11}|$ [dB] and $|S_{21}|$ [dB] parameters measurements during water at rest and water in motion ($n = 3$ successive measurements).

It is possible to compare the $|S_{11}|$ results from the two independent experiments presented in Figures 5.3 and 5.5. Here, our main focus is on the trend and magnitude of the observed effect. We can infer that the experiments exhibit considerable external validity, and the results are reproducible. The downward trend in the reflection coefficient during flow initiation remains evident, with a comparable effect on the magnitude. Section 5.4 presents a descriptive analysis of the measurement results obtained from the second setup.

5.3 Accompanying Effects of Motion

The effects of medium motion are not only related to the effects of weak bianisotropy. Theoretically, these effects should be the only ones present if all the conditions described in Section 1.1 are satisfied, that is, when all time-dependent effects are excluded. However, in practice, it is very difficult to achieve this. In this section, we provide a brief description of the possible accompanying effects.

Table 5.1 summarizes the considered effects and classifies them according to key qualitative characteristics. The inertia of an effect indicates how quickly it appears when the system transitions from state 0 to state 1. We do not aim to determine the exact time it takes for an effect to develop. For qualitative assessment, we only indicate that there is no inertia if the effect appears below a threshold time for measurement; otherwise, we indicate that inertia is present. The order of the threshold measurement time is 10^{-2} s. The same applies to relaxation. This is a characteristic of the effect that indicates how quickly

the effect disappears when the system transitions from state 1 to state 0. For some effects, these characteristics cannot be determined in general, as they occur randomly. As all the effects under consideration are time-dependent, we characterize their behavior, which can be a trend, a plateauing trend, periodic, or random. For a trend, inertia determines the rate of its increase, whereas relaxation determines the rate of its decrease.

Table 5.1: Effects accompanying the media motion in the experiments.

Effect	Inertia	Relaxation	Behavior in time
Deformation	Yes	Yes	Random or plateauing trend
Vibration	No	No	Random or periodic
Cavitation	Undefined	Undefined	Random
Shaping	Yes	No	Random
Pulsation	No	No	Periodic
Friction	Yes	Yes	Trend

Pipe deformation under water flow pressure represents the most unpredictable effect. The behavior of the scattered field during deformation may be random or exhibit a trend that eventually reaches a plateau when the maximum mechanical stress in the pipe is attained. Deformation can disrupt the entire experiment, as relaxation may require a long time or may not occur at all in the case of inelastic deformation. To mitigate this effect, a tube made of HDPE plastic is employed. With a wall thickness of 0.79 mm, the pipe can withstand a maximum pressure of approximately 3 MPa, as determined using the classical Barlow formula.

The main source of vibration is the peristaltic pump. We minimize the influence of this effect by all available means, but we still cannot be completely certain of its absence. Vibrations from the pump can propagate both to the pipe inside the waveguide and to the coaxial cables connected to the VNA. In the first case, this would result in micro-Doppler time-dependent effects [98, 99]. Vibrational signals can be either random or periodic, manifesting as amplitude and phase modulations of the reflected signal. Typically, this effect can be easily observed without advanced processing, simply by tracking the measured S parameters over a period of time.

In certain cases, cavitation can occur in turbulent flows [3]. The treatment of cavities forming in the flow is discussed in [100]. The presence of air cavities alters the effective permittivity of the scatterer. However, in any flow, these cavities move randomly, and their concentration varies with time. Consequently, this effect resembles random noise. The same applies to the movement of any other inclusions within the flow.

When a developed flow encounters any inhomogeneity in the hydraulic system, it requires additional time before it becomes developed again. This effect is referred to as flow profile shaping. In our experiments, we are dealing with the turbulent flow. For the velocity profile function, we have [3]

$$v(\rho) = \frac{v_{av}(\kappa+1)(2\kappa+1)\left(1-\frac{\rho}{a_{in}}\right)^{\frac{1}{\kappa}}}{2\kappa^2}, \tag{5.2}$$

where κ is the hydraulic coefficient, which in our case equals 6.4, ρ is the radial coordinate, and a_{in} is the inner radius of the cylinder (see Figure 4.1). Thus, the maximum velocity in the profile ($\rho = 0$) is equal to 4.12 m/s. Changes in the velocity profile can be attributed to motion effects, however, these effects exhibit random behavior in time and are not the focus of our investigation.

In addition to mechanical vibrations, the pump can also be a potential source of pulsations in the flow [3]. These pulsations may appear as alternating regions of increased and decreased pressure within the flow. When comparing pumps by type, including vibrational and rotary ones, peristaltic pumps exhibit the highest level of pulsations. This is directly related to their operating principle. These pulsations are low-frequency (a few hertz), whereas in vibrational pumps they occur at frequencies of tens of hertz, and in rotary pumps the flow is almost free of pulsations. In a laminar flow, these pulsations can propagate over a considerable distance from the pump, whereas in a turbulent flow they are present only in its vicinity. For a peristaltic pump, this effect is strictly periodic and can be easily detected.

The flow-induced skin friction along the pipe walls can generate a radial temperature gradient. Skin friction can be assessed using temperature transfer methods [101], ultrasonic sensors [102], or micro-electro-mechanical systems [103]. The ratio of thermal boundary layer to dynamic boundary layer in our case roughly equal to 0.44 and the skin friction coefficient is 0.009 [79]. Thus, we have a thin boundary layer in which the kinetic energy is converted into heat with an efficiency equal to Stanton number. In general, this effect is expected to exhibit a characteristic trend, while also being time-dependent (possessing macroscopic inertia) and relaxing when the motion ceases (returning to thermal equilibrium). Flow thermal stabilization to minimize this effect can be crucial in this context.

5.4 Descriptive Analysis and Exclusion Method

Figure 5.6 shows the processed data for the $|S_{11}|$ and $|S_{21}|$ parameters obtained in the second group of experiments. The raw data were shown earlier (see Figure 5.5) and the processing was performed according to (5.1) with $n = 3$. The acquired experimental data shown in Figures 5.3, 5.5 and 5.6 allow us to derive a number of important characteristics of the study:

1. An observable effect occurs within the measurement setup, and the main question is whether this effect is associated with the weak bianisotropy of the moving medium.

2. The observed effect does not exhibit random or periodic behavior and does not show a significant time dependence.

3. The magnitude of the effect oscillates in the frequency range.

4. There is no measurable inertia and relaxation between the states of the medium. The results shown in Figures 5.3 and 5.5 are set immediately after the pump is turned on. The system returns to a rest state without noticeable relaxation processes.

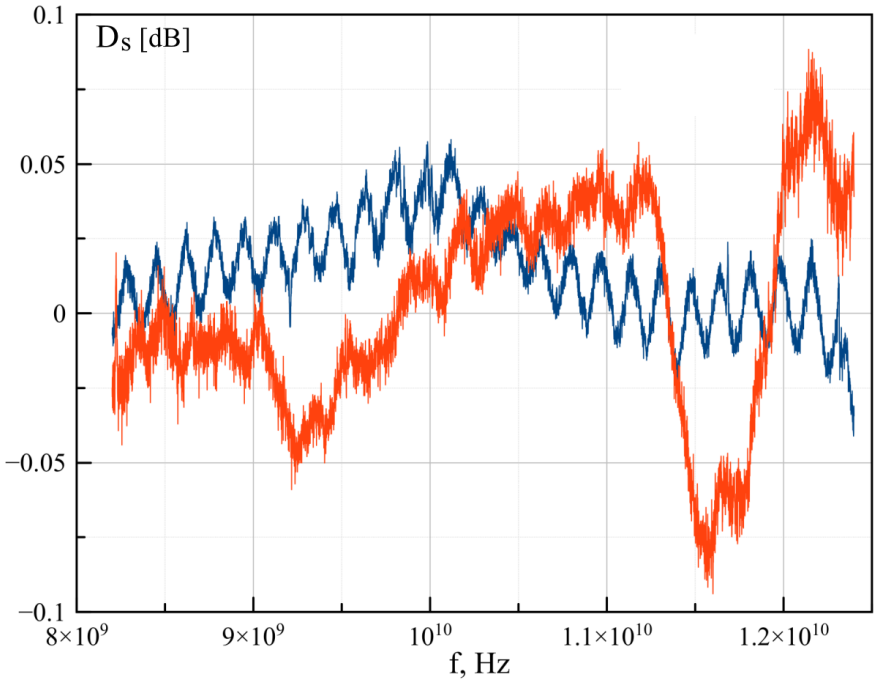

Figure 5.6: Processed $|S_{11}|$ (blue line) and $|S_{21}|$ (red line) data obtained from the second group of experiments.

In general, the specified characteristics may correspond to an effect associated with the induced bianisotropy of the moving medium. Nevertheless, as already noted, a definitive conclusion cannot yet be drawn, and the present analysis is purely descriptive. At the same time, we can attempt to exclude from consideration a number of effects listed in Table 5.1 that do not satisfy these characteristics. All effects whose time behavior is random or periodic do not have a significant impact on the results of the conducted experiments. This is an important conclusion. While we cannot be completely certain that their influence on the experiment is entirely absent, their magnitude is much lower than that of the effect observed in the frequency domain. However, we cannot rule out trend behavior in the observed effect, and this constitutes the main challenge of the present analysis. We did not observe any transient or relaxation processes during the experiments, but our current assessment of the influence of deformation and friction effects does not allow us to exclude them from consideration. A precise quantitative analysis of the influence of these effects should be carried out, for instance through the multiphysics modeling, which is one of the objectives of future research.

CHAPTER 6

General conclusion

This work presents the synthesis, analysis, implementation, and verification of a novel methodology for calculating the effects of media motion on the scattered electromagnetic field. The synthesis is based on the strict formulation of two electrodynamic problems: the first describes the system at rest, while the second represents the system with moving media. By applying the Born approximation to the total field, the difference between these states is expressed, leading to the formulation of a third problem. Solving the third problem yields the difference between the system states, which corresponds to the effects associated with media motion. A procedure was developed to implement the new BA methodology within a native FE solver. Despite some limitations in its scope, the combination of the native solver and the new methodology provides a powerful tool for subsequent analysis, as all elements and parameters of the computational core remain under full control.

We evaluated the algorithmic complexity of the new methodology, which showed that for the first-order approximation, the complexity is equal to or lower than that of traditional FE difference methods. In contrast, for the second-order BA, the algorithmic complexity exceeds that of traditional schemes, but it likely represents the maximum attainable accuracy for the numerical computation of motion effects. This is due to an intrinsic methodological feature: the lower the velocity of the object, the more accurate the BA. We find this property particularly relevant within the context of the problematization conducted. Moreover, the so-called fake BAs described in Section 2.4.3 combines the accuracy of analytical calculation methods with the advantage of directly measuring a small quantity, rather than computing it through the difference.

All limitations of using the BAs methodology in the native FE solver are removed when this approach is implemented in a commercial CAD system. The adaptation algorithm in COMSOL Time Explicit EMW Module has been developed. At the same time, to retain all the advantages of using the own code while enabling the analysis of models with complex geometries, a system for converting and importing the computational FE mesh generated in COMSOL was also developed.

The BAs methodology has been verified. For two-dimensional problems, the verification can be considered complete and sufficient, whereas a number of verification issues for the three-dimensional case were identified in Section 4.2.2. The procedure for applying the new BAs methodology in COMSOL was also verified. Since we are fully confident in the performance of the native solver for 2.5D problems, the implementation was tested using an identical problem formulation.

Finally, we described two series of conducted experiments. The first series can be regarded as a pilot study. Several significant improvements to the setup were implemented for the second series, along with a revised procedure. In its current form, the experimental setup can be considered optimal in terms of the ensuring flow uniformity within the observation area, minimizing vibrations transmitted from the pump to the observation area, and calibrating the measurement system. The research results have so far yielded only a descriptive analysis. We did not observe any significant TD effects during the experiments.

In summary of the above, our investigation demonstrates that the Born approximation is particularly effective for calculating effects of motion at non-relativistic velocities, providing both high accuracy and computational efficiency. Moreover, this approach allows systematic studies of FD scattering phenomena in arbitrarily shaped scatterers and velocity fields, making it a powerful tool for both theoretical investigations and practical applications. Below, we list several quantitative parameters of the conducted study.

According to preliminary estimates, the algorithmic complexity of the methodology for first-order BA is slightly lower than the algorithmic complexity of the traditional FE difference method. The algorithmic complexity for second-order BA is higher by no more than 50% (see Section 2.4.1). In all cases we considered, second-order BA provides highly accurate results, even in situations beyond double precision arithmetic limits (see Section 4.2.3).

The use of the methodology in COMSOL significantly increases computational efficiency compared to the native solver. For certain problems, the computation time was reduced by up to 83%, under identical mesh construction parameters and δ values. In some cases, the increase in computational performance reached 600%.

During the verification of the methodology and its implementation in COMSOL, the parameter β took values within the range from 10^{-4} to 10^{-9}. According to the classification presented in Section 1.6, the verification employed β values from range β_{slow} and partially from β_{int}.

The median value of the D_s in the first series of experiments was 1.22×10^{-3} dB. The maximum $|D_s|$ for $|S_{11}|$ in the second series of experiments was 0.051 dB, while for $|S_{21}|$ it was 0.08 dB.

6.1 Future Developments

In this final section, we will present a list of tasks for the future development of the project. We evaluate the importance and complexity of each task and establish their priorities. All tasks are divided into three thematic areas. The first one is the Methodology Generalization (MG). During our work, we identified several aspects that can be implemented to enhance the generalizability of the methodology, optimize it, or achieve additional improvements closely related to the application of the methodology, but not constituting its intrinsic limitations or properties. The tasks of this work direction are as follows.

Task MG1. Development of a formulation for absorbing boundary conditions to overcome the issues identified in Section 4.2.2. In addition to completing the verification for the three-dimensional problem, the results of this study can significantly broaden the scope of geometries that can be analyzed.

Task MG2. Application of the BA methodology for analyzing motion effects of lossy media. Estimation of the acceptable approximation of $\sigma \approx 0$ and the magnitude of the effect of nonzero conductivity. In Chapter 5, we already indicated that the requirement of $\sigma = 0$ for a material at rest is not an intrinsic methodological limitation. Thus, solving this problem can significantly expand the applicability of traditional FE difference methods as well.

Task MG3. Development of an approach for reconstructing the effects of weak bianisotropy in moving materials for a rotating non-axisymmetric body, *i.e.*, in the presence of strong time-dependent effects. This point is addressed in Section 3.4, and here we provide some additional information. We consider that in practice it is very difficult to achieve a rotational state of a body in which the electromagnetic waves scattered from the object would not experience any TD effects. The methodology for analyzing weak FD effects should allow these effects to be distinguished, even if the magnitude of the TD effects is greater. For example, this can be achieved by subtracting two system states. In state 1, the body is rotating; in state 2, the body is at rest while the source of the incident waves rotates around it. In state 1, the

system exhibits both weak bianisotropy effects and TD effects, whereas in state 2, only the latter are present. Thus, the requirement for the scatterer's boundaries to remain stationary and for the absence of time dependence of the velocity vector field, as indicated in the Section 1.1, can be significantly weakened or even completely removed.

Task MG4. Investigation of the influence of various methods for selecting the coordinates of points within Ω_s for field evaluation, which are subsequently used to compute the equivalent sources. Optimization of the strategy for choosing these point coordinates. Additionally, study of the impact of different interpolation methods of equivalent sources on the accuracy of results in COMSOL. The justification for this task is provided in Sections 2.3 and 3.3.

The second area of development is Validity Enhancement (VE). The aim of this work direction is to enhance both the internal and external validity of the BA methodology and its implementation in COMSOL, but primarily, of course, the experimental investigation. The following tasks are identified within this scope.

Task VE1. Complete the verification of the methodology for the three-dimensional problem in the native solver. Perform the corresponding verification in COMSOL.

Task VE2. Using the methodology implemented in COSMOL to validate the results of the experiments described in Section 5.2.

Task VE3. As part of the computational study, determine the potential impact of deformation and friction effects in the experimental setups described in Section 5.2. The possibility of performing multiphysical and multiscale modeling was considered, in particular, in Section 3.4. The creation of a digital twin of the experimental setup (a similar process is described in [104]) will help complete the process of excluding accompanying effects discussed in Section 5.4.

The third work package is Experimental Studies (ES). Building on the research already conducted, we will continue to optimize the experimental setup and design new ones. The main outcome of this direction may include specific recommendations for the development of new types of sensors for detecting motion effects and devices based on these principles. The list of tasks is presented below.

Task ES1. The optimization of waveguide cross-sections for TL used in experiment setup. As noted in [87], a circular waveguide can be used as the TL. At the

same time, as also mentioned in Section 5.1, a waveguide with a complex cross-sectional shape may increase measurement sensitivity due to the redistribution of the electromagnetic power within its cavity.

Task ES2. Conducting experiments in which a gas is used as the moving medium. The reasons for the necessity of this study are provided at the beginning of Chapter 5. The development of a new experimental procedure, as well as a new experimental setup, is an essential part of this task. However, the results of this experiment can be verified without any additional modifications to the approach for analyzing motion effects.

Task ES3. Optimization of thermal stabilization method of the moving medium within the observation area, aimed at minimizing the influence of temperature variations. Together with passive thermal control methods, it is necessary to apply active thermal control [105, 106].

Task ES4. The use of the BA methodology application in COMSOL for optimizing the experimental setup, the incorporation of realistic transmitter and receiver models, and the solution of the inverse problem to reconstruct the flow velocity profile. This task is defined as one of the objectives of the adaptation of the methodology in COMSOL, with several of its aspects outlined in Section 3.4.

Task ES5. The design and implementation of experimental studies, the schemes of which are shown in Figure 6.1. This represents one of the main conclusions of work [80]. The figure integrates the classical antenna-based scheme used for material testing [107]. A moving medium can be investigated using receiving and transmitting antennas, as illustrated in [69, fig. 1]. Antenna methods hold significant potential for developing new approaches in flowmetry, including those derived from the Fizeau-Fresnel scheme. The figure also shows a combined scheme. In the waveguide resonator, a slot is cut, which is weakly radiating when the media is at rest. When the media is in motion, due to the gyrotropic effect [108], the slot's radiation increases, which is detected by the receiving antenna. As described in [90], on a similar scheme, the effects of artificial bianisotropy of functional materials can be measured.

Within each individual list, the tasks are arranged in order of priority. Nevertheless, several tasks overlap; the completion of some tasks depends on the results obtained from

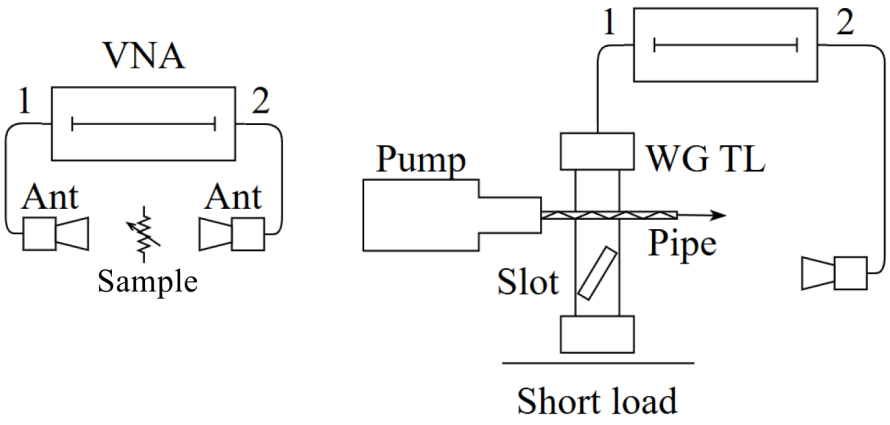

Figure 6.1: Priority schemes of experimental setups. On the left – measurement of media motion effects using the antenna method in free space. On the right – a combined antenna–TL scheme for conducting the experiment.

others (inputs), and different tasks vary in their level of complexity. Complexity is assessed based on the availability of a known approach to solving the task, the potential time required for its completion, and the resources needed to accomplish it. To create a concise plan for the upcoming research, all this information is summarized in Table 6.1.

Table 6.1: Prioritisation for future research.

Priority	Item	Inputs	Complexity
1	MG1		Average
2	VE1	MG1	Low
3	MG2		Average
4	VE2	MG2	Low
5	MG3	VE1	Average
6	VE3	VE2	Average
7	MG4		Low
8	ES1		Average
9	ES2		High
10	ES3	VE3	Average
11	ES4	MG4, VE1, VE2, VE3	High
12	ES5	MG1, MG3, ES1, ES3, ES4	High

Thus, our primary priority is the completion of the methodology verification stage and its application in COMSOL. Next, we plan to implement tasks related to the generalization of the methodology, its optimization, and the expansion of its applicability. Further experimental studies will follow. It is important to note that the completion of the latest

task currently set requires not only substantial financial support but also the successful accomplishment of almost all preceding tasks.

In this regard, the present work stands as a major and self-contained part of a larger scientific endeavor. The development of a new methodology based on the Born approximation has given rise to a new direction of research that significantly expands both the practical and theoretical foundations for studying media motion effects. The large number of tasks for further development only underscores the relevance and significance of the conducted research.

Appendix

APPENDIX A

Native FE Solver with External Meshing

To enable the creation and use of high-quality meshes of complex objects in native simulation calculations, as well as the analysis and visualization of their components, an export/import system was developed. Mesh export to the native solver format is performed from the internal COMSOL mesh description format (*.mphtxt*). Import from the native format is supported into the Standard Tessellation Language (STL) format (*.stl*), which can then be visualized and analyzed in any compatible system, including COMSOL itself.

The workflow proceeds as follows. In COMSOL, the parametric geometry of the model is created, the required computational mesh is generated, and then the mesh is exported in the intrinsic text format. It is important to note that, for the converter to function correctly, only data corresponding to domain elements (tetrahedra) and surface elements (triangles) should be exported. The exported file is parsed by a simple code according to the native mesh representation format. At the input stage, the program requests the path to the **.mphtxt* file. As output, it generates three files: the coordinates of the vertices, the vertex indices of the boundary elements, and the vertex indices of the tetrahedra. These resulting files can then be imported into the native solver for further computation. Thus, the computational mesh can be considered as imported from COMSOL.

To verify the operation of the converter, we use a previously developed program that converts mesh data from the native format to the STL format. An STL file is generated directly from the converted data, without any additional processing. This STL file is then imported back into COMSOL and compared with the originally created mesh. Since the native solver does not include tools for displaying or viewing mesh geometry, the converter that transforms the native mesh into a standardized format makes it possible to visualize the model geometry in any viewer that supports STL format.

Figure A.1 shows examples used to verify the operation of the developed converter for COMSOL–native format–STL transformations. Computational meshes for the following geometries were used: cube, cylinder, unified geometry, geometry with subtraction, and

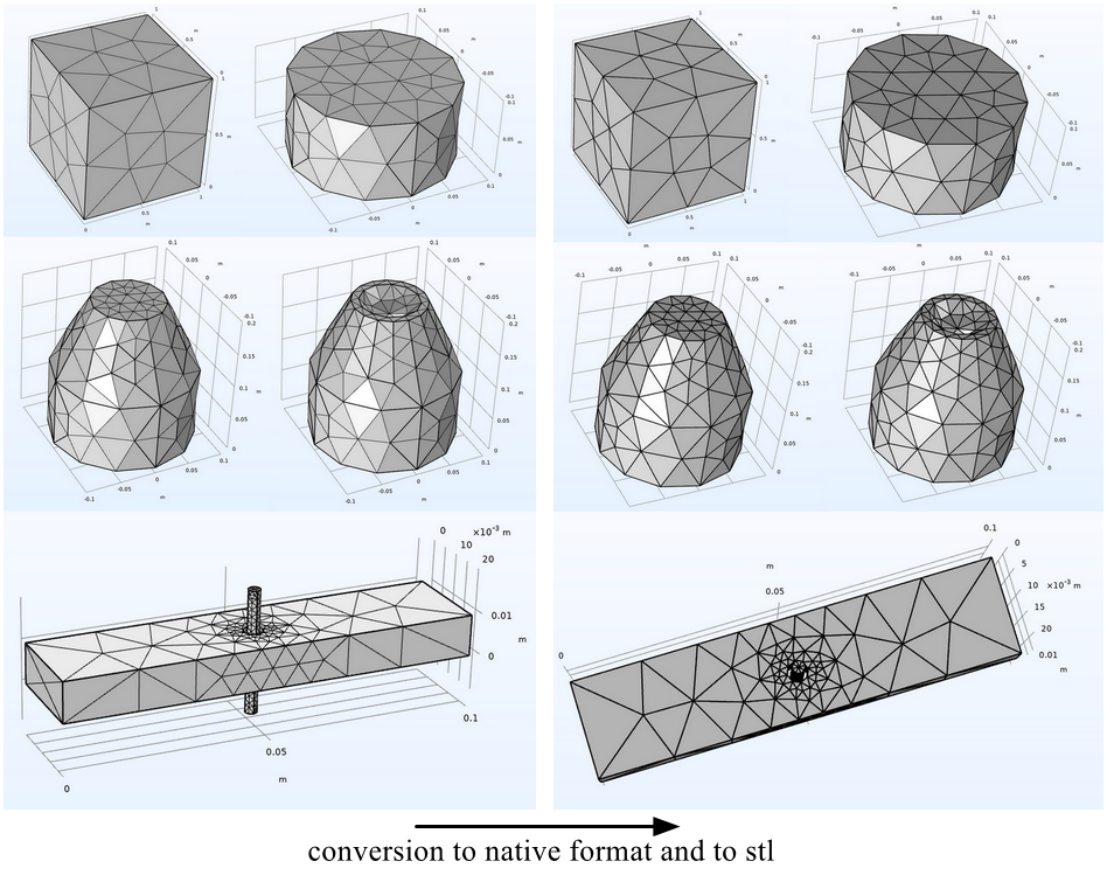

Figure A.1: Verification of the mesh import/export system for various geometries. On the left – meshes exported from COMSOL for conversion to the native solver format. On the right – meshes imported back into COMSOL after conversion to the native solver format and subsequent export to STL.

waveguide geometry. The meshes were first exported to the *.mphtxt* format, then converted to the native FE solver format, and subsequently converted to the STL format and imported back into COMSOL. Analysis of the meshes using standard COMSOL tools confirmed that they are identical and that the conversion process does not alter them.

For the native solver to operate correctly, it is crucial to create an appropriate geometry in COMSOL. This geometry must account for the specific features of the solver, only some of them are domain decomposition method, element enumeration, specifics of mesh geometry reading, *etc*. We will not go into detail here, but it should be noted that the geometry must be defined in accordance with these rules. Otherwise, the computation may either be inefficient in terms of computational resources (primarily due to the element numbering order) or even incorrect (if the domains in the geometry are improperly defined).

We analyzed the use of a mesh converted from COMSOL to the native format. Verification of the native solver's performance with the imported mesh was carried out using the same problem that was employed to validate the new BA methodology in 3D (see Figure 4.1, Table 4.1 and problem description in Section 4.2.2.1).

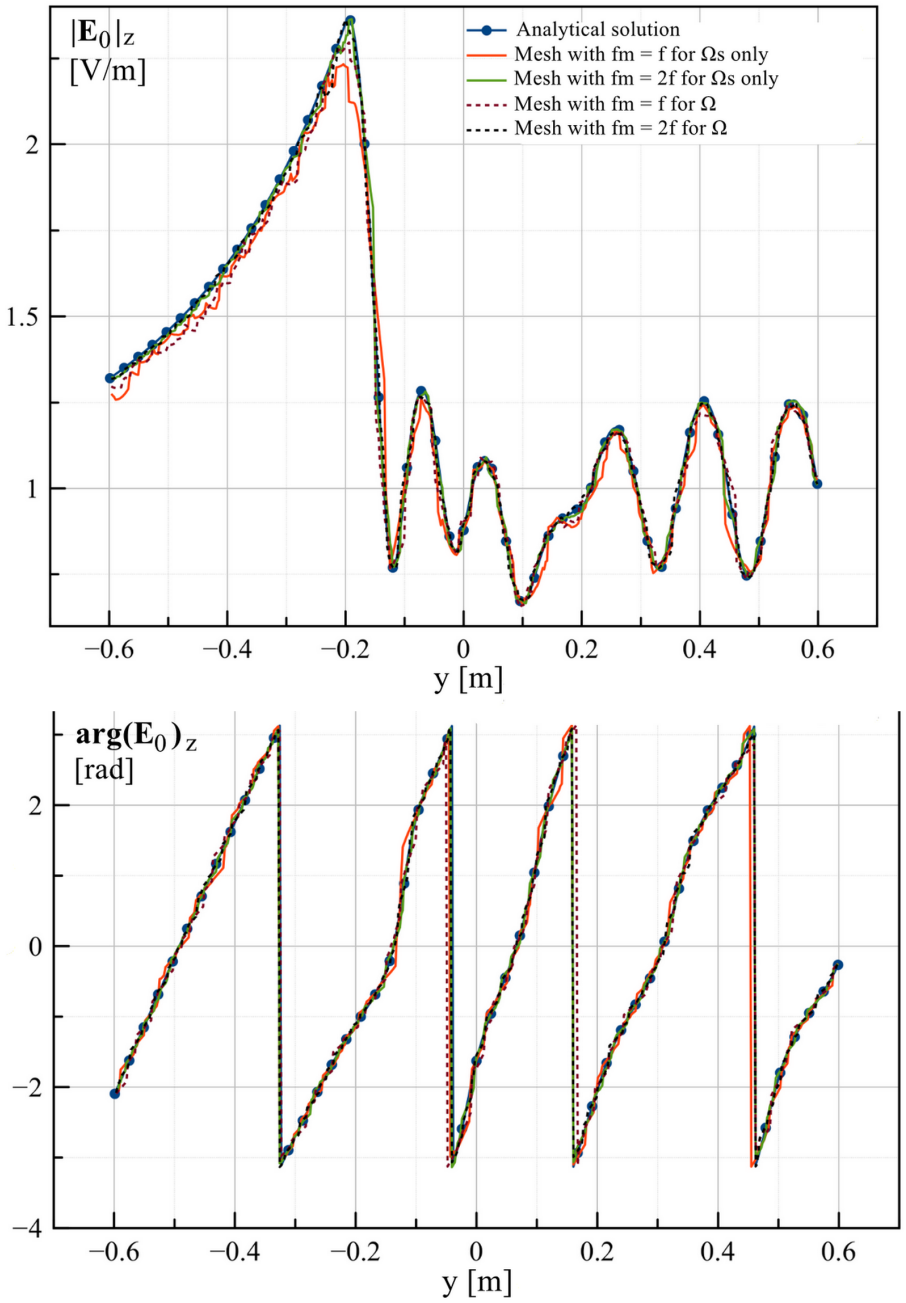

Figure A.2: Verification of the mesh imported into the native solver by solving the scattering problem.

Figure A.2 shows the results of comparing the calculation of the native solver with the imported mesh to the analytical solution. It can be noted that the plot for the $|\mathbf{E}_0|_z$ corresponds to the results obtained earlier (see Figure 4.7 at the bottom). We examined four different meshes created in COMSOL. The parameter f_m is the reference frequency used for mesh generation in COMSOL. It was introduced, in particular, during the verification of the methodology implementation in Section 4.3. We also tested different meshing rules for the system's domains (see Figure 2.1). In some cases, we controlled the mesh only for the subregion of the scatterer, while the surrounding domain was meshed with a standard coarse mesh. However, in this case, the mesh was refined near the scatterer's boundary. In other cases, the mesh was applied to the entire computational domain, without defining a separate subregion for the scatterer, resulting in a quasi-uniform mesh throughout the volume. The results clearly demonstrate two well-known facts [34, 59]: first, with a controlled increase in the number of elements (*i.e.*, as the parameter f_m increases), the solution converges to the exact result; second, uniform meshes generally provide more accurate results, although in many cases they are not optimal in terms of the required computational resources.

Next, we present the use of an imported mesh of a complex geometry, which cannot be created using the native solver alone, for the analysis of a problem of particular interest. As noted in Section 5.2, numerical analysis of the geometry corresponding to that described by Nishikata [97] can provide valuable data for optimizing and designing the experiment. The study of such a problem in one of the commercial CAD systems is presented in [109]. We also considered a similar problem in COMSOL [104].

In Figure A.3, the parametric geometry of the problem, created in COMSOL, is shown at the top. At the bottom, the mesh imported into the native solver is visualized. A three-dimensional cavity problem has been formulated. In this case, we can avoid the issues related to applying BCs on the top and bottom faces of the cylinder, which we encountered when solving the open three-dimensional problem (see Section 4.2.2.3). This is because all the electromagnetic power is concentrated inside the waveguide cavity and does not reach the boundaries of the cylinder's end faces. However, to minimize their potential influence, we can place them in the lateral regions, which are semi-spherical radiation domains with boundaries similar to Sommerfeld surfaces [59, chap. 9] (see also [110]).

It should be noted that when constructing the parametric geometry, the subregion of the cylinder inside the waveguide was not defined as a separate geometric entity. Thus, the portion of the pipe located inside the cavity is not visually distinguishable, including in the mesh geometry. This was done deliberately and is related to the features of the

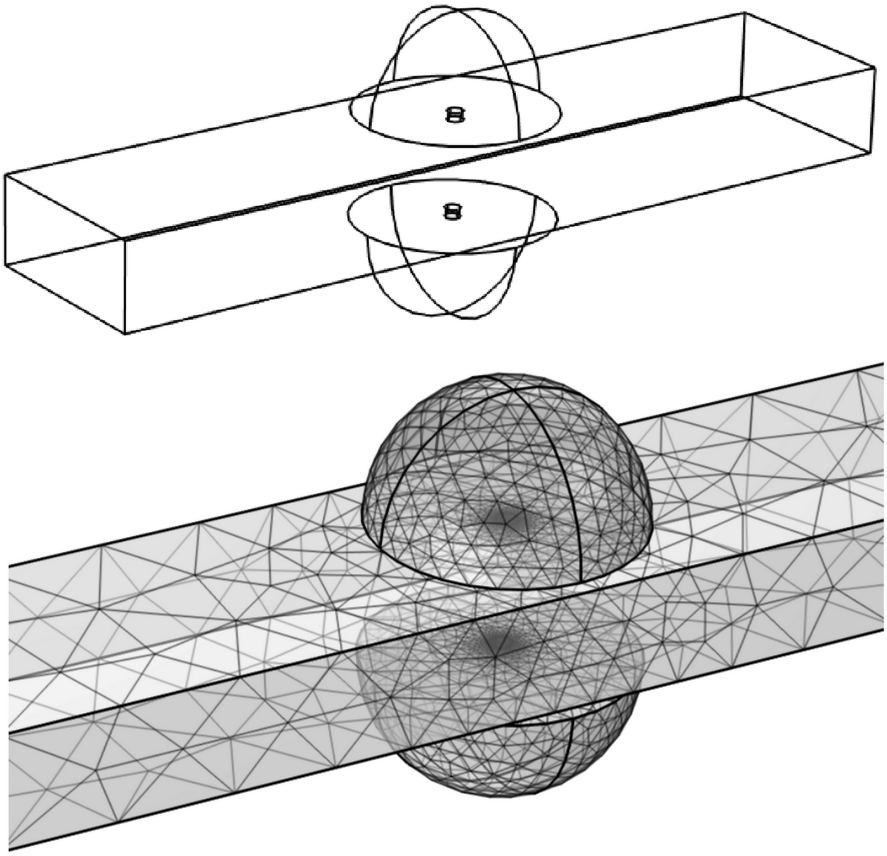

Figure A.3: Parametric geometry (top) and computational mesh (bottom) for a pipe piercing a rectangular waveguide along its narrow wall. Only the surface triangular mesh is shown.

native solver's operation, which we mentioned above. To avoid local mesh refinement, we construct a uniform high-precision mesh throughout the entire waveguide cavity, and then assign the required material parameters to the elements $\in \Omega_s$.

We used the model shown in the Figure A.3 to calculate the S_{11} and S_{21} parameters in the native solver (the formulation of the cavity problem for bianisotropic material is given in [77]). Using this model, we can calculate the motion effects both with the traditional FE difference method and with the new BA methodology. In this section, we do not present the results of these computations; however, they clearly demonstrated the necessity of implementing the BA methodology in COMSOL. First, the accuracy of the native FE approximation did not allow the computational noise level to be reduced sufficiently to detect the motion effect at the order of $\beta \approx 10^{-8}$. Second, the computation time for fine meshes can be up to seven times higher than that for the same model on an

identical mesh in COMSOL. Overall, this was expected. The native solver is a powerful tool for verification, but not for high-performance or optimized computations. It should be emphasized that the creation of a mesh export/import system from the commercial CAD significantly enhanced this tool, expanded its range of applicability, and improved the user experience and ease of mesh analysis.

Acknowledgements

I would like to express my deepest gratitude to my supervisor, **Prof. Mirco Raffetto**, for his invaluable guidance, insightful discussions, and continuous support throughout my research. His exceptional expertise, scientific creativity, and constant responsiveness have been essential to my work on a project that has been ongoing for more than ten years.

I am deeply thankful to **Dr. Mario Rene Clemente Vargas**, a former PhD student of Prof. Raffetto, for his generosity, readiness to help, and many stimulating and productive discussions. He also provided substantial assistance in developing the procedure described in Appendix A.

My sincere appreciation goes to **Prof. Yuri Feldman** from the Hebrew University of Jerusalem for his valuable comments and discussions on the interaction of electromagnetic radiation with water. His expertise and insights into the nature and mechanisms of electrical conductivity in water form a solid foundation for future research.

I wish to extend my heartfelt thanks to **Prof. Sergey Knyazev** from the Ural Federal University. Under his supervision, my first dissertation on a related topic was successfully completed, which greatly strengthened my confidence and academic independence.

I am also grateful to **Prof. Sergey Shabunin** from the Ural Federal University. Thanks to him, I was introduced to Prof. Mirco Raffetto, making this entire journey possible.

Special thanks are due to **Dr. Nikolay Knyazev** from the Ural Federal University. With his permission and support, the first series of experiments described in Chapter 5 was conducted in his laboratory.

I also wish to thank **Dr. Mikhail Ronkin** from the Ural Federal University for his expertise in flow measurements, hydrodynamics, and signal processing. His guidance and technical support were invaluable during all experimental stages, and he took an active part in the first experimental series.

My warmest thanks go to my parents and sister for their endless encouragement and unwavering support throughout my studies.

Finally, my deepest gratitude goes to my wife, **Galina**. Without her patience, understanding, and constant presence by my side, none of this would have been possible.

Academic Activities

Publication record

1. International Journal Papers

M. Raffetto, M. R. Clemente Vargas, and K. Zeyde, "A new Born-approximation approach to compute the effects of motion on the solution of electromagnetic problems involving moving materials with stationary boundaries," *IET Science, Measurement & Technology*, vol. 18, no. 5, p. 245–257, 2024.

K. Zeyde and M. Raffetto, "Application of the Born Approximation for Modeling EM Effects of Moving Materials in COMSOL Multiphysics," accepted for publication in *IEEE Journal on Multiscale and Multiphysics Computational Techniques*, 2026.

2. International Conference Papers

K. Zeyde, "Multiscale effects of continuous moving medium for the weak bianisotropy detection," in *IEEE International Conference on Microwaves, Communications, Antennas, Biomedical Engineering and Electronic Systems (COMCAS)*, Tel-Aviv, Israel, 2024.

M. Raffetto and K. Zeyde, "First 3D results obtained by a new Born-Approximation methodology for media in motion with stationary boundaries," in *IEEE International Symposium on Antennas and Propagation and INC/USNC-URSI Radio Science Meeting (AP-S/INC-USNC-URSI)*, Firenze, Italy, 2024, p. 1339–1340.

K. Zeyde, "Experiments confirming the capabilities of novel microwave Fizeau-Fresnel flowmeters," in *6th International Conference in Electronic Engineering & Information Technology (EEITE)*, Chania, Greece, 2025.

K. Zeyde and M. Raffetto, "Innovative application of the Born-approximation for analyzing medium motion effects in COMSOL time explicit EMW module," in *URSI International Symposium on Electromagnetic Theory (EMTS)*, Bologna, Italy, 2025.

R. Onesti, M. Raffetto, and K. Zeyde, "Analytical evaluation of the effects on the electromagnetic field induced by a moving dielectric slab," in *URSI International Symposium on Electromagnetic Theory (EMTS)*, Bologna, Italy, 2025.

3. National Conference

K. Zeyde and M. Raffetto, "Finite-element Born Approximations of the EM field scattered by moving media with stationary boundaries," in *XXV Riunione Nazionale di Elettromagnetismo (RINEM)*, Viareggio, Italy, 2024.

Participation in Research Projects

Research project Marine Terrestrial 5G Communications for Autonomous Drones (MTCOM).

The MTCOM project aims to develop and test a control and positioning system for autonomous vessels in the port of the future. These vessels will be equipped with radio links to enable autonomous navigation and will be coordinated via a private 5G network for port operation management and the mitigation of marine pollution. Evaluating the performance of the radio links in this environment requires studies that account for the time-varying nature of the channel, caused by sea surface reflections and continuous changes in the orientation of the antennas mounted on the drones. Additionally, it is necessary to assess the effectiveness of commercially available electromagnetic simulators to select appropriate antennas and optimize the performance of the drone communication systems.

Activity:

1. Altair WinProp was proposed for solving the project tasks, and its effectiveness was proven.

2. A literature review was carried out, providing the state of the art on the subject under study.

3. For the verification of numerical algorithms, an analytical trivial two- ray signal propagation channel model was developed.

a series of computational studies were conducted in WinProp, including a pilot study for the simplest two-ray model with reflection from a perfectly smooth surface, as well as a study of diffuse scattering from a rough sea surface.

4. A software code was developed for the topographic determination of the actual sea surface profile, for its export to WinProp.

5. A simple statistical model of diffuse scattering from a rough sea surface was developed to assess the communication channel budget.

Other activities

Reviewing activity for the following international journals:

Frontiers in Earth Science

Ural Radio Engineering Journal

IEEE Transactions on Geoscience and Remote Sensing

IEEE Transactions on Antennas and Propagation

Bibliography

[1] M. H. Fizeau, "On the effect of the motion of a body upon the velocity with which it is traversed by light," *Philosophical magazine and journal of science*, vol. 19, no. 127, 1860.

[2] J. Van Bladel, *Relativity and engineering*, ser. Springer Series in Electrophysics. Berlin: Springer-Verlag, 1984, vol. 15.

[3] R. C. Baker, *Flow measurement handbook*. New York: Cambridge University Press, 2000.

[4] O. Frazão, P. Caldas, F. M. Araújo, L. A. Ferreira, and J. L. Santos, "Optical flowmeter using a modal interferometer based on a single nonadiabatic fiber taper," *Optics letters*, vol. 32, no. 14, pp. 1974–1976, 2007.

[5] R. Mathevet, P. Labastie, and T. Lahaye, "Fizeau's 'aether-drag' experiment in the undergraduate laboratory," in *Procedings Education and Training in Optics and Photonics*, Bordeaux, France, 2015.

[6] Y. Ben-Shimol and D. Censor, "Wave propagation in moving chiral media: Fizeau's experiment revisited," *Radio Science*, vol. 30, no. 5, pp. 1313–1324, 1995.

[7] M. V. Ronkin, A. A. Kalmykov, and K. M. Zeyde, "Novel FMCW-interferometry method testing on an ultrasonic clamp-on flowmeter," *IEEE Sensors journal*, vol. 20, no. 11, p. 6029–6037, 2020.

[8] A. Einstein, "Zur elektrodynamik bewegter korper," *Annalen der physik und chemie*, vol. 17, pp. 891–921, 1905.

[9] H. Minkowski, "Die grundgleichungen fur die elektromagnetischen vorgange in bewegten korpern," *Nachrichten von der gesellschaft der wissenschaften*, p. 53–111, 1908.

[10] D. K. Cheng and J. A. Kong, "Covariant descriptions of bianisotropic media," *Proceedings of the IEEE*, vol. 56, no. 3, p. 248–251, 1968.

[11] B. D. H. Tellegen, "The gyrator, a new electric network element," *Philips Research Reports*, vol. 3, no. 2, pp. 81–101, 1948.

[12] A. Q. Howard, W. C. Chew, and M. C. Moldoveanu, "A new correction to the Born approximation," *IEEE Transactions on geoscience and remote sensing*, vol. 28, no. 3, p. 394–399, 1990.

[13] D. L. Alumbaugh and H. F. Morrison, "Electromagnetic conductivity imaging with an iterative Born inversion," *IEEE Transactions on geoscience and remote sensing*, vol. 31, no. 4, p. 758–763, 1993.

[14] P. R. Siqueira, K. Sarabandi, and F. T. Ulaby, "Numerical simulation of scatterer positions in a very dense medium with an application to the two-dimensional Born approximation," *Radio Science*, vol. 30, no. 5, pp. 1325–1339, 1995.

[15] O. Hrevtsev, N. Selivanova, P. Popovych, L. Poberezhny, O. Shevchuk, G. Hrytsuliak, and L. Poberezhna, "The movement investigation of an axisymmetric rotation body under the action of electromagnetic fields," *Journal of Achievements in Materials and Manufacturing Engineering*, vol. 103, no. 2, p. 67–77, 2020.

[16] Z. Deck-Léger, X. Zheng, and C. Caloz, "Electromagnetic wave scattering from a moving medium with stationary interface across the interluminal regime," *Photonics*, vol. 8, no. 202, 2021.

[17] X.-M. Guo, H.-Y. Li, Y. Bo, W. Chen, L.-X. Yang, Z.-X. Huang, and A.-Q. Wang, "Analysis of EM properties of high-speed moving cone-sphere target coated with plasma sheath based on Lorentz-FDTD method," *Applied Computational Electromagnetics Society Journal*, vol. 39, no. 2, pp. 156–168, 2024.

[18] N. N. Grinchik and O. V. Boiprav, "High-frequency electrodynamics of slow-moving limited media taking into account the additional specular reflection," *Advanced electromagnetics*, vol. 10, no. 1, p. 6–14, 2021.

[19] S. Vujević, "Maxwell's and wave equations in media containing electromagnetic field sources," *International Journal for Engineering Modelling*, vol. 38, no. 2, pp. 1–9, 2025.

[20] M. T. Peric, S. S. Ilic, A. N. Vuckovic, and N. B. Raicevic, "Analysis of bi-isotropic media using hybrid boundary element method," *Applied Computational Electromagnetics Society Journal*, vol. 36, no. 10, p. 1265–1273, 2021.

[21] M. Rafaei-Booket and M. Bozorgi, "Spectral dyadic Green's function for multilayer periodic bi-anisotropic media," *IEEE Access*, vol. 10, p. 116261–116272, 2022.

[22] M. Marvasti and H. Boutayeb, "Analysis of moving bodies with a direct finite difference time domain method," *Applied Computational Electromagnetics Society Journal*, vol. 38, no. 11, p. 829–840, 2023.

[23] G. Jandieri, A. Ishimaru, B. Rawat, and N. Tugushi, "Temporal spectrum of a scattered electromagnetic waves in the conductive collision turbulent magnetized plasma," *Advanced electromagnetics*, vol. 11, no. 1, p. 1–8, 2022.

[24] C. Mystilidis, G. Fikioris, C. Tserkezis, G. A. E. Vandenbosch, and X. Zheng, "The uniqueness theorem for nonlocal hydrodynamic media," *IEEE Transactions on antennas and propagation*, vol. 72, no. 12, p. 9259–9273, 2024.

[25] L. Wang, C. Liao, R. Yuan, J. Gao, and D. Ding, "Transient simulation of electromagnetic wave propagation in plasma based on dynamic Drude model," *IEEE Transactions on antennas and propagation*, vol. 72, no. 1, p. 767–778, 2024.

[26] H. Lopez-Menchon, J. M. Rius, A. Heldring, and E. Ubeda, "Acceleration of Born series by change of variables," *IEEE Transactions on antennas and propagation*, vol. 69, no. 9, p. 5750–5760, 2021.

[27] T. Shan, Z. Lin, X. Song, M. Li, F. Yang, and S. Xu, "Neural Born iterative method for solving inverse scattering problems: 2D cases," *IEEE Transactions on antennas and propagation*, vol. 71, no. 1, p. 818–829, 2023.

[28] L. Ahmadi and A. A. Shishegar, "A physics-based deep learning to extend Born approximation validity to strong scatterers," *IEEE Transactions on antennas and propagation*, vol. 72, no. 12, p. 9392–9400, 2024.

[29] J. Van Bladel, *Electromagnetic fields*, 2nd ed., ser. Series on Electromagnetic wave theory. USA: The IEEE Press, 2007.

[30] P. K. Ramakrishnan and M. Raffetto, "Well posedness and finite element approximability of three-dimensional time-harmonic electromagnetic problems involving rotating axisymmetric objects," *Symmetry*, vol. 12, no. 2, 2020.

[31] N. Zettili, *Quantum mechanics: concepts and applications*, 2nd ed. Chichester, U.K: Wiley, 2009.

[32] L. Tsang, J. A. Kong, and K.-H. Ding, *Scattering of Electromagnetic Waves: Theories and Applications*, ser. Remote sensing. USA: Wiley, 2000.

[33] P. Beckmann, "Equivalent electromagnetic constants of moving media," *Proceedings of the IEEE*, vol. 58, no. 5, pp. 800–801, 1970.

[34] R. W. Thatcher, "Assessing the error in a finite element solution," *IEEE Transactions on microwave theory and techniques*, vol. MTT-30, no. 6, p. 911–915, 1982.

[35] D. D. Zutter, "Scattering by a rotating dielectric sphere," *IEEE Transactions on antennas and propagation*, vol. AP-28, no. 5, pp. 643–651, 1980.

[36] ——, "Scattering by a rotating circular cylinder with finite conductivity," *IEEE Transactions on antennas and propagation*, vol. AP-31, no. 1, pp. 166–169, 1983.

[37] J. V. Bladel, "Relativistic theory of rotating disks," *Proceedings of the IEEE*, vol. 61, no. 3, pp. 260–268, 1973.

[38] D. Censor, "Scattering of electromagnetic waves by a cylinder moving along its axis," *IEEE Transactions on microwave theory and techniques*, vol. MTT-17, no. 3, pp. 154–158, 1969.

[39] C. Yeh, "Scattering obliquely incident microwaves by a moving plasma column," *Journal of Applied Physics*, vol. 40, no. 13, p. 5066–5075, 1969.

[40] V. P. Pyati, "Reflection and refraction of electromagnetic waves by a moving dielectric medium," *Journal of Applied Physics*, vol. 38, no. 2, p. 652–655, 1967.

[41] J. Ramasastry and G. Y. Chin, "Wave interaction with moving boundaries," *Electronics letters*, vol. 3, no. 11, pp. 479–481, 1967.

[42] R. Onesti, M. Raffetto, and K. Zeyde, "Analytical evaluation of the effects on the electromagnetic field induced by a moving dielectric slab," in *URSI International Symposium on Electromagnetic Theory (EMTS)*, Bologna, Italy, 2025.

[43] M. Pastorino and M. Raffetto, "Scattering of electromagnetic waves from a multilayer elliptic cylinder moving in the axial direction," *IEEE Transactions on antennas and propagation*, vol. 61, no. 9, pp. 4741–4753, 2013.

[44] ——, "Scattering of electromagnetic waves by a rotating perfectly conducting cylinder with arbitrary cross section: point-matching method," *IEEE Transactions on antennas and propagation*, vol. AP-28, no. 6, pp. 796–803, 1980.

[45] S. Sahrani, H. Iwamatsu, and M. Kuroda, "A novel approach for the analysis of electromagnetic field with rotating body," *Applied Computational Electromagnetics Society Journal*, vol. 26, no. 8, pp. 651–659, 2011.

[46] T. Danov and T. Melamed, "A simple and direct time domain derivation of the dyadic Green's function for a uniformly moving non-dispersive dielectric-magnetic medium," *IEEE Transactions on antennas and propagation*, vol. 60, no. 5, p. 2594–2597, 2012.

[47] A. Freni, C. Mias, and R. Ferrari, "Finite element analysis of electromagnetic wave scattering by a cylinder moving along its axis surrounded by a longitudinal corrugated structure," *IEEE Transactions on magnetics*, vol. 32, no. 3, pp. 874–877, 1996.

[48] K. M. Zeyde, "Fast segmentation of a rotating axisymmetric scatterer medium of an arbitrary form for the first order fields numerical analysis," *Ural radio engineering journal*, vol. 2, no. 2, pp. 26–39, 2018.

[49] P. Kalarickel Ramakrishnan, M. R. Clemente Vargas, and M. Raffetto, "Electromagnetic inverse scattering of rotating axisymmetric objects," *IEEE Access*, vol. 9, pp. 168185–168192, 2021.

[50] M. Brignone, G. L. Gragnani, M. Pastorino, M. Raffetto, and A. Randazzo, "Noise limitation on the recovery of average values of velocity profiles in pipelines by simple imaging systems," *IEEE Geosciense and remote sensing letters*, vol. 13, no. 9, pp. 1340–1344, 2016.

[51] M. Pastorino, M. Raffetto, and A. Randazzo, "Electromagnetic inverse scattering of axially moving cylindrical targets," *IEEE Transactions on geoscience and remote sensing*, vol. 53, no. 3, pp. 1452–1462, 2015.

[52] H. Alfven, *Cosmical electrodynamics*. Oxford: Clarendon press, 1950.

[53] K. M. Zeyde, "An effects set related to the radio signal propagation in a moving reference frame," in *IEEE International Conference of Young Professionals in Electron Devices and Materials (EDM)*, Altai, Russia, 2021, p. 132–136.

[54] H. H. Bruun, *Hot-Wire Anemometry: Principles and Signal Analysis*. New York: Oxford University Press, 1995.

[55] M. Raffetto, M. R. Clemente Vargas, and K. Zeyde, "A new Born-approximation approach to compute the effects of motion on the solution of electromagnetic problems involving moving materials with stationary boundaries," *IET Science, Measurement & Technology*, vol. 18, no. 5, p. 245–257, 2024.

[56] C. A. Balanis, *Advanced Engineering Electromagnetics*. New York: Wiley, 1989.

[57] P. Fernandes and M. Raffetto, "Well posedness and finite element approximability of time-harmonic electromagnetic boundary value problems involving bianisotropic materials and metamaterials," *Mathematical Models and Methods in Applied Sciences*, vol. 19, no. 12, pp. 2299–2335, 2009.

[58] P. K. Ramakrishnan and M. Raffetto, "Accuracy of finite element approximations for two-dimensional time-harmonic electromagnetic boundary value problems involving non-conducting moving objects with stationary boundaries," *Applied Computational Electromagnetics Society Journal*, vol. 33, no. 6, pp. 585–596, 2018.

[59] P. Monk, *Finite Element Methods for Maxwell's Equations*, ser. Numerical Mathematics and Scientific Computation. Oxford: Clarendon press, 2003.

[60] K. M. Zeyde, "Augmented interpretation model of a moving media for the electrodynamic effects simulation," in *IEEE MTT-S International Conference on Numerical Electromagnetic and Multiphysics Modeling and Optimization (NEMO)*, Reykjavik, Iceland, 2018.

[61] J. V. Bladel, "Electromagnetic fields in the presence of rotating bodies," *Proceedings of the IEEE*, vol. 64, no. 3, pp. 301–318, 1976.

[62] P. Ylä-Oijala, J. Markkanen, and S. Järvenpää, "Current-based volume integral equation formulation for bianisotropic materials," *IEEE Transactions on antennas and propagation*, vol. 64, no. 8, p. 3470–3477, 2016.

[63] K. Zeyde and M. Raffetto, "Innovative application of the Born-approximation for analyzing medium motion effects in COMSOL time explicit EMW module," in *URSI International Symposium on Electromagnetic Theory (EMTS)*, Bologna, Italy, 2025.

[64] *COMSOL Multiphysics® RF Module User's Guide*, COMSOL, 2024, version 6.2. [Online]. Available: https://www.comsol.com

[65] *COMSOL Multiphysics® Reference Manual*, COMSOL, 2023, version 6.2. [Online]. Available: https://www.comsol.com

[66] G. H. C. Silva, R. L. Riche, J. Molimard, and A. Vautrin, "Exact and efficient interpolation using finite elements shape functions," *European Journal of Computational Mechanics*, vol. 18/3–4, p. 307–331, 2009.

[67] W. Luo, J. Liu, Z. Li, and J. Song, "Efficient triangular interpolation methods: Error analysis and applications," *IEEE Antennas and Wireless Propagation Letters*, vol. 19, no. 6, p. 1032–1036, 2020.

[68] J. Nocedal and S. J. Wright, *Numerical Optimization*, 2nd ed., ser. Operations Research. Springer, 2006.

[69] K. M. Zeyde, "Multi-factor nonlinear optimization of nonrelativistic experiment on electromagnetic scattering by rotating target," *Nonlinear World*, vol. 15, no. 5, pp. 11–17, 2017.

[70] T. Shiozawa, "Phenomenological and electron-theoretical study of the electrodynamics of rotating systems," *Proceedings of the IEEE*, vol. 61, no. 12, pp. 1694–1702, 1973.

[71] S. Seikai and T. Shiozawa, "Scattering of electromagnetic waves by a rotating electron-plasma column," *IEEE Transactions on antennas and propagation*, vol. AP-23, no. 1, pp. 75–83, 1975.

[72] K. M. Zeyde, "The motion of electrons under the action of inertial forces in the rarefied medium," in *3rd URSI Atlantic and Asia Pacific Radio Science Meeting (AT-AP-RASC)*, Gran Canaria, Spain, 2022.

[73] M. Raffetto and K. Zeyde, "First 3D results obtained by a new Born-Approximation methodology for media in motion with stationary boundaries," in *IEEE International Symposium on Antennas and Propagation and INC/USNC-URSI Radio Science Meeting (AP-S/INC-USNC-URSI)*, Firenze, Italy, 2024, p. 1339–1340.

[74] Y. Fan, J. Luo, W. Xie, R. Lan, and W. Li, "High-frequency characteristics of the axisymmetric TM modes in a coaxial staggered double-grating slow-wave structure," *IEEE transactions on electron devices*, vol. 63, no. 5, pp. 2110–2117, 2016.

[75] M. Brignone and M. Raffetto, "Well posedness and finite element approximability of two-dimensional time-harmonic electromagnetic problems involving non-conducting moving objects with stationary boundaries," *ESAIM: Math. Model. Numer. Anal.*, vol. 49, no. 4, p. 1157–1192, 2015.

[76] G. Cevini, G. Oliveri, and M. Raffetto, "Further comments on the performances of finite element simulators for the solution of electromagnetic problems involving metamaterials," *Microwave and optical technology letters*, vol. 48, no. 12, p. 2524–2529, 2006.

[77] P. K. Ramakrishnan and M. Raffetto, "Three-dimensional time-harmonic electromagnetic scattering problems from bianisotropic materials and metamaterials: Reference solutions provided by converging finite element approximation," *Electronics*, vol. 9, no. 7, 2020.

[78] J. D. Jackson, *Classical electrodynamics*, 3rd ed. New York: Wiley, 1999.

[79] K. Zeyde, "Multiscale effects of continuous moving medium for the weak bianisotropy detection," in *IEEE International Conference on Microwaves, Communications, Antennas, Biomedical Engineering and Electronic Systems (COMCAS)*, Tel-Aviv, Israel, 2024.

[80] ——, "Experiments confirming the capabilities of novel microwave Fizeau-Fresnel flowmeters," in *6th International Conference in Electronic Engineering & Information Technology (EEITE)*, Chania, Greece, 2025.

[81] E. Seran, M. Godefroy, E. Pili, N. Michielsen, and S. Bondiguel, "What we can learn from measurements of air electric conductivity in 222rn-rich atmosphere," *Earth and Space Science*, no. 4, p. 91–106, 2017.

[82] N. Marcuvitz, *Waveguide handbook*. London: IET, 1986.

[83] K. M. Zeyde, "Resonant cavity second order perturbation by moving medium with stationary domain," in *IEEE International Conference of Young Professionals in Electron Devices and Materials (EDM)*, Altai, Russia, 2021, p. 132–136.

[84] J. Ju, "A novel configuration of temperature compensation in the resonant cavities," *IEEE Transactions on microwave theory and techniques*, vol. 52, no. 1, pp. 139–143, 2004.

[85] C. K. Kim, L. Minz, and S. O. Park, "Improved measurement method of material properties using continuous cavity perturbation without relocation," *IEEE Transactions on instrumentation and measurement*, vol. 69, no. 8, p. 5702–5716, 2020.

[86] Z. Peng, J. Y. Hwang, and M. Andriese, "Maximum sample volume for permittivity measurements by cavity perturbation technique," *IEEE Transactions on instrumentation and measurement*, vol. 63, no. 2, p. 450–455, 2014.

[87] K. M. Zeyde and V. V. Sharov, "Fluid flow sensors design based on electromagnetic drag effect," in *International Conference on Control, Artificial Intelligence, Robotics & Optimization (ICCAIRO)*, Athens, Greece, 2019, p. 48–53.

[88] J. A. Kong and D. K. Cheng, "On guided waves in moving anisotropic media," *IEEE Transactions on microwave theory and techniques*, vol. MTT-16, no. 2, pp. 99–103, 1968.

[89] K. M. Zeyde, V. V. Sharov, and M. V. Ronkin, "Guided microwaves electromagnetic drag over the sensitivity threshold experimental observation," *WSEAS Transactions on Communications*, vol. 18, p. 191–205, 2019.

[90] K. M. Zeyde, D. Hong, and Y. Zhou, "Simulation of novel method for material's weak bianisotropy detection," in *International Conference on Control Systems, Mathematical Modeling, Automation and Energy Efficiency (SUMMA)*, Lipetsk, Russia, 2021, pp. 730–733.

[91] K. M. Zeyde and I. B. Milochkin, "General algorithm for cognitive material measurements by the radio structuroscopy method," in *International Conference on Control Systems, Mathematical Modeling, Automation and Energy Efficiency (SUMMA)*, Lipetsk, Russia, 2023, p. 599–602.

[92] D. Cohen and R. Shavit, "Bi-anisotropic metamaterials effective constitutive parameters extraction using oblique incidence S-parameters method," *IEEE Transactions on antennas and propagation*, vol. 63, no. 5, p. 2071–2078, 2015.

[93] M. Hiebel, *Fundamentals of vector network analysis*, 2nd ed. Germany: Rohde and Schwarz, 2018.

[94] D. M. Pozar, *Microwave Engineering*, 4th ed. John Wiley & Sons, 2012.

[95] V. Raicu and Y. Feldman, *Dielectric Relaxation in Biological Systems*, 1st ed. Oxford: Oxford University Press, 2015.

[96] M. E. Bialkowski, "Analysis of a coaxial-to-waveguide adaptor incorporating a dielectric coated probe," *IEEE Microwave and guided wave letters*, vol. 1, no. 8, p. 211–214, 1991.

[97] A. Nishikata, "Scattering analysis for layered cylindrical object perpendicularly piercing the wider walls of a rectangular waveguide and its application to and measurement," *IEEE Transactions on microwave theory and techniques*, vol. 57, no. 6, pp. 1602–1611, 2009.

[98] R. E. Kleinman and R. B. Mack, "Scattering by linearly vibrating objects," *IEEE Transactions on antennas and propagation*, vol. AP-27, no. 3, pp. 344–352, 1979.

[99] V. C. Chen, F. Li, S. Ho, and H. Wechsler, "Micro-Doppler effect in radar: phenomenon, model and simulation study," *IEEE Transactions on aerospace and electronic systems*, vol. 42, no. 1, pp. 2–19, 2006.

[100] H. Biao, T. Rongming, W. Xuefang, and X. Hongqing, "Bubble content in air/hydro system - part 1: measurement of bubble content," *Tsinghua Science and Technology*, vol. 5, no. 1, pp. 68–71, 2000.

[101] C. Shen, T. Song, and U. Lemmin, "Skin friction measurement in variable temperature flow," in *IEEE Instrumentation and measurement technology conference*, Brussels, Belgium, 1996, p. 523–526.

[102] V. V. Varadan, Y. R. Roh, B. Shankar, and V. K. Varadan, "Measurement of the skin friction associated with turbulent flows in air and water using SAW devices," in *IEEE Symposium on Ultrasonics*, Honolulu, USA, 1990.

[103] C. Ghouila-Houri, A. Mazzamurro, T. Arnoult, M. Benedito, R. Viard, Q. Gallas, E. Garnier, A. Merlen, A. Talbi, and P. Pernod, "High temperature gradient microsensors for skin-friction measurement in flow control applications," in *Symposium*

on Design, Test, Integration & Packaging of MEMS and MOEMS, Paris, France, 2021.

[104] K. M. Zeyde and I. B. Milochkin, "Computer model development for a verified computational experiment to restore the parameters of bodies with arbitrary shape and dielectric properties," *Computer Research and Modeling*, vol. 15, no. 6, pp. 1555–1571, 2023.

[105] Z. Cheng, L. Sun, F. Liu, X. Liu, L. Li, Q. Li, and R. Hu, "Engineering design of an active–passive combined thermal control technology for an aerial optoelectronic platform," *Sensors*, vol. 19, no. 23, 2019.

[106] W. E. Johnson, K. E. Daniel, K. A. Roberts, R. G. Schunk, and J. T. Farmer, "Hybrid thermal control system for extreme thermal environments," in *52nd International Conference on Environmental Systems (ICES)*, Calgary, Canada, 2023.

[107] D. K. Chodgaonkar, V. V. Varadan, and V. K. Varadan, "A free-space method for measurement of dielectric constants and loss tangents at microwave frequencies," *IEEE Transactions on instrumentation and measurement*, vol. 37, no. 3, p. 789–893, 1989.

[108] C. Caloz and A. Sihvola, "Electromagnetic chirality, part 2: the macroscopic perspective [electromagnetic perspectives]," *IEEE Antennas and Propagation Magazine*, vol. 62, no. 2, pp. 82–98, 2020.

[109] K. M. Zeyde, I. B. Milochkin, and A. V. Evgrafov, "Electromagnetic scattering by a complex dielectric cylinder in a rectangular waveguide. Case study in Altair FEKO," in *Ural-Siberian Conference on Biomedical Engineering, Radioelectronics and Information Technology (USBEREIT)*, Ekaterinburg, Russia, 2022, p. 141–144.

[110] W. Lihh, "A second-order asymptotic approximation for the Sommerfeld half-space problem," *IEEE Transactions on antennas and propagation*, vol. 60, no. 1, p. 274–281, 2012.

Simulations and experiments of electromagnetic problems involving materials in motion

Kirill Zeyde